

Mass distribution for single-lined hot subdwarf stars in LAMOST

ZHENXIN LEI,^{1,2} RUIJIE HE,^{1,2} PÉTER NÉMETH,^{3,4} XUAN ZOU,^{1,2} HUAPING XIAO,^{1,2} YONG YANG,⁵ AND JINGKUN ZHAO⁵

¹Key Laboratory of Stars and Interstellar Medium, Xiangtan University, Xiangtan 411105, People's Republic of China

²Physics Department, Xiangtan University, Xiangtan, 411105, People's Republic of China

³Astronomical Institute of the Czech Academy of Sciences, CZ-251 65, Ondřejov, Czech Republic

⁴Astroserver.org, Fő tér 1, 8533 Malomsok, Hungary

⁵Key Laboratory of Optical Astronomy, National Astronomical Observatories, Chinese Academy of Sciences, Beijing 100012, China

ABSTRACT

Masses for 664 single-lined hot subdwarf stars identified in LAMOST were calculated by comparing synthetic fluxes from spectral energy distribution (SED) with observed fluxes from virtual observatory service. Three groups of hot subdwarf stars were selected from the whole sample according to their parallax precision to study the mass distributions. We found, that He-poor sdB/sdOB stars present a wide mass distribution from 0.1 to 1.0 M_{\odot} with a sharp mass peak around at 0.46 M_{\odot} , which is consistent with canonical binary model prediction. He-rich sdB/sdOB/sdO stars present a much flatter mass distribution than He-poor sdB/sdOB stars and with a mass peak around 0.42 M_{\odot} . By comparing the observed mass distributions to the predictions of different formation scenarios, we concluded that the binary merger channel, including two helium white dwarfs (He-WDs) and He-WD + main sequence (MS) merger, cannot be the only main formation channel for He-rich hot subdwarfs, and other formation channels such as the surviving companions from type Ia supernovae (SNe Ia) could also make impacts on producing this special population, especially for He-rich hot subdwarfs with masses less than 0.44 M_{\odot} . He-poor sdO stars also present a flatter mass distribution with an inconspicuous peak mass at 0.18 M_{\odot} . The similar mass - ΔRV_{\max} distribution between He-poor sdB/sdOB and sdO stars supports the scenario that He-poor sdO stars could be the subsequent evolution stage of He-poor sdB/sdOB stars.

1. INTRODUCTION

Hot subdwarf stars are located at the region between the main sequence (MS) and the white dwarf (WD) cooling sequence in the Hertzsprung-Russell (HR) diagram (Heber 2009, 2016). These blue stars have small stellar masses around 0.5 M_{\odot} , high effective temperatures (e.g., roughly $20000 \text{ K} \leq T_{\text{eff}} \leq 70000 \text{ K}$) and gravity (e.g., roughly $5.0 \leq \log g \leq 6.5$), and they can be roughly classified into B and O type (sdB/O) based on their spectral line features. Many hot subdwarf stars are burning Helium (He) in their cores and occupy the bluest positions of horizontal branch (HB), thus known as extreme HB (EHB) stars. Other types of stars could also cross the hot subdwarf region in the HR diagram, such as post-EHB stars, blue hook stars in globular clusters (Brown et al. 2010, 2016), post asymptotic giant branch (post-AGB) stars, post red giant branch (post-RGB) stars, low and extremely low mass (pre-)white dwarfs (pre-ELM WDs), etc (Heber 2016).

The bulk of the currently known hot subdwarf stars were discovered only recently in the data releases of large surveys, such as the Sloan Digital Sky Survey (Geier et al. 2015; Kepler et al. 2015, 2016, 2019), ESO Supernova Ia Progenitor Survey (SPY, Lisker et al. 2005; Stroerer et al. 2007), The Hamburg Quasar Survey (HQS, Edelmann et al. 2003), The Arizona-Montréal Spectroscopic Program (Fontaine et al. 2014), The Large Sky Area Multi-Object Fiber Spectroscopic Telescope spectra survey (LAMOST, Luo et al. 2016, 2019, 2021; Lei et al. 2018, 2019b, 2020, 2023), Galaxy Evolution Explorer survey (GALEX, Vennes et al. 2011; Németh et al. 2012) and Transiting Exoplanet Survey Satellite (TESS, Krzesinski et al. 2022). Reliable atmospheric parameters (e.g., T_{eff} , $\log g$ and $\log(n\text{He}/n\text{H})$)

were obtained by spectral analysis in these studies, and it provides great convenience on studying these special blue stars in our Galaxy.

A catalog of known hot subdwarf stars was compiled from literature and reported by Geier et al. (2017), which contains 5613 objects and a lot of useful information, including multi-band photometry, ground-based proper motions, classifications, published atmospheric parameters. Thanks to the continuously running large surveys mentioned above, the number of confirmed hot subdwarfs was updated successively to 5874 and 6616 by Geier (2020) and Culpan et al. (2022), respectively.

Hot subdwarf stars can be further classified into more sub-types according to the different strength of hydrogen (H) and He lines in their spectra, e.g., He-poor sdB/sdOB/sdO stars and their He-rich counterparts, He-rich sdB/sdOB/sdO stars (Moehler et al. 1990; Geier et al. 2017; Lei et al. 2018). Drilling et al. (2013) designed an MK (Morgan–Keenan)-like spectral classification scheme for hot subdwarf stars, in which a spectral class, a luminosity class, and a helium class are needed for spectral classification. With this detailed classification scheme, Lei et al. (2019a) classified 56 hot subdwarf stars found in LAMOST DR1, and Jeffery et al. (2021) classified 107 hot subdwarf stars observed by the Southern African Large Telescope (SALT).

Since most of the sdB type hot subdwarfs were found in close binary systems (Maxted et al. 2001; Napiwotzki et al. 2004; Copperwheat et al. 2011), binary evolution is considered to be the main formation channel for these stars (see Mengel et al. 1976 for early discussions on this topic). Based on the results from detailed binary population synthesis, Han et al. (2002, 2003) found that stable Roche lobe overflow (RLOF), common envelope (CE) ejection and the merger of two He-WDs due to binary evolution can produce sdB stars, and most of the properties of these stars, such as the period and mass distribution, positions in the $T_{\text{eff}} - \log g$ plane, etc (also see Chen et al. 2013) are consistent with observations. These models predicted that the mass range of sdB stars extends from 0.3 to 0.8 M_{\odot} .

The two He-WD merger channel is considered to be the main formation channel for single He-rich hot subdwarf stars (Webbink 1984). Zhang & Jeffery (2012) studied the merger of two He-WDs and found that a composite model of slow accretion from a debris disk and fast accretion into a corona can reproduce the observed properties of T_{eff} , $\log g$, nitrogen (N) and carbon (C) abundances for He-rich hot subdwarf stars. Moreover, Zhang et al. (2017) also studied the post-merger models of a He-WD with a MS star. They found that the merger of He-WD+MS channel could produce intermediate He-rich hot subdwarfs (iHe-rich, e.g., $-1.0 < \log(n\text{He}/n\text{H}) < 1.0$), and a mass range of 0.48 - 0.52 M_{\odot} was predicted for these stars in their model. Recently, companions surviving from Type Ia supernovae (SNe Ia) explosions were also predicted to evolve into single hot subdwarfs. Meng & Luo (2021) studied the surviving companions from SNe Ia explosions of WD + MS binaries and found that this channel could produce single iHe-rich hot subdwarfs. Based on the results of detailed binary population synthesis, they obtained a Galactic birth rate of $2.3 - 6 \times 10^{-4} \text{ yr}^{-1}$ for their spin-up/down model.

On the other hand, Miller Bertolami et al. (2008) proposed that He-rich hot subdwarf stars could be formed through single stellar evolution. In their study, after losing nearly the whole envelope at the tip of RGB, stars could experience a delayed core He flash while on the way to the WD cooling curve or already on it (also see Castellani & Castellani 1993 for late He flash scenarios on WD cooling curves). This delayed core He flash could drive a deep mixing in the envelope thus leading to He and C enhancement at the stellar surface. However, based on the observed distribution of rotation rates for the companions in known wide hot subdwarf binaries, Pelisoli et al. (2020) found that binary interaction is always required for the formation of hot subdwarfs. This result seems to contradict the single formation channel of He-rich hot subdwarfs. Furthermore, Geier et al. (2022) studied the radial velocities (RVs) for 646 single-lined hot subdwarfs with multi-epoch observed spectra in SDSS and LAMOST. No significant RV variations were detected for nearly all He-rich hot subdwarfs, but the exact opposite is true for He-poor ones. Their results support the merger formation channel for He-rich hot subdwarfs.

Mass is a very important parameter to test and constrain formation channels for hot subdwarf stars. Unfortunately, based on the observational data available until now, obtaining exact masses for a large number of hot subdwarfs is difficult. To study the empirical mass distribution for sdB stars, Fontaine et al. (2012) collected 16 sdB stars with known masses on the basis of asteroseismology and 11 sdB stars in binary systems with masses determined by light curve modeling and spectroscopy. They found a relatively sharp mass distribution with a mean mass around 0.47 M_{\odot} , but with a wide mass range of 0.28-0.63 M_{\odot} . Their results were consistent with model predictions from Han et al. (2002, 2003) when selection effects were considered. Furthermore, combining with the distance from *Gaia* parallax (Gaia Collaboration et al. 2021) and atmospheric parameters, Schaffenroth et al. (2022) obtained angular diameters thus radius and masses for 68 sdB stars in binary systems by comparing observed fluxes with synthetic fluxes calculated

from spectral energy distributions (SED). They found that the mass distribution of sdB stars with cool, low-mass stellar, and sub-stellar companions differ from those with WD companions, which demonstrated that they most likely come from different populations.

Although more than 6000 hot subdwarf stars have become known (Culpan et al. 2022) until now, among which more than 3000 stars have reliable atmospheric parameters (e.g., T_{eff} , $\log g$ and $\log(n\text{He}/n\text{H})$) from spectral fitting, there is still a lack of masses for a large number of hot subdwarf stars to study the mass distribution statistically, thus to investigate the formation and evolution of these stars. In this study, we build on the atmospheric parameters obtained in our previous studies (Lei et al. 2018, 2019b, 2020). From those models, we calculated synthetic SEDs for 664 single-lined hot subdwarfs identified in LAMOST and obtained their radii, masses, and luminosity by comparing the synthetic fluxes with observed fluxes from the virtual observatory (VO) service (Bayo et al. 2008). Based on these results, we studied the possible formation channels for hot subdwarf stars with different spectral classifications. Section 2 described the method used to obtain masses for hot subdwarf stars. Our results are given in Section 3, and a discussion is presented in Section 4. Finally, a summary of our study is given in Section 5.

2. METHODOLOGY

2.1. Basic principle

Once the synthetic spectral energy distribution (SED) of a star is known, we can obtain the model flux density at the stellar surface, $F(\lambda)$. On the other hand, the observed flux density at the Earth, $f(\lambda)$, can be obtained by converting photometric magnitudes into flux density (see Heber et al. 2018, Baran et al. 2021 and Schaffenroth et al. 2022 for more information). With known $F(\lambda)$, $f(\lambda)$ and distance from the Earth, d , one can easily obtain the stellar angular diameter, Θ , and stellar radius, R , by the following equation:

$$\frac{f(\lambda)}{F(\lambda)} = \frac{\Theta^2}{4} = \frac{R^2}{d^2} \quad (1)$$

Then, the stellar mass of a hot subdwarf star can be obtained by:

$$M = \frac{gR^2}{G} \quad (2)$$

where g is the surface gravity and G is the gravitational constant.

2.2. Sample selection, distances estimation, magnitudes conversion into photometric fluxes

With the useful information from Gaia DR2 (Gaia Collaboration et al. 2018), e.g., magnitudes, parallaxes, colors, etc, Lei et al. (2018, 2019b, 2020) identified 864 single-lined hot subdwarf stars in LAMOST. Since all of these hot subdwarf stars have good quality LAMOST spectra (e.g., signal-to-noise ratio, SNR, greater than 10.0 in the u band), they obtained reliable atmospheric parameters (e.g., T_{eff} , $\log g$ and $\log(n\text{He}/n\text{H})$) by fitting H and He profiles with synthetic spectra, which were calculated with SYNSPEC (version 49, Lanz & Hubeny 2007) from non-Local Thermodynamic Equilibrium (NLTE) TLUSTY model atmospheres (version 204; Hubeny & Lanz 2017). Based on the obtained atmospheric parameters, synthetic SEDs were also calculated for each star in the same way as the synthetic spectra.

Gaia EDR3 (Gaia Collaboration et al. 2021) provided astrometry and photometry for 1.8 billion objects collected in the first 34 months of the satellite mission, among which 1.5 billion sources have parallaxes, proper motions, and G , G_{BP} , G_{RP} magnitudes. With precise parallaxes, we could calculate distances for a huge number of objects which are bright and relatively nearby to the Sun. However, distances cannot be obtained simply by directly reversing parallaxes for faint and distant objects, since the parallax uncertainties are large, even negative parallaxes can occur. To provide more reliable distances for as many stars in Gaia EDR3 as possible, Bailer-Jones et al. (2021) used a probabilistic approach, which employed a prior constructed from a three-dimensional model of our Galaxy, and estimated stellar distances based on Gaia parallaxes and photometry.

In this study, 864 single-lined hot subdwarf stars identified in Lei et al. (2018, 2019b, 2020) were cross-matched with Gaia EDR3 data (Gaia Collaboration et al. 2021) to obtain their parallaxes. By inspecting quasar data in Gaia EDR3 Lindegren et al. (2021a) found that parallaxes can be biased. Lindegren et al. (2021b) investigated the variation of the parallax bias for Gaia EDR3 data with magnitude, colour, and ecliptic latitude. They provided a python

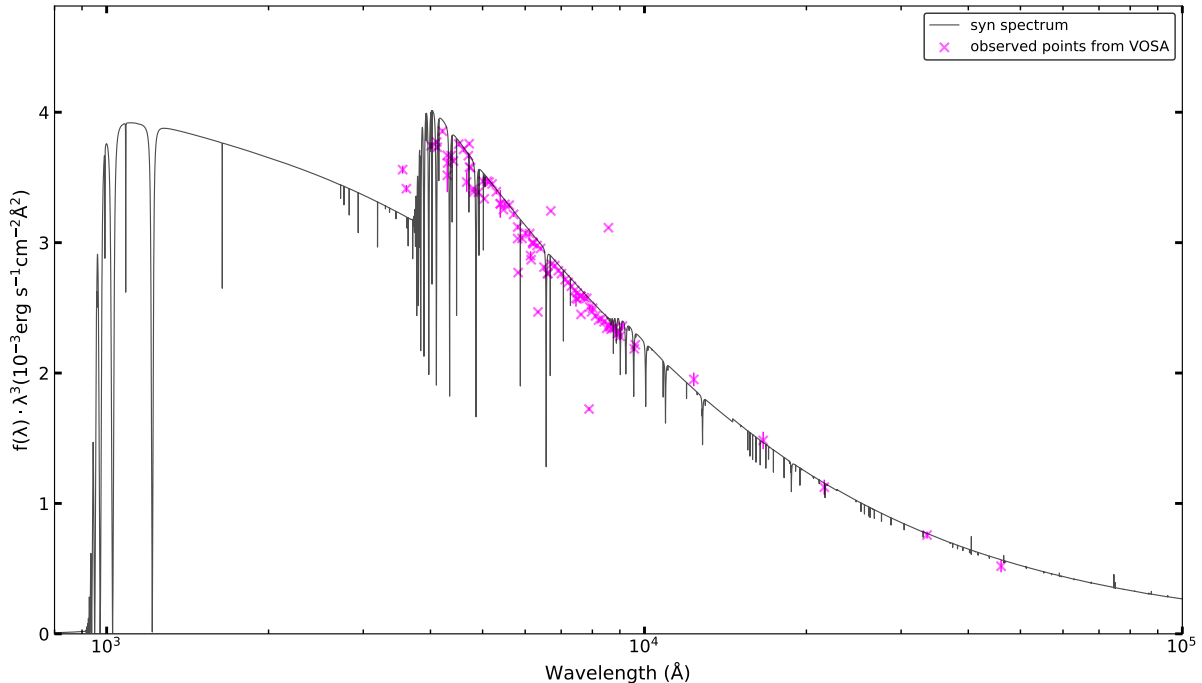


Figure 1. Example of comparison synthetic SED with observed photometric fluxes. Flux density is multiplied by wavelength to the power of three to eliminate the steep slope of SED. Black solid curve denotes the synthetic SED calculated based on the atmospheric parameters obtained from LAMOST spectra fitting, while magenta crosses denote the observed photometric fluxes with different filters retrieved from VOSA.

implementation¹ to correct the bias for *Gaia* EDR3 parallaxes, which was also adopted for our selected sample in this study. Since the uncertainty of parallax can affect the precision of distance directly, thus affecting the determination of stellar radius and mass (Irrgang et al. 2021), only objects with positive parallax and a relative parallax uncertainty of less than 20% (e.g., $\varpi > 0$ and $\sigma_{\varpi}/\varpi \leq 0.2$, see Raddi et al. 2022) were reserved for the following analysis. After this step, 727 hot subdwarf stars with *Gaia* EDR3 parallax remained in our selection, and their distances were obtained directly by using the inverse of parallaxes after applying a zero-point correction.

We used the VO Sed Analyzer² (VOSA, Bayo et al. 2008) of the Spanish Virtual Observatory (SVO) to search for photometric data for our sample and convert observed magnitudes to fluxes. VOSA is a public web tool designed to help users search for observed photometric data from Virtual Observatory (VO) services and build SEDs. It can compare observed photometry with synthetic photometry from theoretical models to obtain important physical parameters for stars, such as T_{eff} , $\log g$, metallicity, radius, luminosity, etc. We obtained interstellar extinctions in the visual band, A_V , for the selected sample through Galactic dust reddening maps³ (Schlegel et al. 1998; Schlafly & Finkbeiner 2011) with extinction parameter $R_V = 3.1$. All this information together with coordinates (e.g., RA, DEC) of the sample was uploaded into VOSA, then the conversion of photometric fluxes from different filters could be obtained for each sample stars.

2.3. Dilution parameter, radius and luminosity

To compare synthetic SEDs with observed photometric fluxes, one needs to convolve synthetic SEDs with the transmission curve of the specific filter. Thanks to the Filter Profile Service⁴ in SVO (Rodrigo et al. 2012; Rodrigo & Solano 2020), which provided information for more than 2300 astronomical filters, including transmission curves and zero points in the Vega, AB, and ST photometric systems, we obtained all the transmission curves and zero point information of the astronomical filters listed in the Filter Profile Service. Then, we convolved the synthetic SEDs

¹ <https://www.cosmos.esa.int/web/gaia/edr3-code>

² <http://svo2.cab.inta-csic.es/svo/theory/vosa/>

³ <https://irsa.ipac.caltech.edu/applications/DUST/>

⁴ <http://svo2.cab.inta-csic.es/theory/fps3/>

with the filter transmission curves and compared them with the observed photometric fluxes obtained from VOSA. By doing this, we obtained the dilution factor $M_d = R^2/d^2$ and stellar angular diameter Θ (see Equation 1) for our selected sample.

Fig 1 gives an example of a comparison between synthetic SED and observed photometric fluxes for one of the selected stars, LAMOST_obsid = 580907209. The observed photometric data were collected from about 100 filters within different passbands equipped on various photometric systems, such as the Galaxy Evolution Explorer (GALEX, Martin et al. 2005), Gaia mission (Gaia Collaboration et al. 2016), Two Micron All Sky Survey (2MASS, Skrutskie et al. 2006), Wide-field Infrared Survey Explorer (WISE, Wright et al. 2010), etc. Fig 1 shows that most of the observed photometric fluxes (e.g., magenta crosses) are consistent with the synthetic SED (e.g., black solid curve).

Once the stellar radii and effective temperatures are known, one can calculate the luminosity of a star by comparing the two parameters with the solar standard model using the following equation:

$$\frac{L}{L_\odot} = \left(\frac{R}{R_\odot}\right)^2 \left(\frac{T_{\text{eff}}}{T_\odot}\right)^4 \quad (3)$$

where R_\odot and T_\odot are radius and surface effective temperature of the Sun, which were set to 6.959×10^8 m and 5777 K respectively.

2.4. Mass calculation and uncertainty estimation

With known radius and $\log g$, we can calculate the stellar masses for the selected sample through Equation 2. To estimate mass uncertainties, a Monte Carlo (MC) approach was adopted in the calculations. Based on the values and uncertainties for the parameters involved in mass determination (i.e., parallaxes, gravity, etc), a set of values was generated for each parameter by using a Gaussian distribution. With these values, the same number of masses was calculated for each sample star. In the calculation, with the symmetric uncertainty, we assumed a Gaussian distribution of parallax for each star. However, the transformation from parallax to distance is nonlinear, thus the distances obtained for each star are not a Gaussian-like distribution and their uncertainties are asymmetric (for a detailed discussion see Bailer-Jones 2015; Astraatmadja & Bailer-Jones 2016; Bailer-Jones et al. 2021). This is also valid for the obtained mass values. Therefore, for each sample star, we calculated the median (e.g., 50th percentile) mass value as the final mass. Moreover, the 16th and 84th percentile mass values form a 68% confidence interval around the median mass, and the differences between them and the median mass are considered as the asymmetric uncertainties of the mass (see Column 14 in Table 1).

Atmospheric parameters for hot subdwarf stars in Lei et al. (2018, 2019b, 2020) were obtained with NLTE model atmospheres and only statistical uncertainties were presented, while no systematic errors were considered in their studies. A realistic assessment of systematics must be based on independent studies, therefore, we estimated systematic errors for T_{eff} and $\log g$ by comparing atmospheric parameters in Lei et al. (2018, 2019b, 2020) with the results from Schaffenroth et al. (2022). Finally, we found systematic differences of about 560 K and 0.013 dex for the two parameters, respectively. Moreover, different atmospheric models could also lead to systematic errors in parameter determination. Heber et al. (2000) determined atmospheric parameters for three pulsating sdB stars by using blanketed NLTE and LTE model atmospheres respectively. They found that there is no obvious difference in T_{eff} determination between NLTE and LTE models, but NLTE $\log g$ is slightly lower than LTE ones by at least 0.05 dex (see Section 4.1 in their study for detailed discussion). In this study, the systematic errors for T_{eff} and $\log g$ discussed above were added to the statistical uncertainties in quadrature for the selected hot subdwarf stars to estimate their mass uncertainties.

Based on the method described above, we obtained masses for 727 hot subdwarf stars from Lei et al. (2018, 2019b, 2020). For some of these hot subdwarf stars, we got excessively large mass values (e.g., larger than $1.0 M_\odot$), which are not likely real hot subdwarfs, or their mass values are unreliable due to large uncertainties of distances and/or gravity. On the other hand, a few stars turned out to have very low mass values (e.g., less than $0.1 M_\odot$). These stars may be extremely low-mass white dwarfs or the mass values are unreliable due to large uncertainties from related parameters as well. Such extreme cases are not reported here. In total, 664 hot subdwarf stars having mass values between 0.1 and $1.0 M_\odot$, are reported and analyzed in the following sections.

3. RESULTS

Table 1 presents the calculated mass values and some useful information for 664 selected hot subdwarf stars. From left to right, columns 1-3 give right ascension (RA), declination (DEC) and LAMOST_obsid, respectively. Columns 4-6

give Gaia EDR3 source_id, G magnitudes, and parallaxes after zero-point correction. Columns 7-10 show T_{eff} , $\log g^5$, and spectral classification from [Lei et al. \(2018, 2019b, 2020\)](#). Column 10 gives E(B-V) values, while columns 11-14 give angular diameters, stellar radius, stellar luminosity, and masses, respectively, which were calculated in this study. For each sample star, we calculated the 16th, 50th (median), and 84th percentile values for the last four parameters, and reported the median values as the final values listed in Table 1, while the differences between the 16th, 84th percentile values and the median value were reported as asymmetric uncertainties (see Section 2.4 for more information).

⁵ The systematic errors discussed in Section 2.4 have been added to the uncertainties of T_{eff} and $\log g$.

Table 1. Main parameters for the 664 hot subdwarfs selected in this study.

RA	DEC	obs_id	source_id	G	parallax	T_{eff}	$\log g$	spclass	E(B-V)	Angular diameter	Radius	Luminosity	Mass
LAMOST (1)	LAMOST (2)	LAMOST (3)	Gaia EDR3 (4)	Gaia EDR3 (mag) (5)	Gaia EDR3 (mas) (6)	(K) (7)	(cm s^{-2}) (8)	(9)	(10)	log(rad) (11)	R/R_{\odot} (12)	L/L_{\odot} (13)	M/M_{\odot} (14)
0.0767	22.30079	385816105	284797322031768832	14.219558±0.002796	1.2039±0.0359	28810±630	5.57±0.06	sdB	0.058±0.004	-11.013±0.004	0.176±0.006	19.2±2.3	0.42±0.08
0.278039	11.01084	66605009	2765454164004531328	13.580941±0.02805	1.6454±0.0352	27030±602	5.48±0.05	sdB	0.071±0.002	-10.856±0.003	0.191±0.004	17.4±1.9	0.40±0.05
0.535283	19.987016	385805170	2846319155418023424	15.581263±0.002853	0.4198±0.0496	31560±722	5.58±0.08	sdB	0.035±0.002	-11.348±0.008	0.233±0.035	48.5±16.3	0.77±0.29
0.981681	27.810404	492112073	2854091981071865344	13.308936±0.002796	1.7692±0.0329	28000±572	5.56±0.06	sdB	0.048±0.002	-10.826±0.010	0.188±0.004	19.4±1.7	0.47±0.06
1.8907183	13.5993244	619614193	2767874292175410560	13.047603±0.002814	2.0899±0.0285	29560±577	5.41±0.05	sdB	0.11±0.005	-10.746±0.029	0.188±0.003	24.0±2.4	0.33±0.05
2.1021972	49.083822	593009050	39359879591384576	15.888843±0.002816	0.6389±0.0432	26640±899	5.53±0.09	sdB	0.108±0.002	-11.297±0.012	0.178±0.013	14.3±3.5	0.40±0.14
2.188996	12.288674	66613068	2766032919436757504	14.60169±0.002839	1.1883±0.0489	32230±654	6.00±0.09	sdB	0.071±0.001	-11.123±0.011	0.139±0.007	18.8±2.8	0.70±0.22
2.923521	19.340418	364410161	2797293512483062912	14.726053±0.002797	0.8772±0.0362	27310±590	5.45±0.06	sdB	0.037±0.001	-11.105±0.006	0.197±0.009	19.2±2.1	0.39±0.07
2.9364712	46.801838	593007055	392942881419391872	14.352201±0.002826	0.7103±0.0396	45110±704	5.34±0.06	He-sdOB	0.091±0.006	-11.186±0.005	0.204±0.013	155.5±22.6	0.34±0.07
3.580483	22.40487	487408198	2800515322070491008	13.420411±0.002814	1.1698±0.0326	36160±987	5.35±0.09	sdB	0.061±0.004	-10.947±0.002	0.210±0.006	67.1±9.8	0.37±0.08
3.593379	28.615494	2915216	2859984160805522176	12.625363±0.002785	2.6611±0.0463	24180±570	5.44±0.06	sdB	0.032±0.001	-10.646±0.004	0.189±0.004	10.9±1.3	0.36±0.05
4.2165006	52.146517	615603055	395157267782903808	16.780361±0.002815	0.4047±0.0552	29170±664	5.46±0.08	sdB	0.167±0.005	-11.465±0.007	0.187±0.022	22.7±5.1	0.31±0.10
4.23055	51.230486	615605186	394991241522199040	16.3279±0.003783	0.4742±0.0465	32770±728	5.48±0.08	sdB	0.132±0.001	-11.449±0.009	0.166±0.016	28.7±8.1	0.36±0.10
4.6252262	48.806384	593013047	392840562417338112	15.281122±0.002802	0.3283±0.0347	24740±582	5.02±0.06	sdB	0.094±0.005	-11.139±0.014	0.491±0.048	80.7±16.3	0.93±0.22
4.681331	1.023214	266708166	2547139876837313920	14.860316±0.00281	0.6462±0.0449	29090±584	5.47±0.07	sdB	0.025±0.0	-11.163±0.042	0.236±0.015	35.7±5.5	0.59±0.16
4.822343	40.502298	475310178	380384779299991424	16.31493±0.00282	0.3941±0.0523	26620±853	5.07±0.08	sdB	0.076±0.002	-11.387±0.023	0.231±0.026	24.0±2.5	0.23±0.05
5.8632988	40.482537	90110033	380338531092183424	15.495041±0.002799	0.4903±0.0403	26580±767	5.34±0.07	sdB	0.056±0.001	-11.236±0.005	0.256±0.005	29.4±1.9	0.52±0.15
5.8632988	41.130463	615605166	394843322846749824	15.930698±0.002822	0.5821±0.042	26610±590	5.42±0.06	sdB	0.142±0.005	-11.272±0.006	0.208±0.017	16.5±3.8	0.42±0.09
5.98014	42.151544	90103101	382086995098288896	15.771845±0.0028	0.3996±0.0475	30320±606	5.55±0.08	sdB	0.056±0.001	-11.351±0.004	0.247±0.034	49.9±2.9	0.79±0.29
6.0352547	56.027472	605908160	421328839978415616	16.15531±0.002826	0.737±0.0406	35020±795	5.76±0.14	sdOB	0.348±0.024	-11.321±0.013	0.144±0.009	27.8±4.6	0.43±0.17
6.36564	8.965084	248813198	2750667003920099200	15.584294±0.002824	0.5913±0.0543	29700±592	5.39±0.07	sdB	0.056±0.002	-11.302±0.008	0.187±0.017	24.7±5.0	0.31±0.10
6.439609	31.591527	284601234	2862287843823854848	15.506684±0.002832	0.5117±0.0447	26180±659	5.39±0.06	sdB	0.065±0.002	-11.228±0.007	0.261±0.025	29.2±5.7	0.61±0.17
6.51063	31.1057	679407014	2862194144817359872	14.84873±0.00281	0.8539±0.037	30150±575	5.52±0.10	sdB	0.078±0.001	-11.147±0.006	0.188±0.007	26.2±3.9	0.42±0.14
6.528333	44.555064	382607056	382781542850500352	17.22106±0.002856	0.3836±0.068	35770±654	5.76±0.09	sdOB	0.061±0.002	-11.713±0.009	0.112±0.018	18.2±1.5	0.26±0.09
6.949183	34.674052	75901223	365939429892433920	15.756424±0.002827	0.8143±0.0675	33010±734	5.72±0.07	He-sdOB	0.077±0.001	-11.373±0.006	0.117±0.013	14.6±3.3	0.27±0.08
7.287603	4.939857	182909073	2554910434747250944	14.960979±0.002891	0.7354±0.0537	33870±722	5.68±0.09	sdB	0.112±0.0	-11.265±0.010	0.162±0.012	31.2±4.9	0.47±0.13
7.329288	52.97546	615609066	416403783797286784	16.766638±0.002838	0.3227±0.0616	36080±747	5.66±0.58	sdB	0.174±0.004	-11.554±0.014	0.191±0.030	54.0±36.2	0.65±1.98
8.943925	26.915094	157510209	280942136625514112	14.257147±0.002821	1.1591±0.0398	27150±767	5.58±0.08	sdB	0.041±0.001	-11.008±0.004	0.191±0.007	17.7±2.2	0.51±0.12
9.507177	34.53228	14610118	365002268028633600	13.880549±0.002804	1.1197±0.0304	40620±630	5.55±0.09	He-sdOB	0.096±0.002	-11.063±0.009	0.170±0.006	71.1±5.4	0.37±0.11
9.522662	43.74734	472206190	387661209812972928	16.11442±0.002876	0.6732±0.0585	36180±853	5.85±0.11	sdOB	0.061±0.002	-11.494±0.009	0.104±0.011	16.9±4.5	0.28±0.11
11.70128	19.39863	285308094	2801277176253968640	14.962909±0.002827	0.9281±0.0413	32230±617	5.89±0.08	sdB	0.046±0.002	-11.218±0.015	0.142±0.006	19.4±1.9	0.57±0.13
11.918803	31.398766	186304225	360511037906831872	14.802395±0.002798	1.0593±0.0383	30990±630	5.75±0.06	sdB	0.056±0.001	-11.160±0.011	0.145±0.006	17.4±2.4	0.44±0.08
12.321444	20.944565	164803013	28014448085887897216	14.543051±0.002841	0.9486±0.0371	27890±809	5.34±0.08	sdB	0.026±0.001	-11.083±0.006	0.149±0.008	20.3±3.4	0.49±0.10
12.452466	35.366938	14604029	363795760175504768	14.810419±0.002851	0.8767±0.0412	35150±716	5.78±0.08	sdOB	0.048±0.005	-11.236±0.005	0.149±0.008	30.2±3.4	0.49±0.10
12.949002	27.003799	157506158	2808769596378258048	15.793072±0.002854	0.8894±0.0622	31780±654	5.82±0.15	sdB	0.04±0.001	-11.389±0.008	0.101±0.006	9.5±1.8	0.24±0.13
13.640353	37.970977	82010071	364742852004132736	14.605407±0.002848	1.034±0.0418	33680±774	6.08±0.11	sdOB	0.042±0.001	-11.175±0.004	0.144±0.005	24.1±2.8	0.94±0.19
14.602768	1.909744	8206211	2537690089791382656	15.108394±0.002833	0.7864±0.0502	33290±824	5.53±0.10	sdOB	0.02±0.001	-11.283±0.005	0.149±0.010	24.4±3.6	0.28±0.08
15.305503	31.432091	96302063	312628749626419328	13.063463±0.002835	1.807±0.0362	27150±617	5.48±0.05	sdB	0.055±0.002	-10.761±0.003	0.214±0.004	22.4±2.0	0.51±0.07

Table 1 continued on next page

Table 1 (continued)

RA	DEC	obs.id	G	parallax	T_{eff}	$\log g$	spclass	E(B-V)	Angular diameter	Radius	Luminosity	Mass
LAMOST (1)	LAMOST (2)	LAMOST (3)	Gaia EDR3 (4)	Gaia EDR3 (mas) (5)	(K) (7)	(cm s^{-2}) (8)	(9)	(10)	log(rad) (11)	R/R_{\odot} (12)	L/L_{\odot} (13)	M/M_{\odot} (14)
36.005261	21.947266	379608221	99836961472298752	15.672043±0.002906	37010±675	5.86±0.08	sdOB	0.113±0.003	-11.379±0.011	0.115±0.008	22.3±5.5	0.35±0.09
36.301804	23.806172	379609016	101826669497182720	13.817124±0.002865	52640±1491	5.46±0.10	sdO	0.108±0.006	-11.107±0.013	0.123±0.004	104.6±16.3	0.16±0.04
37.757164	27.718067	627301227	127674641678296704	1.3925±0.0406	43620±1509	5.71±0.05	sdO	0.106±0.002	-11.338±0.008	0.099±0.004	45.5±7.3	0.40±0.03
38.001041	33.876702	632206097	134510477267997952	1.8625±0.0415	27350±626	5.62±0.06	sdB	0.074±0.001	-11.165±0.077	0.178±0.004	9.1±1.8	0.48±0.10
38.216289	44.190929	180412223	341195058150383104	1.2611±0.0577	34400±802	5.74±0.08	sdOB	0.071±0.002	-11.093±0.003	0.142±0.010	25.2±3.7	0.41±0.10
38.225357	37.072618	176806221	333636534183932416	0.9231±0.0567	35590±1088	5.66±0.13	He-sdOB	0.049±0.001	-11.436±0.008	0.086±0.004	10.6±1.6	0.12±0.03
38.317737	3.830032	364610005	20063858119453824	15.361883±0.003112	29830±575	5.43±0.06	sdB	0.141±0.011	-11.200±0.017	0.166±0.010	19.6±2.5	0.27±0.05
40.018332	3.928428	160513016	2503706418759709184	13.966229±0.002936	65870±1390	5.19±0.17	He-sdO	0.035±0.002	-11.220±0.005	0.229±0.023	904.8±194.9	0.30±0.19
40.844775	4.843528	293409213	6052403489630720	14.074714±0.002882	34790±575	6.02±0.06	He-sdOB	0.045±0.003	-11.087±0.007	0.123±0.004	19.8±1.2	0.57±0.12
41.412008	13.432122	298408084	31918414533148928	13.185378±0.003002	32120±579	5.89±0.14	sdB	0.09±0.004	-10.836±0.024	0.224±0.004	47.6±4.9	0.40±0.05
41.89582	36.763992	82312150	141428363911552384	12.959655±0.002874	43520±602	5.56±0.06	sdB	0.065±0.003	-10.926±0.006	0.178±0.007	101.3±10.4	0.86±0.45
42.586847	49.209444	714701194	438686001110484352	15.737055±0.002859	31040±587	5.56±0.06	sdB	0.253±0.011	-11.233±0.007	0.157±0.005	20.4±2.7	0.32±0.07
45.303592	18.681715	387107175	35928500943041152	15.400193±0.002891	30240±584	5.43±0.06	sdB	0.142±0.004	-11.206±0.065	0.206±0.024	32.0±5.5	0.43±0.08
45.315923	-2.670405	367406216	5186434732342771968	13.823608±0.002892	26820±610	5.39±0.06	sdB	0.079±0.003	-10.897±0.009	0.224±0.007	23.6±2.7	0.46±0.07
45.548188	37.185967	163303129	142086971376178688	15.487472±0.002894	44530±1791	5.63±0.12	sdO	0.122±0.004	-11.385±0.008	0.122±0.010	53.1±12.9	0.23±0.09
45.650063	28.271376	249704157	116691791828603136	16.252745±0.002896	37070±610	5.87±0.09	sdOB	0.131±0.001	-11.478±0.044	0.102±0.008	17.6±2.7	0.28±0.07
48.4049	15.105965	406503078	31009771252186752	15.607131±0.002964	42110±592	5.63±0.06	He-sdOB	0.158±0.007	-11.372±0.238	0.148±0.011	120.2±9.6	0.41±0.13
48.922807	46.869737	606506145	434851149371030272	15.748208±0.002831	39550±774	5.31±0.07	sdO	0.26±0.009	-11.317±0.006	0.235±0.021	62.6±2.6	0.66±0.18
49.487181	32.497341	76704053	125093503772825856	15.705626±0.002919	34250±610	5.97±0.07	sdOB	0.308±0.006	-11.238±0.007	0.140±0.007	24.2±3.0	0.66±0.18
49.744528	43.927658	616805109	242105008677142976	16.485413±0.002929	28450±590	5.94±0.06	sdB	0.166±0.001	-11.391±0.014	0.106±0.011	6.6±1.6	0.36±0.10
50.388316	8.192122	414808170	11015044926034816	15.912281±0.002899	33610±761	5.69±0.09	sdOB	0.232±0.007	-11.317±0.008	0.142±0.010	23.1±3.2	0.36±0.11
50.411157	5.644444	8315230	9132341717939792	14.9721±0.00296	31550±606	5.84±0.07	sdB	0.181±0.012	-11.129±0.022	0.136±0.006	16.4±2.1	0.45±0.12
51.907159	38.135982	265511138	23486163224343424	14.200628±0.002834	26010±584	5.52±0.05	sdB	0.181±0.011	-10.894±0.005	0.220±0.007	19.7±2.6	0.58±0.09
53.288922	34.208582	292911128	221005208733887488	15.770892±0.002858	35490±704	5.64±0.07	sdOB	0.384±0.011	-11.201±0.013	0.130±0.005	21.6±2.7	0.27±0.06
54.117831	46.137875	587807246	247823740446444416	16.384136±0.002859	35190±602	5.67±0.07	sdOB	0.468±0.004	-11.284±0.008	0.148±0.011	29.9±4.7	0.38±0.08
54.589981	41.734607	296711237	237331822538478592	15.187024±0.002826	27200±582	5.59±0.06	sdB	0.198±0.004	-11.097±0.007	0.172±0.005	14.6±1.4	0.43±0.06
54.696112	41.573393	296715043	237133566847520000	15.088968±0.002838	22240±649	5.76±0.06	sdB	0.204±0.006	-10.999±0.007	0.132±0.003	3.9±0.4	0.37±0.06
54.944312	35.546154	265506073	221375331836119552	15.818334±0.002842	64650±9616	5.61±0.07	sdO	0.375±0.027	-11.340±0.012	0.106±0.005	180.2±150.0	0.17±0.03
55.122076	24.499152	474303164	68334308365794304	16.528624±0.002974	24940±704	5.66±0.09	sdB	0.19±0.007	-11.304±0.052	0.164±0.014	9.3±1.6	0.46±0.10
55.654778	20.022511	249804028	63139734399542528	16.182056±0.002892	44340±963	5.97±0.10	He-sdOB	0.271±0.014	-11.437±0.010	0.143±0.016	71.0±18.8	0.70±0.28
56.022144	22.072953	249811209	64368713521485568	14.384861±0.002963	28130±716	5.59±0.08	sdB	0.217±0.016	-10.936±0.019	0.224±0.007	27.9±4.4	0.70±0.19
57.933712	36.871319	181511115	220091342774317056	16.164291±0.002948	28170±649	5.37±0.09	sdB	0.373±0.016	-11.181±0.037	0.133±0.007	10.0±1.5	0.15±0.05
57.996529	9.640213	587107104	3302502234815943296	15.569411±0.002865	23510±590	5.41±0.05	sdB	0.157±0.002	-11.144±0.004	0.200±0.011	10.9±1.4	0.37±0.07
58.380531	10.751119	159408059	3303143628052101120	12.804302±0.002831	42400±610	5.70±0.07	He-sdOB	0.164±0.007	-10.828±0.006	0.144±0.004	60.0±3.8	0.38±0.07
58.809479	10.470014	159306197	3302955130527310464	14.135757±0.002843	26340±584	5.33±0.05	sdB	0.17±0.005	-10.887±0.008	0.212±0.004	19.4±2.1	0.36±0.05
59.276419	36.74847	397401216	220172981513287936	15.476357±0.00388	84550±3683	5.58±0.06	sdO	0.376±0.019	-11.382±0.016	0.111±0.005	573.2±69.4	0.17±0.03
59.862336	27.08573	1405078	163565999746075264	15.077448±0.002803	32240±1012	5.22±0.15	sdB	0.213±0.008	-11.142±0.046	0.341±0.026	125.3±23.0	0.71±0.22
60.052436	36.596069	397401025	14.874661±0.003071	1.4678±0.0401	22480±577	5.36±0.07	sdB	0.507±0.02	-10.784±0.024	0.247±0.024	14.1±1.6	0.51±0.08
60.197058	17.311691	280513233	4660801680943872	15.430288±0.002792	28750±695	5.57±0.05	sdB	0.386±0.014	-11.053±0.006	0.242±0.013	35.9±4.3	0.79±1.2
60.675411	31.397095	182113038	169258102725227008	15.81645±0.002934	36410±659	6.00±0.12	sdOB	0.239±0.01	-11.315±0.022	0.112±0.006	19.8±2.6	0.45±0.11
61.093981	37.408948	397507109	225573267233289600	16.17439±0.002835	34470±635	5.72±0.11	sdOB	0.297±0.014	-11.328±0.030	0.108±0.005	14.8±1.9	0.23±0.05

Table 1 continued on next page

Table 1 (continued)

RA	DEC	obs.id	source.id	G	parallax	T_{eff}	$\log g$	spclass	E(B-V)	Angular diameter	Radius	Luminosity	Mass
LAMOST (1)	LAMOST (2)	LAMOST (3)	Gaia EDR3 (4)	Gaia EDR3 (5)	Gaia EDR3 (mas) (6)	(K) (7)	(cm s^{-2}) (8)	(9)	(10)	log(rad) (11)	R/R_{\odot} (12)	L/L_{\odot} (13)	M/M_{\odot} (14)
61.095407	26.131827	170611197	162522700650966400	15.696881 ± 0.002869	0.6305 ± 0.044	30350 ± 592	5.75 ± 0.08	sdB	0.162 ± 0.01	-11.274 ± 0.010	0.185 ± 0.015	26.2 ± 5.1	0.69 ± 0.20
62.768174	34.310777	200512196	170774775937432832	16.353783 ± 0.002821	0.7027 ± 0.0583	26840 ± 741	5.43 ± 0.07	sdB	0.31 ± 0.014	-11.246 ± 0.007	0.179 ± 0.020	15.0 ± 3.5	0.31 ± 0.10
62.954352	15.383123	254112160	131822554365339776	14.650105 ± 0.002811	1.309 ± 0.0319	37490 ± 767	5.59 ± 0.07	sdO	0.27 ± 0.006	-11.011 ± 0.004	0.165 ± 0.004	47.8 ± 4.2	0.39 ± 0.07
63.957018	30.587572	504615117	165787700429000064	16.435925 ± 0.002939	0.4194 ± 0.0548	22230 ± 649	5.12 ± 0.06	sdB	0.38 ± 0.003	-11.221 ± 0.010	0.314 ± 0.051	21.8 ± 8.0	0.48 ± 0.20
63.958993	1.905817	174708071	3259060049366022400	14.027809 ± 0.002840	1.5334 ± 0.0402	32920 ± 572	5.78 ± 0.06	sdOB	0.11 ± 0.004	-11.005 ± 0.003	0.142 ± 0.004	21.2 ± 2.3	0.44 ± 0.13
64.404255	30.137843	504604071	165712109004835712	17.042028 ± 0.002876	0.5413 ± 0.0774	31570 ± 596	5.60 ± 0.07	sdB	0.39 ± 0.036	-11.414 ± 0.008	0.089 ± 0.011	6.8 ± 1.4	0.11 ± 0.03
64.820704	36.473358	162001168	177389712764641920	14.600672 ± 0.002863	1.1907 ± 0.0271	42340 ± 617	5.47 ± 0.07	He-sdOB	0.49 ± 0.017	-10.986 ± 0.013	0.193 ± 0.004	107.3 ± 9.4	0.40 ± 0.09
65.998459	34.463668	204704027	176209799348981376	15.165816 ± 0.002943	1.3072 ± 0.0377	35580 ± 606	5.79 ± 0.06	sdOB	0.264 ± 0.005	-11.159 ± 0.024	0.117 ± 0.003	19.7 ± 1.9	0.31 ± 0.06
66.040252	8.554802	425604162	3299455110137611776	12.513357 ± 0.002802	1.8992 ± 0.0324	27210 ± 596	5.27 ± 0.05	sdB	0.234 ± 0.004	-10.539 ± 0.008	0.332 ± 0.006	54.1 ± 5.1	0.75 ± 0.15
67.389212	7.697824	527312249	328714463435536768	15.051167 ± 0.002858	1.0245 ± 0.0421	44080 ± 1157	5.62 ± 0.07	sdO	0.195 ± 0.003	-11.256 ± 0.055	0.122 ± 0.005	50.4 ± 7.1	0.22 ± 0.04
67.80107	42.986157	420301136	253239740960393984	14.539616 ± 0.002841	2.4235 ± 0.0792	26690 ± 592	5.63 ± 0.05	sdB	0.616 ± 0.025	-10.742 ± 0.089	0.165 ± 0.007	12.5 ± 1.6	0.43 ± 0.07
70.810624	23.217639	184707246	146588028382865280	15.886053 ± 0.002865	0.5674 ± 0.0424	36390 ± 1028	5.40 ± 0.29	sdO	0.366 ± 0.005	-11.259 ± 0.019	0.215 ± 0.018	74.0 ± 15.0	0.44 ± 0.38
71.237089	14.363909	282807077	3308791681845675136	14.948787 ± 0.003674	1.4853 ± 0.0289	32660 ± 649	5.66 ± 0.08	sdB	0.497 ± 0.033	-10.950 ± 0.011	0.168 ± 0.003	28.9 ± 2.5	0.47 ± 0.10
72.196713	-4.00472	392308023	3200857538788110080	13.345979 ± 0.002842	2.0072 ± 0.0412	29370 ± 567	5.65 ± 0.05	sdB	0.031 ± 0.002	-10.866 ± 0.003	0.151 ± 0.003	14.1 ± 1.2	0.37 ± 0.06
72.615315	15.986111	402814084	3405118997904684032	16.614313 ± 0.002869	0.5651 ± 0.0628	37480 ± 626	5.73 ± 0.09	He-sdOB	0.404 ± 0.016	-11.400 ± 0.009	0.159 ± 0.023	44.5 ± 14.6	0.49 ± 0.19
73.16829	17.529048	285501028	3406444218653682560	16.184155 ± 0.002838	0.5731 ± 0.0564	23550 ± 626	5.16 ± 0.06	sdB	0.43 ± 0.012	-11.102 ± 0.005	0.307 ± 0.027	25.8 ± 4.9	0.50 ± 0.14
75.717784	16.44665	266202113	3393408962846662656	15.588611 ± 0.002847	0.5869 ± 0.0426	44970 ± 1838	5.16 ± 0.20	sdO	0.327 ± 0.007	-11.277 ± 0.045	0.206 ± 0.016	155.5 ± 30.5	0.22 ± 0.17
76.68493	11.604413	407202008	33881118939200000	15.397572 ± 0.002873	0.6154 ± 0.04	32480 ± 602	5.34 ± 0.13	sdOB	0.191 ± 0.003	-11.223 ± 0.008	0.214 ± 0.015	45.8 ± 1.1	0.37 ± 0.17
76.710748	19.515218	202201036	3407876749162251648	16.049084 ± 0.002957	0.6822 ± 0.0513	50610 ± 1183	5.82 ± 0.10	He-sdO	0.437 ± 0.011	-11.332 ± 0.011	0.151 ± 0.013	132.6 ± 29.4	0.53 ± 0.19
77.306642	33.503376	209916235	181774221540061824	15.423825 ± 0.002804	0.8226 ± 0.0394	25640 ± 599	5.32 ± 0.05	sdB	0.555 ± 0.016	-10.914 ± 0.037	0.324 ± 0.017	40.6 ± 5.0	0.81 ± 0.15
77.51154	12.879591	407205159	3388371103647349632	16.047798 ± 0.002871	1.1843 ± 0.0523	32300 ± 587	6.06 ± 0.07	sdB	0.447 ± 0.007	-11.198 ± 0.036	0.119 ± 0.005	13.9 ± 1.6	0.59 ± 0.14
78.457499	17.700698	317806011	3395250473024213120	14.037423 ± 0.002816	1.7333 ± 0.0277	30990 ± 599	5.50 ± 0.07	sdB	0.29 ± 0.004	-10.871 ± 0.016	0.173 ± 0.003	24.8 ± 2.5	0.34 ± 0.07
80.86406	14.078763	374402025	3390235531771243904	15.841971 ± 0.002821	0.6548 ± 0.04	21770 ± 577	5.01 ± 0.07	sdB	0.384 ± 0.004	-11.081 ± 0.008	0.310 ± 0.016	19.5 ± 3.0	0.36 ± 0.07
81.286539	17.953808	374416146	3400347392320018176	15.649051 ± 0.002846	0.9905 ± 0.0478	34810 ± 781	5.68 ± 0.10	sdOB	0.385 ± 0.011	-11.181 ± 0.014	0.147 ± 0.008	28.1 ± 4.8	0.38 ± 0.12
81.961523	16.909214	374415024	3397199529183763072	15.639553 ± 0.002887	0.7154 ± 0.0439	45490 ± 923	5.40 ± 0.10	He-sdOB	0.369 ± 0.008	-11.272 ± 0.007	0.162 ± 0.011	100.5 ± 18.5	0.25 ± 0.06
82.391388	4.122033	506809203	323648827993523584	16.502243 ± 0.002889	0.5531 ± 0.0679	33980 ± 2193	6.00 ± 0.13	He-sdOB	0.119 ± 0.001	-11.486 ± 0.011	0.111 ± 0.016	15.3 ± 4.8	0.45 ± 0.14
83.163266	43.638849	499503037	195587076882426880	16.330063 ± 0.002883	0.6082 ± 0.0519	30010 ± 606	5.58 ± 0.11	sdB	0.443 ± 0.008	-11.232 ± 0.071	0.215 ± 0.023	33.5 ± 8.7	0.64 ± 0.23
83.279828	7.506107	208913243	3334223901191558784	13.787975 ± 0.00281	1.9994 ± 0.0289	35370 ± 1192	5.89 ± 0.08	sdOB	0.29 ± 0.02	-10.877 ± 0.028	0.147 ± 0.002	30.4 ± 4.9	0.61 ± 0.13
83.338169	16.113207	258002165	3396876131029433472	15.207465 ± 0.002809	1.508 ± 0.0392	33930 ± 635	5.92 ± 0.08	sdB	0.482 ± 0.022	-11.036 ± 0.025	0.136 ± 0.004	22.1 ± 3.3	0.57 ± 0.12
83.348132	21.438994	198702152	3403657609512772096	16.876516 ± 0.002928	0.6592 ± 0.0778	48580 ± 1290	5.51 ± 0.08	sdO	0.439 ± 0.011	-11.490 ± 0.007	0.110 ± 0.016	59.7 ± 12.1	0.14 ± 0.06
83.465224	19.241956	279007127	3400946935393688576	15.730089 ± 0.002865	0.638 ± 0.0467	27170 ± 617	5.36 ± 0.06	sdB	0.332 ± 0.011	-11.126 ± 0.048	0.266 ± 0.021	32.0 ± 5.0	0.55 ± 0.15
84.235335	39.92188	42704127	190970433715259904	13.898839 ± 0.002976	1.3436 ± 0.0332	37890 ± 654	5.57 ± 0.08	He-sdOB	0.559 ± 0.026	-10.804 ± 0.101	0.257 ± 0.007	122.0 ± 11.8	0.90 ± 0.19
85.570863	12.830711	506600580	334052779312131584	16.800829 ± 0.002899	0.6166 ± 0.0735	31100 ± 686	5.59 ± 0.07	sdB	0.37 ± 0.007	-11.374 ± 0.011	0.151 ± 0.017	18.8 ± 4.1	0.33 ± 0.09
85.740707	39.197564	381423200	190164354254168192	14.91727 ± 0.00284	1.2017 ± 0.032	26580 ± 692	5.68 ± 0.08	sdOB	0.559 ± 0.015	-10.981 ± 0.067	0.193 ± 0.006	6.9 ± 1.6	0.65 ± 0.16
86.099395	38.297225	284214035	189831438452843008	16.033384 ± 0.002839	0.582 ± 0.0446	36200 ± 680	5.16 ± 0.07	sdOB	0.522 ± 0.014	-11.108 ± 0.044	0.296 ± 0.026	50.2 ± 10.1	0.47 ± 0.13
86.235913	35.826651	319909136	345626713794023680	15.22899 ± 0.002835	0.8626 ± 0.0344	45570 ± 592	5.60 ± 0.07	He-sdOB	0.626 ± 0.016	-11.063 ± 0.034	0.222 ± 0.009	190.4 ± 16.8	0.72 ± 0.11
86.775955	40.139606	321102181	191727718051389312	15.745667 ± 0.002873	1.053 ± 0.0453	32880 ± 639	5.88 ± 0.07	sdOB	0.375 ± 0.014	-11.190 ± 0.029	0.135 ± 0.006	19.3 ± 2.2	0.50 ± 0.12
86.798328	17.15543	420414102	3396486324095591040	16.374607 ± 0.002887	0.795 ± 0.0615	36050 ± 1772	5.53 ± 0.09	He-sdB	0.328 ± 0.007	-11.341 ± 0.059	0.125 ± 0.012	23.6 ± 5.1	0.20 ± 0.07

Table 1 continued on next page

Table 1 (continued)

RA	DEC	obs.id	source.id	G	parallax	T_{eff}	$\log g$	spclass	E(B-V)	Angular diameter	Radius	Luminosity	Mass
LAMOST (1)	LAMOST (2)	LAMOST (3)	Gaia EDR3 (4)	Gaia EDR3 (mag) (5)	Gaia EDR3 (mas) (6)	(K) (7)	(cm s^{-2}) (8)	(9)	(10)	log(rad) (11)	R/R_{\odot} (12)	L/L_{\odot} (13)	M/M_{\odot} (14)
87.875844	38.478464	381403073	3457951566709510912	16.098612±0.00288	0.7548±0.0527	33180±774	5.80±0.09	sdB	0.475±0.007	-11.209±0.039	0.182±0.014	36.0 ^{+7.8} _{-5.4}	0.75 ^{+0.28} _{-0.16}
87.980862	13.398042	404506102	3346423532459289088	16.02293±0.003016	0.8002±0.0681	32240±599	5.68±0.07	sdOB	0.257±0.004	-11.313±0.021	0.135±0.012	17.6 ^{+3.9} _{-0.10}	0.32 ^{+0.10} _{-0.21}
88.167219	32.93386	195804131	3398928751737464192	14.839789±0.002875	1.2968±0.038	80890±14690	5.58±0.12	sdO	0.959±0.016	-10.923±0.210	0.198±0.006	1513.7 ^{+1410.7} _{-895.9}	0.53 ^{+0.13} _{-0.13}
88.453881	39.023084	66503084	3451217092350738944	14.1348±0.003748	1.495±0.0262	30500±570	5.66±0.05	sdB	0.485±0.007	-10.787±0.067	0.241±0.004	45.2 ^{+4.1} _{-3.5}	0.97 ^{+0.15} _{-0.13}
89.391565	14.204803	2711101097	3456893264443563776	14.528431±0.002957	1.1823±0.0357	37240±635	5.59±0.06	sdOB	0.288±0.006	-11.051±0.025	0.168±0.005	48.2 ^{+5.4} _{-0.76}	0.40 ^{+0.07} _{-0.08}
89.559068	46.673715	604410009	197796403761616256	17.083685±0.002964	0.4264±0.0752	49310±1037	5.75±0.12	He-sdOB	0.178±0.001	-11.690±0.017	0.104±0.015	59.5 ^{+17.8} _{-10.6}	0.23 ^{+0.08} _{-0.08}
90.000993	11.476859	401508028	3342199204486994048	16.2485±0.002914	0.5891±0.0737	38530±734	5.57±0.11	He-sdB	0.401±0.009	-11.307±0.032	0.184±0.029	67.2 ^{+14.2} _{-14.2}	0.47 ^{+0.13} _{-0.13}
90.157054	36.799292	381508201	3456632255835216640	15.439364±0.002915	0.912±0.0456	26300±1290	5.30±0.15	sdB	0.361±0.006	-11.042±0.015	0.222±0.013	21.2 ^{+5.7} _{-4.3}	0.35 ^{+0.19} _{-0.10}
90.257966	42.511474	321109060	960904069540367232	15.25141±0.002892	0.9827±0.049	35770±626	5.90±0.07	sdOB	0.228±0.01	-11.214±0.007	0.137±0.007	27.3 ^{+3.0} _{-3.0}	0.54 ^{+0.09} _{-0.09}
92.166509	7.903821	526401140	3328247780618525568	15.035196±0.002825	0.948±0.0325	27850±675	5.47±0.06	sdB	0.498±0.017	-10.917±0.074	0.279±0.011	42.5 ^{+5.9} _{-5.1}	0.84 ^{+0.15} _{-0.10}
92.845585	55.870869	497610101	997207297787944064	15.780172±0.002862	0.6543±0.0418	29780±734	5.46±0.09	sdB	0.106±0.004	-11.312±0.012	0.162±0.011	18.3 ^{+5.6} _{-2.2}	0.28 ^{+0.08} _{-0.05}
93.024484	47.523367	546803066	969542451362654976	16.17961±0.002968	0.3094±0.06	47330±1004	5.05±0.11	He-sdOB	0.143±0.006	-11.524±0.013	0.211±0.037	199.7 ^{+153.7} _{-55.5}	0.19 ^{+0.14} _{-0.10}
93.23016	57.847462	679716210	999261490450160512	15.785784±0.004378	0.6262±0.0522	29270±626	5.43±0.06	sdB	0.069±0.001	-11.323±0.018	0.167±0.013	18.4 ^{+4.2} _{-3.2}	0.27 ^{+0.07} _{-0.07}
93.506638	11.061654	398805096	3330105641733251840	16.3754±0.002946	0.6779±0.056	31300±606	5.47±0.07	sdOB	0.646±0.015	-11.152±0.064	0.228±0.022	44.9 ^{+8.3} _{-8.3}	0.50 ^{+0.13} _{-0.10}
93.304375	34.933493	187212172	3452480293768439296	14.445072±0.002826	1.1252±0.0253	28970±630	5.49±0.08	sdB	0.296±0.009	-10.928±0.027	0.231±0.006	33.8 ^{+2.9} _{-2.9}	0.61 ^{+0.15} _{-0.11}
93.792659	35.854813	185915228	34529199960980353920	16.424997±0.002908	0.6433±0.0516	28610±630	5.68±0.07	sdB	0.277±0.004	-11.314±0.008	0.168±0.014	16.9 ^{+3.6} _{-2.8}	0.55 ^{+0.13} _{-0.10}
93.949651	34.780417	220504128	3452646281368418304	16.036396±0.003366	0.7985±0.0462	22640±788	5.71±0.09	sdB	0.296±0.007	-11.138±0.009	0.202±0.012	9.5 ^{+1.5} _{-1.5}	0.77 ^{+0.16} _{-0.16}
94.864687	35.382661	220504054	3452740362628172160	15.026524±0.002849	0.7352±0.0339	35590±602	5.53±0.06	sdOB	0.326±0.008	-11.108±0.014	0.235±0.011	79.8 ^{+8.6} _{-8.6}	0.69 ^{+0.13} _{-0.10}
95.6662806	46.542454	601111213	968469534172491648	14.748486±0.002818	1.0088±0.0356	27570±613	5.45±0.06	sdB	0.13±0.002	-11.060±0.006	0.192±0.007	19.1 ^{+2.1} _{-2.1}	0.37 ^{+0.06} _{-0.05}
95.688418	51.846152	551803036	995383482875359744	16.4484±0.002951	0.4627±0.053	32360±816	5.61±0.11	sdOB	0.119±0.005	-11.476±0.007	0.159±0.026	25.2 ^{+5.9} _{-4.9}	0.38 ^{+0.15} _{-0.15}
95.878258	33.022396	185907227	3439445854003662592	16.15886±0.002974	0.4539±0.0486	38500±1210	5.35±0.10	sdO	0.29±0.015	-11.372±0.009	0.206±0.030	82.5 ^{+27.1} _{-16.2}	0.35 ^{+0.11} _{-0.11}
96.176952	28.496275	332303054	3433651805682659200	17.194746±0.002998	0.4633±0.0906	32930±907	5.87±0.10	sdOB	0.205±0.006	-11.577±0.023	0.126±0.034	16.7 ^{+10.4} _{-5.0}	0.43 ^{+0.28} _{-0.15}
96.770481	34.969325	74716039	942463434178440576	14.409541±0.00288	1.2037±0.0286	25330±781	5.30±0.07	sdB	0.227±0.005	-10.906±0.028	0.227±0.006	19.0 ^{+5.9} _{-3.9}	0.37 ^{+0.09} _{-0.07}
97.001902	20.849289	274315180	3376012799112785408	15.790771±0.002897	0.3399±0.0445	76560±10754	5.10±0.22	He-sdO	0.402±0.031	-11.364±0.006	0.284±0.033	2548.3 ^{+1269.3} _{-1269.3}	0.37 ^{+0.06} _{-0.06}
97.152155	32.842084	74703090	3439296187280018432	14.68049±0.002945	0.7703±0.0384	43240±831	5.49±0.11	He-sdOB	0.214±0.009	-11.177±0.010	0.191±0.011	114.7 ^{+17.1} _{-12.3}	0.42 ^{+0.13} _{-0.10}
97.454305	22.414013	274411112	337646895898845312	15.400609±0.002899	0.6541±0.0389	28110±630	5.57±0.07	sdB	0.244±0.013	-11.136±0.030	0.248±0.016	34.8 ^{+5.4} _{-4.7}	0.82 ^{+0.21} _{-0.15}
97.640728	21.324502	274309125	3376057123175008256	15.29579±0.003164	0.8602±0.0411	21460±613	5.32±0.06	sdB	0.298±0.01	-10.989±0.031	0.260±0.012	12.9 ^{+1.8} _{-1.8}	0.51 ^{+0.08} _{-0.08}
97.865182	50.14843	551801179	968154867688361856	16.567343±0.002897	0.3386±0.0545	25350±915	5.34±0.09	sdB	0.118±0.004	-11.394±0.010	0.267±0.057	26.7 ^{+7.2} _{-7.2}	0.58 ^{+0.30} _{-0.17}
98.043207	28.178276	75709065	3434009173772378112	15.077774±0.002908	0.6738±0.0456	45110±831	5.44±0.10	He-sdOB	0.188±0.003	-11.279±0.011	0.173±0.035	110.6 ^{+20.5} _{-15.4}	0.30 ^{+0.10} _{-0.07}
98.397232	23.148759	220002038	33823403167310023368	15.488676±0.002927	0.5686±0.0516	46790±716	5.61±0.08	He-sdOB	0.174±0.006	-11.373±0.008	0.169±0.019	123.7 ^{+39.2} _{-29.2}	0.43 ^{+0.14} _{-0.10}
99.308942	42.381702	317915162	96803204208084992	17.218493±0.003082	0.577±0.0872	34870±722	5.97±0.09	sdOB	0.125±0.003	-11.652±0.041	0.085±0.018	9.6 ^{+4.1} _{-4.1}	0.24 ^{+0.15} _{-0.15}
99.660973	42.948122	475702062	964071899977558784	16.144976±0.002951	0.4874±0.0625	29760±626	5.37±0.06	sdB	0.113±0.001	-11.378±0.011	0.191±0.034	25.8 ^{+6.0} _{-6.0}	0.32 ^{+0.13} _{-0.13}
100.45235	42.805621	422811236	963881581386403072	14.17787±0.002873	1.1992±0.0344	28140±649	5.56±0.08	sdB	0.098±0.001	-10.975±0.005	0.197±0.006	22.0 ^{+2.6} _{-2.6}	0.52 ^{+0.12} _{-0.12}
100.62136	37.070349	206060056	943819308110646144	15.069308±0.002982	1.0127±0.0423	34830±654	5.82±0.11	sdOB	0.127±0.002	-11.127±0.009	0.130±0.005	22.4 ^{+2.4} _{-2.4}	0.41 ^{+0.09} _{-0.09}
100.81184	13.965445	415715194	3352890447538648064	14.97635±0.00338	1.0353±0.0308	32560±621	5.76±0.07	sdB	0.286±0.011	-11.074±0.024	0.181±0.007	33.0 ^{+3.3} _{-3.2}	0.68 ^{+0.14} _{-0.14}
100.88299	14.157209	415715176	3355897092143865088	14.80878±0.002883	1.1126±0.0308	32560±621	5.57±0.05	sdB	0.124±0.002	-11.067±0.006	0.169±0.006	42.8 ^{+4.2} _{-3.2}	0.39 ^{+0.06} _{-0.05}
100.948932	32.029482	438514106	937248901501446272	13.825026±0.002982	1.0644±0.0448	26880±569	5.21±0.05	sdB	0.124±0.002	-10.864±0.006	0.283±0.012	37.1 ^{+3.0} _{-3.0}	0.47 ^{+0.06} _{-0.06}
101.28447	21.304168	319005070	3378155777335873664	16.127935±0.003299	0.4384±0.0502	27260±621	5.30±0.08	sdB	0.155±0.014	-11.311±0.015	0.246±0.025	30.0 ^{+6.2} _{-6.2}	0.44 ^{+0.17} _{-0.11}
101.57652	29.337016	2604051	33866222158606040960	13.570652±0.002854	2.1179±0.0437	37930±669	6.00±0.07	sdB	0.094±0.003	-10.983±0.024	0.107±0.002	21.4 ^{+1.7} _{-1.7}	0.42 ^{+0.08} _{-0.08}

Table 1 continued on next page

Table 1 (continued)

RA	DEC	obs.id	source.id	<i>G</i>	parallax	T_{eff}	$\log g$	spclass	E(B-V)	Angular diameter	Radius	Luminosity	Mass
LAMOST (1)	LAMOST (2)	LAMOST (3)	<i>Gaia</i> EDR3 (4)	<i>Gaia</i> EDR3 (mag) (5)	<i>Gaia</i> EDR3 (mas) (6)	(<i>K</i>) (7)	(cm s^{-2}) (8)	(9)	(10)	log(rad) (11)	R/R_{\odot} (12)	L/L_{\odot} (13)	M/M_{\odot} (14)
101.79684	13.370346	387309021	3352595366104656384	17.358217±0.003094	0.7117±0.1165	35580±617	6.03±0.07	sdOB	0.265±0.015	-11.608±0.013	0.105±0.023	15.5±7.8	0.42±0.22
101.89525	13.836488	387309030	3352835983053282304	16.795809±0.003044	0.5558±0.0666	31770±606	6.06±0.07	sdB	0.185±0.008	-11.502±0.011	0.125±0.019	14.1±4.5	0.66±0.25
102.31712	38.572141	296103019	944390774983674496	15.493822±0.002905	0.7018±0.0473	33450±582	5.72±0.06	sdOB	0.104±0.003	-11.311±0.007	0.157±0.010	27.9±8.8	0.47±0.11
102.6132	16.662794	282306209	3358122782854938112	16.28432±0.002959	0.505±0.0554	28870±664	5.65±0.07	sdB	0.117±0.006	-11.400±0.057	0.174±0.017	18.8±4.4	0.50±0.19
103.09651	9.965476	392002223	3158419684195782656	14.2029±0.002906	1.2297±0.0471	70180±1884	5.78±0.06	sdO	0.179±0.005	-11.214±0.038	0.110±0.044	26.3±35.2	0.27±0.06
103.18157	40.293805	296115026	950627174872167808	14.110184±0.002857	0.6313±0.0373	68730±1308	5.22±0.06	He-sdO	0.071±0.001	-11.235±0.003	0.206±0.011	84.8±100.1	0.25±0.04
103.216529	29.006594	15710159	887620515740571264	14.770409±0.002854	0.9839±0.0387	32270±680	5.74±0.08	sdB	0.058±0.0	-11.180±0.005	0.150±0.005	22.0±2.9	0.44±0.08
103.24919	52.713839	545808061	993265067567138432	15.438828±0.002872	0.4672±0.038	31770±1344	5.04±0.15	sdB	0.051±0.001	-11.256±0.090	0.249±0.019	55.0±16.7	0.25±0.14
103.351374	33.059526	438511176	937565831431448192	12.087978±0.003466	2.2159±0.0554	33990±573	5.49±0.05	sdOB	0.091±0.002	-10.656±0.011	0.222±0.005	59.3±5.1	0.55±0.06
103.69431	24.82412	81505213	3381286602335612416	13.969696±0.002919	0.6725±0.0388	61260±2319	5.10±0.05	sdO	0.074±0.002	-11.190±0.007	0.214±0.014	579.9±100.2	0.21±0.04
103.80732	15.948556	422403108	3355060020198388480	16.413248±0.002944	0.4089±0.0696	29400±704	5.40±0.14	sdB	0.1±0.003	-11.435±0.021	0.201±0.042	26.5±12.9	0.35±0.27
103.88743	22.063784	95406046	3378454092881858816	13.688599±0.002877	1.7044±0.0475	47580±1096	5.69±0.08	sdOB	0.065±0.001	-11.091±0.023	0.106±0.003	51.2±6.2	0.20±0.05
104.47756	12.242259	392004058	3160786559070298880	15.67552±0.002891	0.6601±0.0517	50480±963	5.50±0.09	sdO	0.12±0.006	-11.458±0.008	0.117±0.011	79.8±13.4	0.16±0.05
104.56965	9.728642	29001011	3157967411257049728	13.570471±0.002954	0.7864±0.0364	36690±1245	5.01±0.09	sdOB	0.13±0.004	-10.942±0.006	0.318±0.017	165.4±28.3	0.37±0.11
105.2623	9.693231	507814235	3157919887443293952	17.018484±0.003043	0.5514±0.0788	23300±831	5.56±0.08	sdB	0.118±0.005	-11.450±0.012	0.141±0.028	5.3±2.4	0.27±0.13
105.34676	53.493837	545813031	98172582818800128	14.919451±0.002865	0.3924±0.0431	73480±4515	5.07±0.14	He-sdO	0.042±0.001	-11.420±0.005	0.215±0.021	1215.1±350.8	0.20±0.06
105.449625	28.568161	21003121	884393900085830144	14.8787±0.002865	0.6323±0.0348	26710±754	5.40±0.10	sdB	0.082±0.003	-11.097±0.007	0.277±0.014	35.6±6.6	0.69±0.16
105.56337	12.29816	392009130	3160836861727862400	14.722439±0.002934	0.9351±0.0418	27110±698	5.41±0.06	sdB	0.078±0.006	-11.076±0.019	0.156±0.010	18.8±2.9	0.36±0.09
105.73661	17.391982	372812146	3361273433424723712	15.765791±0.002898	0.68±0.0494	29210±590	5.58±0.06	sdB	0.056±0.001	-11.332±0.008	0.156±0.012	15.7±2.3	0.33±0.06
105.77822	19.537799	174905039	336490572999194880	15.898383±0.002894	0.3748±0.0531	37730±947	5.40±0.09	sdB	0.062±0.003	-11.456±0.005	0.203±0.023	75.6±18.7	0.39±0.20
106.31091	22.355964	174911065	3367827072481260416	15.09628±0.002903	0.8071±0.0432	28550±630	5.62±0.06	sdB	0.046±0.001	-11.198±0.006	0.174±0.010	17.7±2.3	0.46±0.10
106.64127	9.090862	507803187	3154729899269006336	16.323244±0.002915	0.4501±0.0517	28260±613	5.37±0.06	sdB	0.105±0.005	-11.394±0.016	0.199±0.025	22.6±7.0	0.34±0.10
106.82751	14.016182	372807096	3161497015379649280	15.402214±0.002927	0.7705±0.0555	39820±1157	5.61±0.09	sdOB	0.058±0.001	-11.385±0.010	0.121±0.009	32.8±5.7	0.22±0.06
107.11835	44.426357	436410091	953141929764017408	16.274355±0.002899	0.6622±0.0533	38760±939	5.98±0.48	He-sdB	0.091±0.003	-11.493±0.012	0.107±0.008	23.4±6.0	0.40±0.89
107.27312	22.595127	616616046	3368172319132367104	16.134527±0.002902	0.451±0.0556	48480±2631	5.48±0.07	sdO	0.056±0.003	-11.574±0.011	0.130±0.021	84.6±36.2	0.18±0.07
107.72217	56.412373	687616080	988436459174352512	14.624264±0.002856	0.9733±0.0521	41280±781	5.80±0.09	sdO	0.047±0.0	-11.242±0.005	0.132±0.006	46.1±5.9	0.40±0.14
108.01	11.559014	128701029	3159937564294110080	12.442865±0.002808	2.54±0.0549	25790±587	5.43±0.05	sdB	0.158±0.004	-10.569±0.045	0.235±0.005	21.9±2.4	0.54±0.08
108.22018	42.643905	316516061	949617548319629824	16.126808±0.002974	0.4884±0.0592	47000±1454	5.71±0.07	sdO	0.061±0.001	-11.565±0.009	0.121±0.013	64.6±24.6	0.28±0.09
108.27216	18.417765	267011180	3363070035424348800	15.826177±0.002917	0.7481±0.0559	27180±728	5.80±0.05	sdB	0.105±0.003	-11.281±0.042	0.152±0.011	11.4±1.9	0.53±0.09
108.31042	17.582952	267015014	3360729067791609216	15.980993±0.002955	0.5721±0.0581	29520±728	5.60±0.06	sdB	0.154±0.003	-11.323±0.021	0.185±0.020	23.2±6.5	0.49±0.15
108.33188	38.127736	187812147	946428174325145856	16.661816±0.003051	0.4246±0.0709	39780±1088	5.58±0.13	He-sdB	0.045±0.001	-11.609±0.014	0.125±0.017	34.9±15.8	0.22±0.14
108.5057	69.559596	601216092	1109216024779190016	16.1673±0.002816	0.3794±0.0445	37890±728	5.52±0.08	He-sdOB	0.038±0.002	-11.536±0.009	0.172±0.021	53.6±15.2	0.35±0.14
108.6558	26.786667	281105033	88333730358019584	15.808328±0.002894	0.2938±0.0487	24650±635	5.07±0.13	sdB	0.049±0.002	-11.284±0.094	0.391±0.078	51.1±14.1	0.64±0.23
109.73439	10.44399	446310014	315657359750882944	15.766756±0.002967	0.8986±0.0617	31080±680	5.47±0.10	He-sdOB	0.072±0.003	-11.370±0.030	0.106±0.008	9.5±1.3	0.12±0.04
109.740975	2.887462	492402100	3139042514040855296	14.870437±0.00287	0.6932±0.0318	26300±587	5.23±0.05	sdB	0.101±0.006	-11.084±0.028	0.266±0.013	30.2±4.9	0.45±0.08
109.84141	5.16679	492414173	3140714527629703552	16.356464±0.003073	0.474±0.0641	35180±621	5.79±0.14	sdOB	0.105±0.004	-11.510±0.013	0.146±0.019	29.2±7.2	0.47±0.16
110.666731	9.231818	369611044	3155626997678101248	13.031905±0.002885	1.9843±0.0532	42400±2087	5.79±0.10	sdOB	0.045±0.001	-10.982±0.020	0.117±0.003	63.6±15.1	0.31±0.08
110.96446	30.321259	214908131	885963418573729792	15.01771±0.002888	1.3041±0.0534	38200±596	5.91±0.07	sdOB	0.058±0.002	-11.232±0.008	0.099±0.005	9.8±1.2	0.29±0.06
110.995849	4.499076	492404174	3139698956841267456	15.378058±0.002841	0.546±0.0432	29850±568	5.26±0.06	sdB	0.089±0.006	-11.224±0.050	0.225±0.016	36.3±7.5	0.34±0.06
111.22127	19.391139	270103045	3362730178953977472	14.653339±0.002852	0.9218±0.0378	26520±577	5.53±0.05	sdB	0.051±0.002	-11.073±0.004	0.199±0.008	17.6±2.1	0.49±0.10
111.2289	15.280799	397603157	3167124522048560128	15.523512±0.002923	0.7275±0.047	32490±692	5.88±0.09	sdOB	0.081±0.002	-11.312±0.010	0.148±0.010	21.7±3.3	0.59±0.21

Table 1 continued on next page

Table 1 (continued)

RA	DEC	obs.id	source.id	G	parallax	T_{eff}	$\log g$	spclass	E(B-V)	Angular diameter	Radius	Luminosity	Mass
LAMOST (1)	LAMOST (2)	LAMOST (3)	Gaia EDR3 (4)	Gaia EDR3 (mag) (5)	Gaia EDR3 (mas) (6)	(K) (7)	(cm s^{-2}) (8)	(9)	(10)	log(rad) (11)	R/R_{\odot} (12)	L/L_{\odot} (13)	M/M_{\odot} (14)
111.25613	27.055098	606410248	872695092069071360	16.161148±0.00297	0.69833±0.0622	31890±704	5.57±0.13	sdB	0.05±0.001	-11.4665±0.035	0.106±0.011	10.4±2.4	0.15±0.04
111.39693	51.847694	617015027	1142701823200960512	15.033071±0.002806	0.7912±0.0329	36490±582	5.82±0.12	sdOB	0.038±0.0	-11.296±0.005	0.142±0.006	32.1±3.4	0.50±0.18
111.42846	52.723794	448315232	986474685615378816	15.289351±0.002908	0.8527±0.0453	25000±590	5.50±0.06	sdB	0.059±0.001	-11.168±0.011	0.180±0.011	11.2±1.4	0.37±0.07
111.65522	8.558556	446301096	3143342600936696960	15.014175±0.002958	0.8685±0.0439	29920±579	5.64±0.06	sdB	0.047±0.002	-11.204±0.005	0.210±0.017	32.1±5.7	0.71±0.16
112.103	41.831571	320613193	948767385313600128	15.710246±0.002887	0.4243±0.0456	38230±649	5.71±0.08	He-sdOB	0.067±0.004	-11.423±0.042	0.197±0.029	75.4±24.9	0.71±0.30
112.207639	2.233514	600415096	3135810671409226368	15.96779±0.002904	0.5093±0.0527	31090±654	5.56±0.12	sdB	0.12±0.007	-11.361±0.008	0.188±0.016	29.9±5.9	0.47±0.13
112.88153	20.756841	270109111	864917013671899648	15.61999±0.002887	0.6425±0.0542	50930±2116	5.50±0.11	sdO	0.04±0.001	-11.493±0.030	0.111±0.012	73.8±19.8	0.15±0.04
113.065169	6.203372	492412181	3141525486172958336	15.910931±0.002876	0.622±0.0595	28910±590	5.54±0.09	sdB	0.052±0.001	-11.358±0.008	0.157±0.014	15.7±4.0	0.32±0.12
113.08392	27.069038	21602071	872322087046515840	16.608788±0.002966	0.475±0.0709	36640±1054	5.91±0.11	He-sdOB	0.051±0.002	-11.602±0.009	0.1117±0.014	22.5±5.8	0.41±0.13
113.35669	36.882668	331004092	898625493262383104	15.077509±0.002843	1.2158±0.0402	33110±570	5.94±0.06	sdB	0.047±0.001	-11.260±0.006	0.100±0.004	10.7±1.3	0.31±0.06
113.69226	34.355805	75815079	893594510306886784	15.442548±0.002918	0.5125±0.0573	26400±741	5.25±0.06	sdB	0.063±0.007	-11.224±0.028	0.133±0.026	29.6±10.5	0.43±0.17
113.898132	2.969486	600412059	3135525623021849088	15.930572±0.002845	0.5644±0.0501	37090±592	5.71±0.09	sdOB	0.049±0.002	-11.472±0.016	0.133±0.017	30.0±8.8	0.33±0.11
114.182985	-3.195907	436206051	3060798513530161920	13.73426±0.002805	1.2077±0.035	28890±692	5.54±0.06	sdB	0.075±0.002	-10.910±0.011	0.225±0.007	31.6±3.3	0.64±0.12
114.30941	25.098511	228001126	868529562204066688	15.511215±0.0029	0.4801±0.045	26760±698	5.28±0.08	sdB	0.042±0.001	-11.253±0.006	0.256±0.029	30.0±8.8	0.46±0.14
114.48439	31.279597	91905056	880252005422941440	13.553999±0.006624	1.3194±0.0335	31000±635	5.49±0.07	sdB	0.044±0.001	-10.917±0.021	0.198±0.005	32.5±3.5	0.44±0.09
114.51894	26.412458	73906248	869050009160765056	14.568084±0.002896	0.873±0.0449	27730±868	5.55±0.09	sdB	0.039±0.001	-11.092±0.015	0.205±0.011	22.4±3.3	0.54±0.17
114.63907	51.47903	448308129	98279822026188928	15.616516±0.002864	0.611±0.044	26880±692	5.45±0.08	sdB	0.061±0.001	-11.262±0.015	0.198±0.017	18.4±4.4	0.40±0.10
115.09819	20.826954	176203116	67305856816796288	15.52251±0.002969	0.5818±0.0528	33560±582	5.76±0.06	sdOB	0.039±0.004	-11.363±0.030	0.164±0.017	30.9±3.0	0.57±0.16
115.10468	15.8663	499603225	3165813590653493760	17.033026±0.003079	0.4053±0.0808	32430±868	6.21±0.13	sdB	0.028±0.0	-11.656±0.011	0.121±0.019	14.7±3.4	0.85±0.34
116.14643	30.352421	120407017	879166065892619904	14.725154±0.002859	0.8052±0.0407	29100±664	5.45±0.08	sdB	0.039±0.001	-11.141±0.005	0.193±0.009	24.0±3.0	0.38±0.07
116.28351	38.18521	279210190	919963474904219776	14.826072±0.002885	0.6169±0.0373	29310±626	5.30±0.08	sdB	0.039±0.001	-11.156±0.011	0.247±0.013	41.0±7.4	0.44±0.11
116.46916	25.85761	183702062	86881794388022016	14.73376±0.002916	0.7626±0.0434	26210±617	5.47±0.06	sdB	0.033±0.001	-11.096±0.005	0.237±0.015	23.7±4.0	0.60±0.15
116.5139	33.743557	273608236	882125367078828672	14.977926±0.002814	0.6062±0.0363	26480±613	5.22±0.06	sdB	0.042±0.002	-11.141±0.004	0.269±0.018	31.7±4.2	0.44±0.09
116.55484	33.552105	120412018	882087811884800896	15.840804±0.002863	0.3535±0.0501	46150±795	5.51±0.12	He-sdOB	0.042±0.002	-11.524±0.007	0.188±0.024	143.2±51.9	0.40±0.21
117.04874	13.730365	417207114	3164383748798177792	15.642965±0.002918	0.7176±0.0588	22940±1088	5.36±0.16	sdB	0.03±0.0	-11.228±0.012	0.182±0.016	8.2±2.4	0.27±0.18
117.21696	45.817713	405304165	927227948229851392	16.04589±0.002896	0.478±0.0464	27690±767	5.74±0.09	sdB	0.051±0.002	-11.374±0.007	0.194±0.017	20.2±4.2	0.79±0.21
117.23262	30.713059	120407139	879237740307303040	14.046156±0.003012	1.361±0.0322	31080±572	5.65±0.06	sdB	0.041±0.001	-11.033±0.035	0.150±0.004	18.9±1.9	0.37±0.06
117.26186	12.803115	407409236	3152255890729006848	16.650686±0.002868	0.3401±0.0613	37580±1012	5.53±0.10	sdB	0.025±0.0	-11.632±0.007	0.155±0.031	42.4±21.2	0.30±0.10
117.91362	6.768001	120510204	3144058245567712512	13.486943±0.002821	1.2486±0.0459	39600±570	5.61±0.09	He-sdOB	0.019±0.0	-11.035±0.004	0.163±0.006	58.1±4.7	0.39±0.15
118.1429	16.268133	414013194	666988874675710464	14.450037±0.00282	0.7114±0.0513	50420±907	5.67±0.11	He-sdOB	0.024±0.001	-11.318±0.013	0.164±0.014	156.7±31.4	0.46±0.17
118.30847	11.211171	605805093	315070732898463616	15.587963±0.003622	0.5042±0.0475	29360±568	5.42±0.05	sdB	0.024±0.0	-11.318±0.013	0.212±0.016	30.1±7.5	0.44±0.12
118.47597	25.519389	173809084	873767017124252544	15.666527±0.002869	0.5619±0.0448	33540±931	5.86±0.07	sdOB	0.052±0.005	-11.378±0.022	0.165±0.017	31.1±5.1	0.71±0.21
118.55157	29.832504	2711238	877431345781684480	14.585556±0.002872	1.0882±0.0451	31270±1157	5.82±0.19	sdB	0.039±0.002	-11.136±0.004	0.151±0.005	19.8±3.9	0.56±0.38
119.01571	22.441942	173807064	674255203425267584	14.177251±0.002876	1.0823±0.0445	65800±1528	5.48±0.05	sdO	0.049±0.001	-11.268±0.013	0.111±0.005	205.1±22.1	0.13±0.02
119.29932	13.752347	392702198	654222239006166656	15.905103±0.002865	0.5669±0.0529	36110±1062	5.99±0.17	sdOB	0.029±0.001	-11.475±0.005	0.129±0.013	25.2±6.5	0.61±0.33
119.53142	-4.534807	170213155	3068507812327598208	13.043116±0.002849	1.7568±0.0429	41370±568	5.87±0.09	He-sdOB	0.043±0.001	-10.946±0.007	0.144±0.004	54.3±4.7	0.57±0.11
119.845827	16.767125	18216091	967308798199419776	14.404426±0.002821	0.5668±0.0428	38880±1062	5.17±0.09	sdO	0.031±0.001	-11.191±0.024	0.253±0.023	129.9±32.7	0.33±0.10
119.93739	37.250873	285607170	907291264093243520	16.26833±0.002871	0.5121±0.0554	33980±686	5.82±0.09	He-sdOB	0.042±0.002	-11.512±0.020	0.133±0.018	21.3±3.7	0.43±0.17
120.63138	39.374639	279209235	921064055980216320	15.167146±0.00288	0.5041±0.0478	35770±610	5.47±0.07	sdOB	0.036±0.001	-11.320±0.007	0.210±0.012	66.1±12.2	0.48±0.15
120.86637	34.361297	78615208	905650346067635968	15.04674±0.00287	0.5845±0.0451	39300±698	5.43±0.07	sdO	0.042±0.002	-11.317±0.005	0.185±0.013	73.8±11.3	0.34±0.09
121.61706	32.516504	78608160	90215492988483456	15.373613±0.002918	0.7481±0.0458	32930±613	5.65±0.09	sdB	0.045±0.001	-11.314±0.010	0.144±0.009	21.8±5.2	0.34±0.10

Table 1 continued on next page

Table 1 (continued)

RA	DEC	obs.id	source.id	G	parallax	T_{eff}	$\log g$	spclass	E(B-V)	Angular diameter	Radius	Luminosity	Mass
LAMOST (1)	LAMOST (2)	LAMOST (3)	Gaia EDR3 (4)	Gaia EDR3 (mag) (5)	Gaia EDR3 (mas) (6)	(K) (7)	(cm s^{-2}) (8)	(9)	(10)	log(rad) (11)	R/R_{\odot} (12)	L/L_{\odot} (13)	M/M_{\odot} (14)
121.61938	24.349293	103802062	680914734899282560	14.983982±0.00292	0.7281±0.0503	28190±621	5.50±0.06	sdB	0.039±0.002	-11.170±0.004	0.210±0.017	24.7±5.6	0.51±0.13
121.73617	15.455543	392709195	65486682340111168	14.75256±0.003005	0.6909±0.038	29030±613	5.47±0.06	sdB	0.028±0.001	-11.150±0.014	0.227±0.014	33.0±5.4	0.55±0.12
121.99274	27.409538	2001056	683766356962547840	14.092126±0.002872	0.764±0.0512	38780±846	5.39±0.12	sdO	0.028±0.0	-11.130±0.016	0.217±0.014	96.7±16.3	0.41±0.18
122.34152	16.144793	392712156	65642809850193664	15.716009±0.002851	0.4329±0.0447	37730±1218	5.54±0.14	sdB	0.026±0.002	-11.445±0.023	0.180±0.023	59.±18.6	0.41±0.20
123.14029	16.023232	227309093	655674865665718666	13.673504±0.002854	1.2438±0.0463	31350±579	5.52±0.05	sdB	0.037±0.002	-10.964±0.003	0.188±0.008	30.8±3.8	0.43±0.07
123.243814	0.731455	641316208	3089571878131968792	14.574138±0.002839	0.7474±0.047	28390±659	5.42±0.06	sdB	0.026±0.001	-11.106±0.004	0.234±0.014	32.0±4.6	0.52±0.16
123.88002	24.872947	404606240	682305655764689408	16.328789±0.002926	0.4486±0.0673	35360±876	5.55±0.11	sdB	0.039±0.001	-11.539±0.009	0.140±0.027	27.±6.9	0.25±0.14
124.735819	39.901597	642010128	909317797165729024	14.917613±0.00284	0.896±0.041	22910±602	5.44±0.09	sdB	0.041±0.001	-11.075±0.007	0.210±0.012	11.0±1.8	0.45±0.13
124.82385	42.560752	318008007	915859960070594176	16.220505±0.002995	0.4986±0.0634	32880±592	6.10±0.06	sdOB	0.054±0.001	-11.481±0.012	0.144±0.012	21.7±4.9	0.98±0.26
124.998525	22.6836111	602216224	676607952150024448	15.619679±0.002837	0.7931±0.0525	31300±592	5.69±0.09	sdB	0.042±0.001	-11.346±0.038	0.128±0.009	14.0±1.8	0.29±0.06
125.2234083	0.1455028	641315139	3077510098136276480	15.158632±0.003153	0.6822±0.0477	29030±572	5.65±0.05	sdB	0.034±0.0	-11.219±0.006	0.194±0.016	23.7±5.0	0.62±0.12
125.917117	8.327003	334913110	599294211494840704	14.683098±0.002989	0.8072±0.0448	28110±613	5.74±0.07	sdB	0.025±0.001	-11.121±0.039	0.211±0.012	24.7±5.0	0.90±0.22
126.190367	23.255656	602216150	678116344664890368	15.318593±0.002836	0.6146±0.055	29900±606	5.47±0.06	sdB	0.032±0.001	-11.274±0.005	0.187±0.014	25.1±4.1	0.37±0.09
126.89565	17.898859	268107224	662146419308286976	14.558397±0.002808	1.1357±0.0438	29460±599	5.64±0.06	sdB	0.033±0.001	-11.109±0.006	0.154±0.007	16.0±2.2	0.38±0.07
127.136949	14.867359	380214234	651745279826458112	11.620548±0.002834	3.7728±0.055	38230±584	5.81±0.05	He-sdOB	0.034±0.001	-10.642±0.007	0.131±0.002	32.8±2.7	0.41±0.06
127.5257	47.864096	302901126	930769616916994048	16.039906±0.002874	0.4869±0.0538	27030±1131	5.57±0.11	sdB	0.033±0.001	-11.363±0.008	0.194±0.027	17.8±4.2	0.50±0.14
128.51254	7.202881	340409136	595824702553000448	14.659434±0.00286	0.9332±0.0402	29550±579	5.64±0.05	sdB	0.027±0.0	-11.139±0.038	0.170±0.008	19.9±2.7	0.46±0.09
128.849472	-1.931296	183405148	3073231760935363264	11.371105±0.002813	2.6532±0.0462	46270±654	5.88±0.06	He-sdOB	0.025±0.001	-10.645±0.004	0.187±0.005	143.6±11.4	0.96±0.18
128.898243	19.736805	399207128	662848427026938240	13.076024±0.002823	1.5645±0.0543	27170±716	5.41±0.07	sdB	0.025±0.0	-10.784±0.004	0.231±0.007	26.1±3.8	0.51±0.15
129.016533	15.870972	43203186	657873717121550976	15.378343±0.002837	0.7283±0.0443	26790±747	5.56±0.08	sdB	0.027±0.001	-11.231±0.004	0.178±0.013	14.7±1.9	0.42±0.11
129.050164	19.298929	431714232	662771594747150976	15.689806±0.00289	0.5645±0.0652	35310±734	5.49±0.09	sdOB	0.022±0.001	-11.398±0.051	0.154±0.017	33.5±5.3	0.26±0.10
129.0820292	20.9636028	699412249	664631178147534720	16.308779±0.002912	0.5478±0.0878	31370±716	5.52±0.12	sdB	0.033±0.001	-11.490±0.029	0.128±0.005	14.4±1.2	0.20±0.13
129.24905	10.631478	420802086	601444306482580992	15.165354±0.002848	0.7113±0.0504	27030±630	5.52±0.06	sdB	0.03±0.002	-11.192±0.004	0.198±0.017	18.6±2.9	0.47±0.13
130.255486	39.938389	642006098	911573758803336960	15.425313±0.002817	0.7404±0.0437	29380±582	5.69±0.06	sdB	0.032±0.001	-11.283±0.007	0.157±0.012	16.6±2.0	0.45±0.11
130.432816	13.075019	380207118	603097422215268736	13.60113±0.002821	0.7819±0.0375	46930±659	5.53±0.08	He-sdOB	0.045±0.002	-11.079±0.004	0.237±0.011	244.7±28.9	0.69±0.15
130.770989	33.462441	199614008	710337051880367616	14.8973±0.002828	0.7268±0.0413	27360±774	5.47±0.06	sdB	0.028±0.001	-11.144±0.005	0.222±0.011	24.9±3.6	0.54±0.09
130.870297	8.410645	503814238	597102541222525056	16.42204±0.002832	0.5215±0.0612	25720±710	5.64±0.07	sdB	0.043±0.003	-11.417±0.005	0.163±0.023	10.5±2.3	0.42±0.18
130.919521	2.007572	449410221	3078888851357039360	14.019052±0.002803	0.8532±0.0436	42780±1210	5.28±0.07	sdO	0.072±0.005	-11.119±0.010	0.197±0.012	117.8±19.2	0.27±0.06
131.39858	19.697389	535915112	661156102927711104	13.248145±0.0028	1.0432±0.0306	23510±572	5.07±0.05	sdB	0.023±0.001	-10.768±0.012	0.372±0.013	37.5±4.3	0.60±0.08
131.499846	-2.658236	302304166	3072185163322482816	15.707915±0.002815	0.5919±0.0521	32540±963	5.86±0.11	sdB	0.021±0.001	-11.387±0.007	0.156±0.016	24.8±4.7	0.64±0.26
131.82875	23.0086	316011216	689367475352913280	15.271796±0.002834	0.6117±0.0552	29080±704	5.49±0.05	sdB	0.018±0.001	-11.076±0.005	0.206±0.005	27.0±2.5	0.47±0.07
132.677077	2.76284	449404224	579799175230073728	15.589573±0.002834	0.4183±0.0482	30870±610	5.52±0.10	sdB	0.026±0.0	-11.355±0.007	0.208±0.028	35.0±10.9	0.51±0.24
133.348574	16.826456	116809080	611684298790301568	13.918414±0.002806	1.2519±0.0467	27820±602	5.33±0.06	sdB	0.026±0.0	-11.289±0.017	0.221±0.038	37.7±7.1	0.57±0.21
134.205286	17.020746	116812014	611587919724027392	12.785231±0.002793	1.8709±0.0383	29080±704	5.41±0.06	sdB	0.018±0.0	-10.965±0.003	0.195±0.009	20.4±2.0	0.36±0.06
134.47774	38.314391	711713027	719606175420853888	15.663792±0.002849	0.4696±0.0518	30870±610	5.52±0.10	sdB	0.026±0.0	-11.355±0.007	0.208±0.028	35.0±10.9	0.51±0.24
134.71299	2.170267	109804103	577763368640517760	13.620108±0.00281	1.6429±0.0418	48090±1584	5.62±0.08	sdO	0.034±0.001	-11.091±0.011	0.108±0.003	56.0±6.4	0.18±0.03
134.761016	11.94105	93916015	604794342318395520	15.425232±0.002787	1.8635±0.0338	28770±669	5.61±0.06	sdB	0.024±0.002	-10.840±0.007	0.172±0.003	11.8±1.3	0.44±0.07
136.199038	31.547997	28303115	71177383869959296	15.104003±0.002819	0.7845±0.0546	38250±704	5.62±0.05	He-sdOB	0.018±0.0	-11.346±0.005	0.126±0.003	30.6±6.2	0.25±0.08
136.272592	5.550386	424616225	58037234853200664	14.054273±0.003237	1.2267±0.0529	41170±565	5.60±0.05	He-sdOB	0.041±0.002	-11.132±0.008	0.133±0.006	45.8±4.9	0.26±0.04
136.4204	12.207931	531216109	604474251290699776	14.597474±0.002811	0.8874±0.0392	28570±575	5.47±0.06	sdB	0.016±0.001	-11.114±0.004	0.191±0.011	22.0±2.4	0.39±0.07
136.783847	-3.103886	495812004	5762960596350664832	11.86401±0.002823	1.9776±0.0574	48630±1281	5.47±0.07	He-sdOB	0.017±0.0	-10.753±0.004	0.194±0.006	189.1±22.7	0.41±0.08

Table 1 continued on next page

Table 1 (continued)

RA	DEC	obs.id	source.id	<i>G</i>	parallax	T_{eff}	$\log g$	spclass	E(B-V)	Angular diameter	Radius	Luminosity	Mass
LAMOST (1)	LAMOST (2)	LAMOST (3)	<i>Gaia</i> EDR3 (4)	<i>Gaia</i> EDR3 (mag) (5)	<i>Gaia</i> EDR3 (mas) (6)	(<i>K</i>) (7)	(cm s^{-2}) (8)	(9)	(10)	log(rad) (11)	R/R_{\odot} (12)	L/L_{\odot} (13)	M/M_{\odot} (14)
137.58958	59.50939	209716167	1039246845702047360	15.32735±0.002823	1.3258±0.049	73690±7571	6.97±0.33	sdO	0.037±0.001	-11.512±0.009	0.052±0.002	69.1±40.8	0.96±1.24
137.605977	12.140855	94009080	604238612204857088	13.912457±0.00281	1.1488±0.035	27430±575	5.36±0.05	sdB	0.023±0.001	-10.956±0.034	0.217±0.007	24.0±5.7	0.39±0.50
138.03039	16.222359	200801161	607895838520616704	13.791821±0.002805	0.8688±0.043	39490±1139	5.37±0.06	sdO	0.031±0.002	-11.069±0.005	0.218±0.012	103.5±14.0	0.41±0.08
138.215253	27.342056	44602153	695059062934110592	12.183534±0.002831	3.6237±0.063	36700±577	5.96±0.07	He-sdOB	0.026±0.001	-10.741±0.005	0.111±0.002	20.0±1.7	0.41±0.07
138.536147	3.967868	424604230	578986163009656320	15.424299±0.002804	0.5274±0.056	29420±675	5.52±0.09	sdB	0.041±0.002	-11.276±0.027	0.221±0.006	33.0±3.2	0.60±0.23
138.779524	18.787857	554312158	635660764741010304	15.858203±0.002829	0.3601±0.0545	27270±741	5.05±0.07	sdB	0.027±0.002	-11.343±0.006	0.286±0.038	40.4±9.2	0.34±0.10
140.36756	2.767307	101704108	3845583703883921920	13.283801±0.002819	2.1328±0.0484	31610±613	5.84±0.06	sdB	0.036±0.002	-10.891±0.010	0.133±0.004	16.1±1.5	0.44±0.08
140.528329	8.325203	223715183	587484528898551552	15.578993±0.002877	0.716±0.0588	32160±722	6.01±0.13	sdB	0.044±0.002	-11.350±0.059	0.141±0.011	18.8±4.2	0.75±0.30
140.665973	27.040402	100508062	694109462844643072	12.593493±0.002802	2.9732±0.0667	31770±569	5.89±0.05	sdB	0.02±0.001	-10.769±0.008	0.128±0.003	15.0±1.4	0.47±0.06
140.805888	29.449328	11307210	69572684449223040	14.687137±0.002855	1.3063±0.0519	30870±639	6.24±0.09	sdOB	0.018±0.001	-11.166±0.007	0.118±0.005	11.5±1.3	0.89±0.17
140.978208	36.393264	213108067	810691780249660800	15.641441±0.002961	0.6313±0.0363	34210±621	5.62±0.08	sdOB	0.012±0.001	-11.412±0.006	0.136±0.014	22.5±7.4	0.29±0.10
141.167117	30.836992	189207170	700362419831670016	14.556747±0.003	0.8259±0.0513	40480±579	5.46±0.25	He-sdOB	0.022±0.001	-11.241±0.004	0.153±0.011	56.6±8.8	0.25±0.22
141.196371	23.321494	275512146	639171814606295424	15.756526±0.002841	0.4774±0.0529	26010±602	5.49±0.05	sdB	0.028±0.001	-11.282±0.148	0.238±0.031	23.3±7.2	0.64±0.22
142.233763	6.276275	223707059	586043309672965888	14.08088±0.002807	1.1569±0.0347	27240±584	5.47±0.05	sdB	0.044±0.001	-10.974±0.003	0.207±0.007	21.3±3.3	0.47±0.07
142.564419	30.842911	556014133	697406932576439680	14.852041±0.002825	0.929±0.0471	29100±587	5.67±0.06	sdB	0.019±0.001	-11.168±0.005	0.164±0.009	17.4±2.5	0.46±0.08
142.694923	48.273269	208410025	825628714431805056	10.640029±0.002814	4.256±0.0617	45830±722	5.78±0.08	He-sdOB	0.008±0.001	-10.505±0.004	0.163±0.002	105.5±7.4	0.58±0.10
142.74847	2.842343	206408094	384466157225496064	14.926293±0.002816	0.937±0.0407	31340±602	5.58±0.05	sdB	0.049±0.002	-11.206±0.047	0.147±0.006	18.6±1.9	0.29±0.10
143.800665	31.166785	22603091	697707958245002880	15.612009±0.002827	0.4789±0.063	33660±630	5.85±0.07	sdOB	0.017±0.001	-11.395±0.006	0.191±0.028	41.8±14.7	0.94±0.39
143.922229	16.353044	32106171	619153556155078272	14.705356±0.002848	1.1802±0.0546	30320±566	5.47±0.06	sdB	0.029±0.001	-11.134±0.053	0.136±0.005	14.1±1.9	0.20±0.23
144.249525	38.122706	342411212	800799439774706560	15.41011±0.002827	0.6357±0.0467	26820±1045	5.60±0.10	sdB	0.012±0.001	-11.246±0.004	0.197±0.017	17.9±3.2	0.57±0.19
144.3178	18.419783	142410002	633011250955383168	13.075914±0.002837	1.5666±0.0467	35260±599	5.60±0.06	sdB	0.025±0.001	-10.901±0.004	0.174±0.006	41.7±3.7	0.43±0.05
144.543089	-3.999546	408905050	3824642199263291136	14.652945±0.002798	0.7751±0.0537	34410±635	5.87±0.06	sdOB	0.038±0.001	-11.195±0.040	0.187±0.015	43.6±8.9	0.94±0.25
145.729342	6.593786	341903193	3853346290335592320	13.667614±0.002809	1.2462±0.0429	26740±680	5.51±0.06	sdB	0.029±0.001	-10.895±0.010	0.224±0.009	23.0±2.5	0.60±0.11
145.815892	16.932532	526902074	6205669740057395840	16.142424±0.002833	0.3672±0.0575	28560±781	5.53±0.09	sdB	0.024±0.001	-11.407±0.043	0.235±0.055	33.5±17.0	0.72±0.37
145.977337	27.783209	447313409	648029239761019776	13.196795±0.002816	1.5588±0.0439	30570±621	5.51±0.05	sdB	0.018±0.001	-10.862±0.003	0.194±0.006	19.3±9.5	0.46±0.06
146.299391	-3.155844	408906081	3826259821385575296	13.957952±0.002868	1.9083±0.0442	40330±761	6.24±0.06	sdO	0.037±0.003	-11.110±0.007	0.089±0.002	19.0±1.6	0.51±0.07
146.872334	27.274173	388912003	647193232966817280	16.59871±0.002862	0.4529±0.0695	29550±649	5.57±0.08	sdB	0.028±0.001	-11.524±0.006	0.147±0.018	14.9±3.8	0.29±0.16
147.74187	18.438487	142508056	627130616093753600	16.0874±0.002908	0.6382±0.0838	34560±617	5.89±0.09	sdOB	0.022±0.001	-11.489±0.041	0.115±0.019	16.9±3.6	0.37±0.20
147.75537	3.7991754	709312041	3849462024992532608	15.866466±0.002817	0.4763±0.0536	29500±575	5.41±0.06	sdB	0.038±0.004	-11.1368±0.019	0.202±0.021	27.9±3.6	0.38±0.08
148.3206292	15.5617194	731215192	616743220508208896	15.502529±0.002885	0.5389±0.0692	41010±565	5.66±0.07	He-sdOB	0.028±0.001	-11.427±0.007	0.150±0.026	57.2±21.0	0.37±0.16
148.831108	51.616397	293910209	8281203108593591048	12.581236±0.002797	1.7381±0.0464	49140±1028	5.61±0.14	He-sdOB	0.009±0.001	-10.905±0.004	0.153±0.004	124.3±12.6	0.35±0.14
149.209242	14.378333	210808231	615674873163301248	14.282339±0.002835	0.6472±0.0466	45520±592	5.24±0.09	He-sdOB	0.024±0.001	-11.221±0.004	0.202±0.017	158.1±25.6	0.26±0.07
149.884416	36.30718	90914031	795959630108543232	12.795368±0.002795	1.6215±0.0429	27620±592	5.22±0.05	sdB	0.008±0.001	-10.749±0.003	0.238±0.005	29.4±3.1	0.34±0.05
149.966705	3.50916	445703068	3848520258923494656	15.395316±0.002901	0.4647±0.0644	33770±606	5.30±0.06	sdOB	0.021±0.001	-11.344±0.076	0.212±0.038	53.0±20.3	0.33±0.14
150.976151	40.571695	99507015	803736166614876544	13.249913±0.002798	1.0204±0.0365	41260±1020	5.33±0.06	sdO	0.01±0.001	-10.991±0.011	0.222±0.008	127.0±18.9	0.38±0.07
153.7891	0.550186	315411004	3831905500061334912	14.843756±0.002869	0.9408±0.0456	32980±669	5.84±0.09	sdOB	0.031±0.001	-11.226±0.020	0.140±0.007	20.9±2.6	0.50±0.10
155.124196	42.839426	34604022	80569072032579456	15.264394±0.002886	0.3377±0.0595	39670±891	5.93±0.09	sdO	0.014±0.001	-11.380±0.006	0.272±0.065	163.4±94.5	0.49±0.28
158.819075	40.354013	142615080	780253140863277184	11.448022±0.002847	4.73704±0.0542	31660±575	5.93±0.07	sdB	0.012±0.001	-10.539±0.006	0.137±0.002	17.0±1.4	0.57±0.10
159.16221	19.867303	106016182	3987249901607922944	15.574069±0.002864	0.5049±0.0498	33980±722	5.80±0.07	sdOB	0.022±0.001	-11.367±0.034	0.184±0.015	40.5±7.4	0.78±0.16
159.90309	43.102566	228703057	781164326766404736	11.106956±0.002805	4.4105±0.1039	71950±5141	5.67±0.06	sdO	0.011±0.001	-10.678±0.005	0.106±0.002	272.6±68.2	0.19±0.03
160.346854	50.738881	18316005	836644480912524288	14.939624±0.002821	0.4554±0.0467	50230±1472	5.70±0.10	He-sdO	0.014±0.001	-11.373±0.004	0.204±0.024	237.5±69.7	0.75±0.34

Table 1 (continued)

RA	DEC	obs.id	source.id	G	parallax	T_{eff}	$\log g$	spclass	E(B-V)	Angular diameter	Radius	Luminosity	Mass
LAMOST (1)	LAMOST (2)	LAMOST (3)	Gaia EDR3 (4)	Gaia EDR3 (mag) (5)	Gaia EDR3 (mas) (6)	(K) (7)	(cm s^{-2}) (8)	(9)	(10)	log(rad) (11)	R/R_{\odot} (12)	L/L_{\odot} (13)	M/M_{\odot} (14)
160.376837	18.703028	296504043	3986138020473930368	12.967082±0.002875	2.0139±0.0531	34890±767	5.98±0.06	sdOB	0.024±0.001	-10.873±0.005	0.152±0.004	30.5±4.0	0.79±0.14
160.469575	21.675766	712413228	3987913113277693184	13.045824±0.002837	1.9034±0.0486	33410±572	5.75±0.05	sdOB	0.018±0.001	-10.881±0.006	0.151±0.004	25.4±5.5	0.46±0.08
162.3896667	18.7115278	215810196	3983291213071411712	14.87698±0.002831	1.9027±0.0322	29500±659	5.14±0.08	sdB	0.029±0.001	-11.162±0.028	0.298±0.018	59.6±11.4	0.45±0.12
162.5111777	-0.1010237	205211114	380630306686089216	13.419046±0.002916	1.4769±0.0436	38450±572	5.83±0.05	sdOB	0.037±0.001	-10.972±0.009	0.159±0.004	33.8±3.4	0.63±0.10
163.185161	24.930381	403016118	729598330934052480	16.696741±0.002974	0.4234±0.0649	3450±747	5.81±0.15	sdOB	0.081±0.008	-11.560±0.090	0.144±0.026	23.8±2.9	0.49±0.34
163.5772	49.833258	148604206	832980633290384256	13.323629±0.002805	0.7449±0.039	34250±1308	5.21±0.07	sdOB	0.019±0.001	-10.936±0.034	0.345±0.017	144.2±25.2	0.70±0.12
165.233143	10.928443	290014160	3868418219635118080	14.190763±0.002878	1.4055±0.052	32320±572	5.93±0.07	sdOB	0.021±0.001	-11.094±0.014	0.127±0.004	15.9±1.8	0.50±0.11
165.973167	11.001214	290015051	3868458111291375616	15.103493±0.002884	0.6109±0.0442	35750±1192	5.87±0.34	sdOB	0.019±0.001	-11.306±0.005	0.177±0.014	45.8±11.5	0.83±0.98
166.34654	49.583249	503916138	832788184395879424	14.237161±0.002828	0.5381±0.0458	78590±2436	5.36±0.07	sdO	0.017±0.001	-11.336±0.004	0.160±0.013	870.0±160.1	0.21±0.05
166.7103	29.592403	392409050	732692631532422528	15.720041±0.002948	0.5346±0.0515	35630±692	5.86±0.07	sdOB	0.022±0.001	-11.434±0.005	0.150±0.018	33.0±7.9	0.59±0.21
166.8567	47.353497	504003005	7835541848870827264	16.744926±0.002847	0.5037±0.0747	25510±1054	5.63±0.12	sdB	0.032±0.003	-11.483±0.007	0.142±0.018	7.8±4.3	0.32±0.21
167.335037	26.790214	190610055	3998182792399323904	15.468087±0.002835	0.3734±0.0539	40170±1353	5.60±0.13	sdO	0.017±0.001	-11.411±0.092	0.224±0.022	116.6±35.2	0.73±0.13
169.64492	19.829744	297308031	39782070025584425216	13.148385±0.002958	1.3693±0.0424	28090±610	5.42±0.05	sdB	0.017±0.0	-10.823±0.017	0.245±0.007	33.5±4.1	0.57±0.09
170.001536	30.950015	300414223	4023386553845346688	14.49254±0.002992	0.8631±0.0494	33620±664	5.77±0.07	sdOB	0.013±0.001	-11.174±0.007	0.174±0.009	34.3±6.2	0.64±0.13
170.57449	37.448018	439213135	760930907631979904	15.910185±0.002949	0.3087±0.0607	39140±630	5.45±0.08	sdO	0.017±0.001	-11.504±0.007	0.226±0.009	107.9±67.3	0.51±0.36
170.961175	23.612733	309515234	3992841536709886640	14.138851±0.002884	0.8788±0.0403	28080±568	5.38±0.05	sdB	0.015±0.0	-11.017±0.005	0.245±0.011	33.4±3.9	0.52±0.07
171.654513	11.999694	419412143	3917380026471466112	15.696931±0.002884	0.4661±0.0548	29340±635	5.44±0.08	sdB	0.032±0.001	-11.340±0.056	0.215±0.030	30.8±9.4	0.46±0.14
172.51545	1.627016	237307119	3799987433421443712	13.780135±0.002852	1.0469±0.0427	42390±639	5.68±0.09	He-sdOB	0.028±0.001	-11.114±0.008	0.163±0.007	76.8±9.7	0.49±0.10
172.798333	19.611231	393415146	3977575573672822400	15.553078±0.002894	0.5424±0.0519	30440±610	5.74±0.07	sdB	0.021±0.001	-11.336±0.021	0.191±0.017	27.8±4.9	0.74±0.16
173.173392	-6.614569	407007245	3593223417120115712	16.21005±0.00289	0.483±0.0698	49200±1509	5.73±0.09	sdO	0.026±0.001	-11.619±0.031	0.109±0.022	63.5±16.6	0.24±0.13
174.359894	14.170597	571607128	3918117008499710848	13.23756±0.002841	2.0349±0.0488	35700±995	5.83±0.10	He-sdOB	0.028±0.0	-10.941±0.010	0.125±0.003	22.7±3.0	0.38±0.12
174.47542	58.256857	449009063	846070525377462528	16.144583±0.002855	0.5329±0.0473	33830±1245	5.88±0.07	sdOB	0.01±0.0	-11.498±0.009	0.131±0.013	20.2±6.1	0.47±0.15
174.925071	46.730407	140606089	786220877662239488	15.551469±0.002815	0.5227±0.0457	30760±590	5.55±0.07	sdB	0.016±0.001	-11.340±0.009	0.196±0.018	30.5±7.7	0.43±0.14
176.238472	-3.948095	499808226	3600365496761173504	15.859084±0.002908	0.4166±0.0636	28010±659	5.31±0.08	sdB	0.025±0.001	-11.353±0.005	0.235±0.044	31.2±11.9	0.49±0.19
178.016827	39.140844	657402229	403450295999559168	15.340561±0.002818	0.5166±0.0404	58800±2543	5.48±0.11	sdO	0.021±0.0	-11.451±0.064	0.151±0.014	199.0±59.7	0.25±0.10
179.001258	34.123619	399012110	4028265945931548544	14.810241±0.002834	0.5745±0.0523	38180±644	5.42±0.07	sdOB	0.019±0.001	-11.279±0.014	0.201±0.016	77.4±18.7	0.39±0.13
180.921546	25.519844	19002085	4006102059258774272	15.118703±0.002845	0.752±0.064	35060±846	5.63±0.14	sdOB	0.017±0.001	-11.265±0.232	0.150±0.012	30.4±7.4	0.35±0.18
181.601508	57.159922	25714089	1575432697534110336	14.832521±0.002835	0.8492±0.0353	35220±664	5.76±0.07	sdOB	0.013±0.001	-11.262±0.008	0.144±0.006	28.4±3.4	0.43±0.07
182.319787	16.198908	343510162	392257089586104064	13.637659±0.002833	1.2561±0.0438	29840±568	5.67±0.08	sdB	0.033±0.001	-10.929±0.044	0.203±0.008	28.8±2.9	0.71±0.14
182.400326	-3.552102	203010225	3598151393876907904	13.30226±0.002808	2.1343±0.0483	36140±1020	5.88±0.06	sdOB	0.026±0.001	-10.953±0.004	0.115±0.003	20.4±3.0	0.37±0.06
188.963098	42.377703	133410210	1534536701840624768	11.974718±0.002793	3.9874±0.0443	26750±606	5.51±0.08	sdB	0.017±0.001	-10.566±0.006	0.194±0.003	17.3±1.8	0.44±0.10
189.219429	50.253856	22713239	1568451554613870848	14.644768±0.002945	0.6862±0.0459	48380±1463	5.23±0.08	sdO	0.013±0.001	-11.312±0.052	0.157±0.013	118.9±28.5	0.15±0.04
189.347983	25.06663	555614008	3959631234670040704	10.46187±0.002811	7.0625±0.0592	33220±675	6.14±0.10	sdOB	0.019±0.001	-10.359±0.004	0.136±0.001	20.2±1.6	0.94±0.28
189.77099	47.630772	319211089	1543006141129419648	15.546273±0.002806	0.5819±0.0418	29650±573	5.75±0.21	sdB	0.014±0.001	-11.323±0.004	0.184±0.016	23.5±4.8	0.69±0.47
190.159493	51.266733	455403016	156856989552108800	13.57228±0.002812	1.0852±0.032	42190±592	5.72±0.07	He-sdOB	0.01±0.001	-11.075±0.004	0.168±0.006	80.2±7.5	0.55±0.10
190.629575	4.112153	206508081	37041612319296853120	15.467288±0.002821	0.7184±0.0546	34180±568	5.87±0.06	sdOB	0.025±0.0	-11.369±0.017	0.132±0.009	21.6±3.1	0.48±0.09
190.630828	11.733614	437602078	3928420360164984320	15.70003±0.002836	0.2997±0.053	47940±891	5.56±0.23	He-sdOB	0.026±0.002	-11.511±0.005	0.231±0.051	251.1±66.4	0.71±0.29
192.709449	16.176535	100802163	3934486949931442176	14.395102±0.002817	1.1998±0.0393	26540±891	5.53±0.07	sdB	0.02±0.001	-11.045±0.005	0.168±0.006	12.5±2.1	0.35±0.07
193.034742	11.850803	223907015	3927916302803458304	15.23746±0.002812	0.653±0.0492	31600±630	5.63±0.07	sdB	0.025±0.001	-11.284±0.013	0.176±0.012	27.8±4.0	0.48±0.09
193.12335	-3.024892	105710231	3682304199935092096	15.632162±0.002823	0.5984±0.0508	29880±587	5.72±0.06	sdB	0.017±0.0	-11.345±0.006	0.169±0.013	20.4±3.2	0.55±0.16
193.32712	30.108144	144516050	1465043619891174016	15.832666±0.002882	0.567±0.0577	33350±582	5.68±0.08	sdB	0.009±0.0	-11.442±0.009	0.139±0.013	21.5±4.0	0.34±0.10

Table 1 continued on next page

Table 1 (continued)

RA	DEC	obs.id	source.id	G	parallax	T_{eff}	$\log g$	spclass	E(B-V)	Angular diameter	Radius	Luminosity	Mass
LAMOST (1)	LAMOST (2)	LAMOST (3)	Gaia EDR3 (4)	Gaia EDR3 (mag) (5)	Gaia EDR3 (mas) (6)	(K) (7)	(cm s^{-2}) (8)	(9)	(10)	log(rad) (11)	R/R_{\odot} (12)	L/L_{\odot} (13)	M/M_{\odot} (14)
194.114387	27.708522	301803019	1463697233542956672	15.808579±0.002844	0.5983±0.0614	26330±587	5.75±0.08	sdB	0.007±0.0	-11.329±0.008	0.171±0.021	12.8±3.5	0.61±0.21
194.455489	54.42649	415303223	1570270249924113408	13.479468±0.002805	1.6009±0.0293	33130±584	5.89±0.06	sdOB	0.016±0.001	-10.963±0.005	0.148±0.014	23.5±2.2	0.63±0.10
194.834837	27.568081	301804130	1460692714941449728	14.176633±0.002817	1.3746±0.0544	35550±816	5.73±0.09	He-sdOB	0.008±0.0	-11.138±0.005	0.115±0.005	19.0±2.3	0.25±0.07
195.106638	0.7583765	144103116	3689536684343245312	15.695078±0.002895	0.6569±0.0388	37940±923	6.02±0.15	sdOB	0.022±0.001	-11.409±0.109	0.127±0.009	30.4±5.9	0.63±0.25
195.246865	0.953267	327515053	3689564206493682816	16.438677±0.002878	0.4421±0.0617	39660±698	5.70±0.07	He-sdOB	0.022±0.0	-11.602±0.067	0.122±0.023	33.3±12.6	0.27±0.13
196.202858	28.124981	34503131	1461140216174118016	15.449413±0.002807	0.7407±0.0558	34360±1362	5.97±0.09	sdB	0.008±0.0	-11.364±0.008	0.127±0.014	19.9±4.0	0.56±0.13
196.433237	11.978208	214502083	3737057611255721472	16.019308±0.002846	0.4046±0.0587	31840±635	5.63±0.07	sdB	0.028±0.001	-11.441±0.045	0.194±0.036	34.2±9.1	0.56±0.15
196.516153	9.408616	342107122	3734224925705249152	14.436239±0.002799	1.1348±0.0411	29870±617	5.76±0.06	sdB	0.024±0.001	-11.101±0.004	0.153±0.006	16.8±2.1	0.50±0.08
196.564867	48.838822	149710037	1554816510916988544	13.716149±0.002798	1.4305±0.0286	32570±575	5.69±0.06	sdOB	0.008±0.0	-11.007±0.003	0.150±0.003	22.7±4.3	0.40±0.04
196.206285	54.545775	403709179	1564081030251770752	15.8173±0.002841	0.4122±0.0378	38560±761	5.34±0.07	sdB	0.02±0.002	-11.352±0.008	0.236±0.018	33.5±5.4	0.44±0.12
198.942	16.224036	424903052	37446610257454417152	15.774941±0.002811	0.6608±0.0468	28270±584	5.85±0.07	sdOB	0.02±0.001	-11.405±0.005	0.131±0.008	16.6±2.5	0.45±0.11
199.69624	44.595021	739312049	1550490241899314560	14.754681±0.0028	0.5367±0.0357	42850±573	5.73±0.05	He-sdOB	0.016±0.001	-11.315±0.004	0.202±0.016	122.5±24.7	0.80±0.19
199.822539	20.95443	401811071	3940518836361346304	15.134704±0.002801	0.4151±0.0499	51410±1131	5.50±0.07	He-sdOB	0.021±0.001	-11.416±0.004	0.204±0.032	261.3±57.0	0.48±0.12
200.183494	5.983701	36109220	3717383603022961792	14.72766±0.002893	0.5875±0.0461	43660±831	5.70±0.11	He-sdOB	0.031±0.001	-11.300±0.006	0.191±0.017	120.5±24.3	0.67±0.26
200.848058	26.275522	582314065	1449056067988016128	16.165157±0.002851	0.417±0.0637	33770±741	5.89±0.08	sdOB	0.019±0.001	-11.503±0.008	0.166±0.032	32.7±14.0	0.79±0.41
200.896934	36.133203	139410221	1473687671071803520	11.613195±0.002815	2.737±0.0543	36900±741	5.47±0.07	He-sdOB	0.01±0.001	-10.647±0.006	0.183±0.003	56.2±5.2	0.36±0.10
202.973147	15.688212	142716122	3744968013301724544	13.485176±0.002875	1.2606±0.0337	29370±617	5.53±0.07	sdB	0.016±0.0	-10.906±0.006	0.218±0.007	31.8±3.4	0.65±0.28
204.2248833	11.4347944	734713132	3738606616980353664	16.306934±0.002857	0.3949±0.0589	37850±621	5.87±0.08	sdOB	0.026±0.001	-11.554±0.029	0.156±0.029	44.3±19.9	0.65±0.28
204.70065	-2.030368	212806164	3637481302758519040	13.366823±0.004589	1.7079±0.0376	32500±567	5.79±0.05	sdB	0.041±0.004	-10.916±0.059	0.159±0.004	25.2±3.2	0.56±0.07
205.036798	47.864419	143413093	1552221800914196480	13.566182±0.002833	1.2314±0.0305	28480±610	5.40±0.06	sdB	0.021±0.003	-10.903±0.004	0.229±0.006	31.1±3.2	0.48±0.07
205.38117	4.912973	142010081	3714909426982422272	16.196907±0.002902	0.6996±0.0595	59430±4138	6.38±0.12	sdO	0.024±0.001	-11.651±0.020	0.070±0.005	55.3±21.7	0.46±0.18
206.636362	28.289811	448603239	1451833434359977216	14.848846±0.002791	0.6802±0.0383	28040±669	5.33±0.05	sdB	0.013±0.001	-11.156±0.005	0.232±0.013	30.2±3.2	0.41±0.09
206.7520875	-1.1901194	733615158	3727881843124118400	14.938643±0.002834	1.0366±0.0413	23510±566	5.60±0.05	sdB	0.029±0.001	-11.100±0.008	0.172±0.007	8.1±1.3	0.43±0.08
207.971317	-1.496278	41804169	3658738470295900800	15.640486±0.002825	0.4844±0.0475	30420±915	5.70±0.08	sdB	0.05±0.002	-11.322±0.007	0.220±0.025	37.2±7.5	0.88±0.29
208.76946	-2.506063	651513250	3657799934042253952	12.044429±0.002811	3.5942±0.0595	45740±1148	5.65±0.06	sdO	0.043±0.0	-10.761±0.009	0.107±0.002	44.5±5.3	0.19±0.03
208.89461	16.004774	341310209	1243253467230351360	15.889947±0.002864	0.5878±0.0644	37380±686	5.69±0.07	sdOB	0.017±0.0	-11.489±0.006	0.125±0.013	27.4±6.4	0.28±0.07
208.913404	14.910708	341302147	1231024630186706944	15.973404±0.002844	0.5164±0.0512	29210±596	5.48±0.06	sdB	0.018±0.001	-11.387±0.044	0.174±0.016	19.8±4.8	0.33±0.09
209.602612	6.860208	339610163	3720655474749294592	14.305015±0.002812	0.9981±0.0439	28470±680	5.41±0.10	sdB	0.025±0.0	-11.045±0.004	0.200±0.010	23.6±3.5	0.38±0.13
210.821432	28.658128	332003169	1452740084776034944	14.833896±0.002821	0.5108±0.0417	47360±747	5.57±0.07	He-sdOB	0.014±0.0	-11.345±0.004	0.197±0.015	177.7±29.8	0.53±0.14
211.43857	1.7386288	732404097	3661331668469980416	15.775452±0.003031	0.3055±0.045	27770±572	5.27±0.06	sdB	0.03±0.001	-11.324±0.011	0.346±0.069	64.2±29.2	0.81±0.35
211.499225	31.409769	537808228	1454323415879594368	13.463078±0.002825	1.7055±0.0357	30540±606	5.73±0.07	sdB	0.011±0.0	-10.923±0.005	0.151±0.006	18.1±1.7	0.46±0.08
212.567679	32.412925	230113142	147844229724415104	14.878578±0.002825	0.9646±0.0375	31620±659	6.03±0.08	sdB	0.012±0.001	-11.222±0.005	0.141±0.006	17.9±3.3	0.76±0.16
212.607982	-1.504604	449815203	3647329074356945152	13.707858±0.002847	0.8539±0.0362	36690±754	5.59±0.05	sdOB	0.056±0.002	-11.020±0.010	0.246±0.009	98.9±9.9	0.85±0.14
212.732694	9.548705	723502076	3723006814724972416	14.029369±0.002899	1.2371±0.0429	36840±606	5.83±0.05	sdOB	0.02±0.001	-11.112±0.031	0.139±0.005	31.9±2.9	0.47±0.06
213.598658	29.684781	233014059	1260997037986811648	16.637234±0.002869	0.394±0.0658	24980±639	5.68±0.07	sdB	0.016±0.0	-11.467±0.008	0.186±0.039	12.1±6.1	0.61±0.32
213.764081	41.8243	575416138	1492192692285509376	14.776727±0.002821	0.9046±0.0338	30910±610	5.64±0.08	sdB	0.009±0.0	-11.191±0.006	0.161±0.018	21.2±2.1	0.41±0.16
213.954395	11.2038595	723504163	1225417739360402048	16.014019±0.002911	0.3337±0.0628	41500±573	5.50±0.12	He-sdOB	0.019±0.0	-11.553±0.011	0.179±0.047	85.2±52.4	0.38±0.27
214.587163	-3.381686	449706090	364592008861401216	16.478344±0.002939	0.4509±0.0743	29790±635	5.79±0.06	sdB	0.049±0.001	-11.489±0.013	0.158±0.034	17.7±8.7	0.57±0.29
216.248249	3.328705	236906092	36684919109893566464	16.443863±0.002933	0.4806±0.0667	35200±654	5.82±0.32	sdOB	0.029±0.001	-11.574±0.008	0.119±0.012	20.0±4.6	0.36±0.18
216.283123	20.878427	316812154	1240306604269576704	14.9679±0.002832	0.8432±0.0415	35660±722	5.72±0.09	sdOB	0.037±0.001	-11.274±0.050	0.143±0.007	29.4±4.4	0.39±0.12
216.49655	28.787578	233008016	1283953333241515520	16.714096±0.002831	0.3259±0.0515	34250±599	5.64±0.06	sdB	0.014±0.0	-11.595±0.065	0.175±0.032	37.6±17.4	0.48±0.25

Table 1 continued on next page

Table 1 (continued)

RA	DEC	obs.id	source.id	G	parallax	T_{eff}	$\log g$	spclass	E(B-V)	Angular diameter	Radius	Luminosity	Mass
LAMOST (1)	LAMOST (2)	LAMOST (3)	Gaia EDR3 (4)	Gaia EDR3 (mag) (5)	Gaia EDR3 (mas) (6)	(K) (7)	(cm s^{-2}) (8)	(9)	(10)	log(rad) (11)	R/R_{\odot} (12)	L/L_{\odot} (13)	M/M_{\odot} (14)
217.123294	21.10059	307805237	1240449403342559360	13.206256±0.002822	2.247±0.0462	32550±570	5.86±0.06	sdB	0.03±0.001	-10.893±0.023	0.125±0.003	16.0±1.2	0.42±0.07
217.365692	19.359703	316813056	123936476948058496	14.071779±0.002857	0.7202±0.0408	50580±1565	5.55±0.17	He-sdOB	0.026±0.0	-11.193±0.005	0.195±0.013	222.3±46.6	0.52±0.25
218.77645	28.797477	566705209	1281101268798929152	16.081741±0.002794	0.4934±0.0466	36500±649	5.85±0.07	sdOB	0.017±0.001	-11.512±0.048	0.137±0.016	30.3±5.5	0.49±0.17
218.828893	-15.670621	132712144	1234322477875249664	13.842321±0.00414	1.6037±0.0342	26210±602	5.47±0.07	sdB	0.019±0.001	-10.928±0.005	0.163±0.005	11.2±1.5	0.29±0.06
220.220106	-3.174965	418220302	3648191164488514688	13.794926±0.002303	1.2947±0.0466	29490±621	5.45±0.06	sdB	0.08±0.004	-10.927±0.006	0.202±0.006	27.4±3.1	0.42±0.07
220.322231	1.624409	527203236	3655309299687364992	14.240586±0.002849	1.1558±0.0402	29110±639	5.75±0.06	sdB	0.034±0.001	-11.035±0.016	0.176±0.006	20.0±2.2	0.62±0.08
221.04239	34.353706	574013227	1292915830478091008	16.006956±0.002818	0.3602±0.0472	46830±644	5.72±0.18	He-sdOB	0.01±0.001	-11.579±0.006	0.157±0.016	107.9±22.8	0.47±0.18
221.784479	7.397089	140208168	1171708967165771392	14.617061±0.002913	0.598±0.0498	49380±1054	5.43±0.16	He-sdOB	0.023±0.001	-11.300±0.006	0.184±0.019	181.9±40.4	0.33±0.18
223.344967	39.496492	242506213	1296418427846820608	16.142±0.002865	0.5978±0.0459	30110±734	5.81±0.12	sdB	0.011±0.0	-11.454±0.005	0.129±0.009	12.3±1.9	0.40±0.15
223.61111	47.334557	344015107	1590388529573233536	16.088852±0.002863	0.4423±0.0432	30350±566	5.74±0.06	sdB	0.017±0.0	-11.441±0.008	0.184±0.019	25.6±4.7	0.56±0.20
223.665896	19.616899	334115038	1237226700401153792	12.431075±0.002891	2.9859±0.0466	31000±582	5.88±0.05	sdB	0.023±0.001	-11.715±0.007	0.143±0.003	16.8±1.4	0.67±0.13
224.526717	8.858398	651102213	1161864283648012160	14.624252±0.002901	1.2006±0.0456	22500±587	5.48±0.06	sdB	0.027±0.001	-11.021±0.004	0.178±0.006	7.2±1.0	0.34±0.06
224.8688067	19.0638675	657013168	118933362275187200	14.228025±0.002862	1.3201±0.036	36420±781	6.00±0.06	sdOB	0.036±0.001	-11.132±0.006	0.125±0.003	24.9±2.5	0.57±0.10
225.102211	42.095753	580111192	1585277243613047936	13.861313±0.00282	1.1271±0.0304	31000±579	5.59±0.06	sdB	0.014±0.0	-11.007±0.004	0.192±0.005	30.5±3.4	0.52±0.09
226.152825	12.803728	442407239	1181028908759001472	15.431147±0.002915	0.371±0.0432	46180±728	5.48±0.10	He-sdOB	0.031±0.0	-11.451±0.009	0.212±0.033	184.0±62.7	0.52±0.24
227.154254	10.053918	651108142	1167834597427267456	15.085231±0.002896	0.5859±0.0741	35880±635	5.79±0.12	sdOB	0.032±0.001	-11.307±0.006	0.187±0.029	52.4±11.0	0.81±0.24
227.805583	26.289058	462202202	1270423258548105728	15.842945±0.002806	0.4859±0.0412	30470±596	5.46±0.10	sdB	0.032±0.001	-11.362±0.069	0.194±0.022	29.1±4.5	0.41±0.11
230.1914	29.80715	219416182	12756262415380252544	15.664035±0.002816	0.6702±0.0505	37890±741	6.03±0.09	sdOB	0.02±0.001	-11.451±0.004	0.116±0.011	25.3±4.8	0.53±0.17
231.759504	42.068681	573415155	1390836583700955264	16.297833±0.002928	0.3318±0.0542	30860±584	5.73±0.07	sdB	0.018±0.001	-11.486±0.019	0.218±0.029	38.5±9.7	0.99±0.12
231.78	10.270154	565710176	1165815825359631232	16.112337±0.002853	0.3807±0.0444	33230±923	5.15±0.07	sdB	0.034±0.001	-11.425±0.092	0.218±0.022	51.2±10.2	0.24±0.09
232.084522	10.50891	567310064	1165848673269627520	15.921133±0.002873	0.5213±0.0668	35120±649	5.75±0.08	sdOB	0.038±0.001	-11.465±0.016	0.144±0.026	28.4±10.8	0.44±0.12
232.217458	9.528992	567302092	116553678992411616	16.424826±0.002913	0.3585±0.0614	32720±590	5.88±0.07	sdOB	0.03±0.001	-11.536±0.009	0.175±0.024	31.4±7.9	0.85±0.33
232.708505	6.015569	566509196	4429114659552190080	14.691596±0.002846	1.2313±0.0412	33840±570	6.00±0.06	sdOB	0.04±0.001	-11.196±0.006	0.114±0.004	15.1±1.4	0.47±0.08
232.762545	33.638114	333013143	1373881186687373696	14.761776±0.002816	0.891±0.0328	31680±596	5.92±0.06	sdB	0.026±0.001	-11.188±0.004	0.164±0.006	24.2±3.1	0.81±0.16
232.79329	10.250305	243312195	1165963744033018496	13.546925±0.003113	1.4799±0.0317	26800±1037	5.51±0.10	sdB	0.03±0.001	-10.877±0.005	0.197±0.006	18.0±3.1	0.45±0.12
233.317108	44.587383	582404042	13945816233383963264	15.524522±0.002838	0.7233±0.0361	30400±584	5.80±0.06	sdB	0.016±0.002	-11.326±0.017	0.144±0.006	16.0±1.7	0.49±0.10
233.374829	52.113533	53103086	1595357428778737344	13.973778±0.002832	1.6017±0.0259	31890±626	6.05±0.08	sdB	0.011±0.001	-11.048±0.004	0.123±0.002	14.1±1.2	0.61±0.12
233.456025	37.991129	331509102	1375814952762454272	12.941533±0.004614	1.9294±0.0345	29300±577	5.55±0.05	sdB	0.011±0.001	-10.793±0.004	0.186±0.003	23.1±2.6	0.46±0.06
233.796725	23.788525	328505074	1220934996098999552	15.567246±0.002815	0.5193±0.0429	27150±621	5.37±0.06	sdB	0.041±0.001	-11.271±0.016	0.236±0.018	26.8±4.6	0.47±0.08
233.815317	34.790072	322207235	1374058963973357696	15.0359±0.002805	0.6409±0.0354	38230±704	5.57±0.07	sdB	0.017±0.0	-11.323±0.006	0.108±0.012	53.6±6.1	0.38±0.09
234.67853	9.5784135	565707040	1165071009310870912	15.708179±0.002924	0.4495±0.0405	35840±575	5.62±0.06	sdOB	0.033±0.001	-11.359±0.109	0.204±0.016	62.2±13.7	0.62±0.18
235.097774	26.808252	328611040	12233920926079402112	13.79695±0.002791	1.2256±0.0297	26220±577	5.41±0.07	sdB	0.04±0.001	-10.905±0.004	0.228±0.005	22.2±2.4	0.49±0.09
235.162647	39.930281	152406202	1377891689708857856	13.199988±0.002839	2.4232±0.0305	33520±861	6.25±0.14	sdB	0.017±0.001	-10.911±0.005	0.111±0.002	13.9±1.3	0.79±0.20
236.678871	0.757753	457502165	4422600328035803264	15.090169±0.002887	0.7146±0.0416	52670±1528	5.43±0.13	sdO	0.084±0.001	-11.375±0.010	0.130±0.008	118.6±20.9	0.16±0.04
237.67498	29.756532	339709096	1320813464131916416	16.389122±0.00283	0.3262±0.0458	30770±568	5.53±0.07	sdB	0.024±0.0	-11.503±0.053	0.221±0.037	39.3±14.1	0.60±0.25
237.701252	16.440384	571812247	1196375273586921472	14.829869±0.002838	0.6879±0.0427	32050±568	5.68±0.06	sdOB	0.047±0.002	-11.200±0.009	0.205±0.012	39.5±5.1	0.73±0.13
239.140379	22.046203	1206214356465503616	13.79815±0.002811	0.6649±0.0352	78490±9596	5.20±0.08	He-sdO	0.05±0.001	0.05±0.001	-11.189±0.004	0.216±0.010	1601.5±1120.0	0.28±0.06
239.374454	48.839656	437201058	1399993557054575232	16.492474±0.002881	0.2963±0.0505	43920±831	6.01±0.14	He-sdOB	0.016±0.001	-11.665±0.011	0.162±0.036	86.4±3.7	1.00±0.32
239.4949003	14.0390339	740903219	1191689807863866112	15.347903±0.002837	0.916±0.0399	30520±644	5.85±0.06	sdB	0.036±0.001	-11.283±0.013	0.128±0.005	12.9±1.4	0.43±0.07
240.300504	53.197761	149514028	1404827731724827776	14.23653±0.002853	1.3414±0.026	30940±590	5.79±0.06	sdB	0.013±0.001	-11.083±0.004	0.136±0.003	15.3±1.2	0.42±0.08
240.380311	4.674167	133105185	4425487989169416320	14.459783±0.002875	1.4155±0.0431	38100±669	5.74±0.07	He-sdOB	0.058±0.002	-11.183±0.011	0.103±0.003	20.0±1.6	0.21±0.04

Table 1 continued on next page

Table 1 (continued)

RA LAMOST (1)	DEC LAMOST (2)	obs.id LAMOST (3)	source.id Gaia EDR3 (4)	G Gaia EDR3 (mag) (5)	parallax Gaia EDR3 (mas) (6)	T_{eff} (K) (7)	$\log g$ (cm s^{-2}) (8)	spclass (9)	E(B-V) (10)	Angular diameter log(rad) (11)	Radius R/R_{\odot} (12)	Luminosity L/L_{\odot} (13)	Mass M/M_{\odot} (14)
242.015365	7.074661	133011059	4450489165598124800	12.805161±0.003703	1.3807±0.0597	32480±626	5.34±0.06	sdB	0.047±0.002	-10.804±0.006	0.250±0.012	62.2±8.3	0.50±0.09
242.385059	22.630508	461109174	1206447693448896128	16.32137±0.002843	0.32±0.0565	44740±774	5.64±0.12	He-sdOB	0.073±0.003	-11.595±0.043	0.175±0.046	110.6±99.2	0.49±0.38
242.478874	17.249217	347906246	1198927755470384128	12.210127±0.002793	1.6149±0.0496	29170±569	5.12±0.05	He-sdOB	0.038±0.001	-10.640±0.003	0.314±0.011	64.3±6.0	0.47±0.08
242.838926	52.768252	432203009	1427969118595251072	12.750125±0.002845	2.3455±0.0361	30870±596	5.66±0.06	sdB	0.022±0.001	-10.777±0.036	0.157±0.002	20.0±2.0	0.41±0.07
242.95559	19.397395	558412106	1201659389029469184	15.868877±0.002845	0.5588±0.0471	33090±590	5.81±0.07	sdOB	0.044±0.002	-11.424±0.008	0.148±0.013	23.6±5.4	0.51±0.14
243.002746	51.82875	149505207	1427678435208512384	13.654894±0.002801	0.951±0.037	34620±680	5.08±0.08	sdOB	0.023±0.001	-10.997±0.059	0.234±0.009	70.7±7.3	0.24±0.04
243.18797	4.2115442	744007193	4437254653372798848	16.007946±0.002865	0.3919±0.0539	45700±664	5.65±0.07	He-sdOB	0.057±0.001	-11.552±0.007	0.155±0.029	94.5±39.7	0.39±0.19
243.365233	8.898758	233106152	4452964853466754048	14.609142±0.002835	1.0963±0.0381	31400±582	5.91±0.07	sdB	0.034±0.001	-11.151±0.006	0.145±0.005	18.4±2.2	0.63±0.13
243.572692	3.997775	568307134	4437211291383115392	15.566049±0.002822	0.3733±0.0451	46690±1020	5.60±0.07	He-sdOB	0.053±0.001	-11.462±0.006	0.206±0.021	181.1±98.5	0.61±0.14
243.696	42.459869	241910003	1381954385173920640	14.368959±0.002869	1.0083±0.0305	35200±1518	5.83±0.10	sdOB	0.013±0.0	-11.152±0.005	0.153±0.006	32.3±5.3	0.57±0.16
244.596204	14.270251	337915062	44632625890008114944	13.422815±0.002786	1.8174±0.0331	36830±568	6.07±0.05	sdOB	0.047±0.001	-10.973±0.003	0.130±0.003	27.6±1.7	0.70±0.05
244.84043	29.918343	342209165	1318236621192489216	16.842691±0.002861	0.3585±0.0569	33060±635	5.93±0.14	sdB	0.036±0.001	-11.622±0.007	0.147±0.031	23.5±0.6	0.71±0.09
244.84679	30.833913	220412139	1319053146015474688	15.618161±0.00282	0.7394±0.038	36610±971	5.98±0.14	sdOB	0.024±0.0	-11.423±0.006	0.113±0.007	20.8±2.8	0.46±0.19
245.7361	47.514196	743008201	1410860511508492288	16.21871±0.003708	0.5469±0.0445	28100±606	5.66±0.07	sdB	0.007±0.0	-11.436±0.017	0.148±0.014	12.1±2.9	0.36±0.17
245.874442	24.761389	238215199	1302449042967968640	15.683034±0.002805	0.3048±0.042	53080±931	5.68±0.09	He-sdO	0.042±0.001	-11.516±0.005	0.223±0.036	355.6±132.6	0.86±0.37
246.132846	40.986953	241901157	1380974582874497280	14.443345±0.002812	0.7331±0.0328	28950±577	5.43±0.05	sdB	0.007±0.001	-11.084±0.031	0.246±0.010	38.1±4.4	0.58±0.08
246.725946	8.426436	236512210	4440350981196959104	14.897121±0.002828	0.657±0.0436	41520±566	5.64±0.06	He-sdOB	0.057±0.001	-11.302±0.024	0.171±0.014	78.5±11.0	0.47±0.11
246.818754	40.457908	576301124	133289630646572160	12.538268±0.002798	2.3654±0.034	23710±562	5.49±0.05	sdOB	0.007±0.001	-10.638±0.006	0.214±0.003	13.0±1.5	0.51±0.08
247.093844	27.488591	225003186	1305126525580012672	13.620311±0.002804	1.1887±0.0295	27750±598	5.41±0.06	sdB	0.044±0.006	-10.890±0.005	0.247±0.006	32.3±1.4	0.58±0.08
247.4703492	11.0840364	663715062	4458994472154612480	14.332891±0.002803	1.2518±0.0731	27900±587	5.42±0.05	sdB	0.052±0.001	-11.026±0.007	0.105±0.012	15.2±2.0	0.26±0.05
248.005651	7.994445	140315205	4440145853560129408	12.839467±0.002782	1.167±0.0392	38450±1012	5.42±0.05	sdO	0.066±0.001	-10.849±0.006	0.266±0.011	140.1±19.6	0.69±0.10
248.05109	17.888424	146615140	4467169787783133312	15.982681±0.003004	0.5759±0.0575	36470±1281	5.62±0.25	sdB	0.049±0.002	-11.476±0.004	0.131±0.017	27.3±0.5	0.27±0.05
248.647179	26.350464	566608204	1304379201270414592	16.940329±0.002851	0.3061±0.0532	51420±1201	5.70±0.12	sdO	0.048±0.002	-11.752±0.043	0.126±0.018	99.7±27.2	0.30±0.21
249.26495	5.984855	571908139	4435849168273656704	13.822571±0.002833	2.0484±0.0859	30750±579	5.50±0.06	sdB	0.068±0.001	-10.962±0.004	0.120±0.006	11.5±1.3	0.17±0.03
250.878644	51.415874	585102152	1413338325384928128	16.15201±0.002857	0.3433±0.0338	35940±788	5.09±0.06	sdOB	0.015±0.002	-11.489±0.082	0.205±0.025	63.4±17.0	0.19±0.06
251.154843	-0.001554	340308108	4382904797178453504	13.641729±0.002829	1.4584±0.0249	26430±635	5.51±0.06	sdB	0.134±0.002	-10.813±0.004	0.233±0.003	23.9±2.3	0.65±0.09
251.538521	40.290433	152701066	1355775219474985856	14.079659±0.002847	1.2857±0.028	29810±579	5.69±0.05	sdB	0.012±0.0	-11.034±0.021	0.158±0.004	17.7±1.5	0.45±0.07
252.2449	24.967189	567901136	1300121926607765760	16.04618±0.002816	0.9095±0.0377	23390±675	5.72±0.07	sdB	0.07±0.005	-11.283±0.060	0.127±0.005	4.3±0.7	0.31±0.06
252.499386	53.525487	148415067	142598175870116864	14.009392±0.002826	1.1785±0.0248	31000±931	5.60±0.13	sdB	0.053±0.005	-11.004±0.005	0.183±0.003	27.8±3.2	0.50±0.14
253.7016	15.882959	546709115	4557895027682278784	15.513562±0.002811	0.5183±0.0393	43060±669	5.59±0.12	He-sdOB	0.08±0.001	-11.419±0.009	0.160±0.013	78.1±14.1	0.36±0.16
253.928415	13.030146	144307163	4449162845336419840	14.356711±0.00289	0.9544±0.0347	26230±788	5.34±0.08	sdB	0.06±0.002	-11.003±0.007	0.225±0.009	21.6±3.5	0.41±0.09
254.756648	29.042889	739510211	1309437641952913920	16.08472±0.002828	0.3735±0.0387	27720±899	5.61±0.13	sdB	0.034±0.001	-11.392±0.003	0.24±0.002	32.2±1.7	0.89±0.37
254.990298	28.848331	739510216	1308678016856993920	14.372261±0.002812	0.8986±0.0285	37520±868	5.73±0.05	sdO	0.039±0.002	-11.165±0.003	0.166±0.005	49.0±4.8	0.54±0.08
255.65702	24.589606	143802076	4572469019942466304	15.914248±0.002815	0.5792±0.0377	27590±891	5.46±0.08	sdB	0.05±0.003	-11.342±0.008	0.178±0.013	16.3±3.8	0.33±0.10
255.76656	15.138432	745914113	4545907052398514432	17.095757±0.002878	0.3615±0.0688	27460±692	5.34±0.07	sdB	0.094±0.003	-11.549±0.011	0.171±0.049	15.6±10.0	0.23±0.15
255.98617	34.251398	565812178	1337803736279119616	16.697882±0.002871	0.2855±0.0453	28360±592	5.34±0.06	sdB	0.018±0.001	-11.516±0.033	0.239±0.032	33.1±8.5	0.46±0.27
256.02866	28.90447	346705170	1308731137012654464	17.012312±0.002868	0.4982±0.0554	32720±649	5.92±0.09	sdOB	0.057±0.003	-11.628±0.013	0.104±0.015	11.1±2.0	0.63±0.14
256.313389	35.471831	576815103	1338485777087459072	15.565695±0.002826	0.4617±0.0326	43090±613	5.79±0.06	He-sdOB	0.002±0.001	-11.473±0.059	0.166±0.014	85.7±15.5	0.31±0.16
256.39427	24.890812	143802233	4572125628717747200	16.825285±0.002847	0.3747±0.0567	34410±838	5.80±0.09	sdB	0.043±0.002	-11.627±0.008	0.144±0.021	25.9±7.1	0.48±0.15
257.3859	21.370697	575513248	4567834303554972288	15.590922±0.002803	0.6506±0.0397	35690±630	5.80±0.07	sdOB	0.05±0.001	-11.391±0.048	0.139±0.010	27.7±3.0	0.45±0.10
257.555047	53.446121	148413001	1419133610657016064	12.587522±0.002855	2.8516±0.0345	24010±716	5.54±0.12	sdB	0.013±0.001	-10.647±0.008	0.175±0.002	9.2±1.1	0.39±0.09

Table 1 continued on next page

Table 1 (continued)

RA	DEC	obs.id	source.id	G	parallax	T_{eff}	$\log g$	spclass	E(B-V)	Angular diameter	Radius	Luminosity	Mass
LAMOST (1)	LAMOST (2)	LAMOST (3)	Gaia EDR3 (4)	Gaia EDR3 (mag) (5)	Gaia EDR3 (mas) (6)	(K) (7)	(cm s^{-2}) (8)	(9)	(10)	log(rad) (11)	R/R_{\odot} (12)	L/L_{\odot} (13)	M/M_{\odot} (14)
258.078166	48.976605	148506234	1414187320160273024	12.828451±0.002787	2.1667±0.0317	29870±590	5.85±0.07	sdB	0.008±0.0	-10.785±0.004	0.169±0.003	20.4±1.9	0.74±0.15
258.2631	16.178565	745911237	4546882216133354752	16.245491±0.002853	0.5274±0.0486	35550±704	5.82±0.06	sdOB	0.067±0.001	-11.509±0.006	0.130±0.013	24.1±3.9	0.41±0.10
258.269431	24.838763	564407046	457192212486265216	17.404416±0.002866	0.4103±0.0643	27400±686	5.44±0.05	sdB	0.049±0.002	-11.570±0.009	0.143±0.030	10.4±3.0	0.21±0.11
259.32832	42.435913	141008222	1360139937040515072	12.453231±0.002792	2.395±0.0387	66410±10165	5.67±0.09	sdO	0.019±0.001	-10.913±0.010	0.113±0.021	223.6±186.1	0.22±0.05
259.37476	32.12192	573808096	1333535634003198848	17.206957±0.002941	0.3032±0.0585	32540±698	5.76±0.09	sdB	0.038±0.001	-11.675±0.052	0.151±0.037	22.8±13.9	0.50±0.29
259.824376	47.372495	745114017	1365071418489267584	15.77518±0.002865	0.6549±0.0385	38620±774	5.87±0.08	sdOB	0.03±0.002	-11.466±0.007	0.114±0.006	26.0±3.1	0.36±0.07
260.35745	9.033239	241603163	4491274930955326080	15.604965±0.002823	0.5821±0.0363	26640±747	5.55±0.06	sdB	0.085±0.004	-11.243±0.008	0.216±0.016	21.2±3.3	0.60±0.13
261.050108	28.591214	227215215	4598511330803479936	13.325417±0.002806	2.0895±0.0272	36350±602	5.89±0.06	sdOB	0.032±0.001	-10.966±0.035	0.116±0.001	21.0±1.4	0.37±0.05
261.989091	25.143254	584512022	4570629777508086400	12.962732±0.002786	1.714±0.0305	27540±686	5.47±0.09	sdB	0.05±0.004	-10.739±0.009	0.237±0.005	28.9±3.0	0.61±0.16
262.26331	17.326944	742209223	4550175420961718528	16.28401±0.002844	0.3041±0.0456	37750±868	5.17±0.10	sdB	0.07±0.003	-11.544±0.007	0.211±0.036	82.2±32.2	0.25±0.12
264.126193	7.600641	341003194	4487346891305390592	13.678309±0.002833	1.9843±0.0273	27890±599	5.37±0.06	sdB	0.149±0.005	-10.839±0.007	0.228±0.005	28.3±2.9	0.45±0.07
264.360098	22.149371	446111200	4557081835745623808	11.801611±0.00288	2.3476±0.0464	41170±816	5.28±0.05	sdO	0.067±0.001	-10.669±0.013	0.169±0.024	105.7±10.9	0.28±0.04
264.776732	11.296711	242308023	4492802221326659456	13.281932±0.002835	1.738±0.0328	28430±587	5.52±0.06	sdB	0.129±0.003	-10.786±0.018	0.210±0.004	25.7±2.1	0.53±0.07
265.091562	48.899451	580907209	1363886900869046656	13.176237±0.002878	1.5615±0.0303	27550±635	5.41±0.06	sdB	0.018±0.001	-10.811±0.003	0.221±0.004	25.1±3.0	0.46±0.07
265.676651	44.503737	568416221	1350113181268869632	16.002327±0.002882	0.4042±0.0464	37500±741	5.56±0.16	sdOB	0.026±0.002	-11.506±0.006	0.169±0.024	51.7±16.8	0.38±0.22
265.82931	21.543762	457610044	4556606305156496768	13.992819±0.002779	1.0877±0.0234	37590±846	5.56±0.10	sdOB	0.098±0.004	-11.049±0.005	0.183±0.004	59.7±5.4	0.44±0.13
266.726507	43.76783	568415057	1349088676950060672	14.360828±0.002831	1.0659±0.0262	32760±617	5.67±0.05	sdOB	0.025±0.001	-11.137±0.003	0.148±0.004	5.4±2.5	0.34±0.10
267.483551	0.110035	459005109	4371689194462064768	14.337096±0.002786	1.984±0.0235	37600±573	5.89±0.07	sdB	0.037±0.006	-10.922±0.005	0.135±0.004	18.4±1.6	0.52±0.08
268.270067	24.596209	457611042	4581048921494269056	14.598722±0.002812	0.6139±0.031	37320±781	5.40±0.07	sdB	0.064±0.002	-11.197±0.005	0.227±0.013	89.7±11.4	0.47±0.16
270.030251	31.577103	663811042	4603104815057642752	15.210573±0.00283	0.675±0.0337	26970±716	5.52±0.07	sdB	0.038±0.001	-11.199±0.005	0.207±0.009	20.5±3.0	0.52±0.13
271.34282	15.200315	746410046	4498502433203434368	16.894659±0.002897	0.5589±0.0673	28260±573	5.30±0.06	sdB	0.087±0.002	-11.517±0.022	0.121±0.012	8.3±2.8	0.11±0.02
271.95262	14.507648	746402150	4498196768968750336	15.8908±0.002843	0.52±0.0437	28730±635	5.39±0.06	sdB	0.14±0.007	-11.298±0.016	0.215±0.020	28.3±5.2	0.41±0.11
272.388874	22.516659	234607117	4577984720030433536	12.91816±0.002772	2.2299±0.0273	27480±567	5.53±0.05	sdB	0.093±0.003	-10.713±0.003	0.194±0.003	19.4±2.2	0.47±0.07
273.615979	41.90375	239111121	2113506200378734848	16.126574±0.002878	0.4902±0.0359	27760±596	5.36±0.06	sdB	0.049±0.001	-11.387±0.009	0.182±0.011	17.8±3.4	0.28±0.06
272.76169	17.633307	746415156	4526224282435916544	17.07194±0.002954	0.3866±0.0618	44410±1380	5.97±0.19	He-sdOB	0.11±0.005	-11.731±0.010	0.106±0.022	39.9±20.6	0.39±0.33
273.0417	18.131682	746411012	4526347084141410432	15.466732±0.002809	0.5603±0.0329	30170±567	5.41±0.05	sdB	0.105±0.002	-11.236±0.053	0.226±0.012	37.8±4.2	0.48±0.07
274.13538	34.930314	743615206	4605575383775753856	16.002438±0.002873	0.4889±0.0441	47780±1810	5.48±0.06	sdO	0.042±0.0	-11.554±0.010	0.127±0.013	75.9±16.8	0.18±0.04
274.83431	18.178403	746412176	4523666131196149632	16.41353±0.002903	0.4004±0.0525	27630±606	5.14±0.06	sdB	0.193±0.008	-11.351±0.009	0.191±0.031	18.8±3.9	0.19±0.07
274.88444	6.0783654	742405150	4476966603891088640	17.09612±0.002944	0.3676±0.0732	36240±809	5.36±0.17	sdB	0.211±0.01	-11.595±0.010	0.154±0.026	36.2±11.5	0.20±0.10
274.95133	33.369344	743604247	4592825172063276288	16.418398±0.00285	0.2764±0.0387	28380±592	5.44±0.05	sdB	0.054±0.001	-11.450±0.006	0.283±0.054	46.7±10.9	0.31±0.09
279.219563	57.462023	346803047	2154234138295602672	16.440025±0.002849	0.5968±0.0434	28290±639	5.71±0.09	sdB	0.043±0.001	-11.466±0.010	0.127±0.010	9.3±1.9	0.81±0.20
279.443598	59.26635	346815163	2154810316748450432	14.578444±0.002845	0.7916±0.0319	39210±569	5.72±0.08	He-sdOB	0.053±0.003	-11.232±0.052	0.163±0.007	56.3±6.2	0.51±0.12
285.754739	34.758065	574208088	2092525388221505792	15.676477±0.002826	0.5026±0.0355	28440±596	5.45±0.05	sdB	0.08±0.002	-11.290±0.007	0.233±0.015	32.1±4.6	0.57±0.13
285.90424	38.603512	576405016	2100027626635533056	14.64371±0.002808	0.8216±0.0306	29050±577	5.39±0.06	sdB	0.093±0.003	-11.084±0.004	0.221±0.010	31.1±3.0	0.45±0.08
286.918867	42.306115	161401152	2105469320138052864	10.588934±0.00279	4.1507±0.0319	30560±621	5.10±0.07	sdB	0.058±0.002	-10.313±0.038	0.260±0.022	52.6±4.8	0.31±0.06
287.27975	37.937321	576407250	2099149567821051904	15.243486±0.00283	0.7881±0.027	24320±572	5.42±0.05	sdB	0.145±0.013	-11.104±0.029	0.218±0.002	14.8±1.8	0.45±0.04
288.15187	43.674379	362008075	2103044549103238912	12.443379±0.002782	2.566±0.0361	27850±613	5.57±0.07	sdB	0.063±0.006	-10.647±0.015	0.196±0.003	20.8±1.9	0.51±0.10
288.82889	42.93705	664703151	2102745688098547840	14.483809±0.002834	0.6843±0.0306	38420±1113	5.54±0.16	sdO	0.087±0.003	-11.171±0.018	0.220±0.011	95.4±16.1	0.62±0.33
291.52478	47.275349	354204250	2129130844728397568	14.842774±0.00284	0.4276±0.0316	62190±1574	5.65±0.08	He-sdO	0.072±0.002	-11.356±0.005	0.230±0.009	715.2±114.7	0.90±0.19
291.539417	37.335611	52401101	2051770507972278016	13.594062±0.002922	1.7302±0.0237	30670±587	5.82±0.07	sdB	0.247±0.016	-10.819±0.024	0.193±0.003	29.4±2.1	0.90±0.18
291.64212	49.50824	353808152	2129777323205768448	14.787799±0.002827	0.7855±0.0275	27340±1272	5.56±0.14	sdB	0.06±0.001	-11.111±0.015	0.222±0.008	24.8±3.5	0.64±0.30

Table 1 continued on next page

Table 1 (continued)

RA	DEC	obs.id	source.id	G	parallax	T_{eff}	$\log g$	spclass	E(B-V)	Angular diameter	Radius	Luminosity	Mass
LAMOST (1)	LAMOST (2)	LAMOST (3)	Gaia EDR3 (4)	Gaia EDR3 (mag) (5)	Gaia EDR3 (mas) (6)	(K) (7)	(cm s^{-2}) (8)	(9)	(10)	log(rad) (11)	R/R_{\odot} (12)	L/L_{\odot} (13)	M/M_{\odot} (14)
291.81268	38.45518	664011152	2052684550030830464	15.594818±0.00283	0.4372±0.0341	39890±567	5.38±0.16	He-sdOB	0.11±0.004	-11.396±0.047	0.202±0.018	92.1±20.3	0.34±0.19
292.78702	43.416039	664613110	2125895669204184832	13.572659±0.002818	0.6387±0.0263	66880±11164	5.15±0.06	sdO	0.109±0.002	-11.076±0.010	0.293±0.013	1481.7±739.9	0.44±0.10
35.000895	35.000895	664007120	2048109069842534912	15.320847±0.002817	0.7685±0.0297	34560±987	5.71±0.08	sdOB	0.148±0.006	-11.261±0.011	0.158±0.007	32.4±4.3	0.46±0.11
293.86659	35.732989	664008145	2048434490916786176	15.756708±0.002817	0.8145±0.0369	29610±639	5.63±0.11	sdB	0.127±0.005	-11.289±0.007	0.142±0.007	14.2±1.9	0.31±0.11
294.635917	46.066417	247615029	2080063931448749824	12.114145±0.003894	2.4759±0.0316	30030±570	5.43±0.05	sdB	0.134±0.003	-10.574±0.021	0.240±0.005	42.1±3.7	0.56±0.08
294.82629	47.14856	354605098	2128554653197280512	15.38585±0.002842	0.6541±0.0337	29820±590	5.42±0.06	sdB	0.093±0.002	-11.235±0.039	0.196±0.010	27.4±3.6	0.37±0.06
296.05313	50.494251	354611122	2135353702585217920	15.461982±0.002862	0.6326±0.0288	27770±630	5.50±0.07	sdB	0.109±0.006	-11.225±0.015	0.209±0.008	23.4±2.6	0.51±0.12
297.984417	46.130778	165903109	2079522048319286528	13.609694±0.002819	1.2421±0.0239	39380±704	5.51±0.06	sdO	0.184±0.008	-10.950±0.027	0.198±0.004	84.1±7.8	0.46±0.07
298.28497	47.716728	354606155	2086441927825846656	14.981389±0.002823	0.7829±0.0269	28810±639	5.42±0.07	sdB	0.16±0.008	-11.109±0.015	0.220±0.008	30.1±3.6	0.46±0.08
299.231536	43.837941	355101074	20790096641541181312	14.320142±0.002865	1.4789±0.0224	39060±592	5.72±0.07	He-sdOB	0.365±0.015	-10.991±0.044	0.149±0.002	46.3±2.8	0.42±0.08
300.39346	44.574322	355208177	207613572430769872	15.435311±0.002811	0.618±0.0265	34260±590	5.29±0.17	sdB	0.502±0.080	-11.083±0.057	0.291±0.011	103.8±15.6	0.60±0.31
303.0673667	8.2691222	587214212	4251149700348007680	14.602394±0.002811	0.9721±0.0331	27730±606	5.39±0.08	sdB	0.142±0.005	-11.024±0.006	0.212±0.007	23.8±3.2	0.39±0.09
303.406715	9.467058	746301022	4299431347569705216	12.384984±0.002836	1.4616±0.0378	33430±575	5.15±0.06	sdOB	0.179±0.005	-10.659±0.039	0.333±0.010	123.7±9.3	0.57±0.09
311.28078	36.636963	470909040	1870606730148932224	16.453148±0.002828	0.8212±0.0411	25040±592	5.80±0.06	sdB	0.723±0.061	-11.045±0.132	0.172±0.010	10.5±1.7	0.69±0.13
312.413176	30.081818	475203139	1858674589447492608	13.487746±0.002857	1.2353±0.0317	37330±590	5.54±0.08	sdOB	0.196±0.005	-10.907±0.035	0.222±0.007	86.1±7.4	0.63±0.14
314.217996	3.596911	370216014	1731435633531386752	14.439921±0.002833	0.6749±0.0444	40220±795	5.27±0.07	sdO	0.061±0.001	-11.191±0.007	0.208±0.012	102.4±15.2	0.29±0.05
315.580451	1.576663	370205063	1729653290822954880	14.986846±0.002842	0.8823±0.0448	34480±639	5.73±0.09	sdOB	0.109±0.001	-11.227±0.005	0.150±0.007	28.4±4.8	0.45±0.11
315.813279	4.684184	370211146	17930719088696066176	16.548935±0.002834	0.5043±0.0625	29660±649	5.69±0.08	sdB	0.115±0.003	-11.461±0.017	0.149±0.007	15.4±5.3	0.39±0.19
315.885216	30.593842	475213199	1852616039853485824	12.92222±0.002776	2.5293±0.0315	34280±587	5.90±0.06	sdOB	0.2±0.007	-10.766±0.023	0.151±0.016	28.3±3.0	0.66±0.08
317.098329	1.032085	370208205	2690647825256267264	15.966711±0.002886	0.5776±0.0639	25480±754	5.33±0.07	sdB	0.098±0.002	-11.288±0.045	0.194±0.027	14.4±3.1	0.29±0.11
317.36219	37.139663	680412153	1868767831308190976	15.267942±0.00283	0.7334±0.0317	50100±1725	5.53±0.07	sdO	0.199±0.013	-11.330±0.032	0.140±0.005	111.3±22.8	0.24±0.05
317.372429	13.279525	371607236	1758993857339363776	15.401143±0.002826	0.7634±0.038	26520±722	5.52±0.08	sdB	0.088±0.004	-11.193±0.007	0.187±0.011	15.4±5.8	0.42±0.10
317.672454	14.433031	371606237	1759968097711823232	14.178232±0.002827	0.9612±0.0362	43210±626	5.83±0.06	He-sdOB	0.091±0.002	-11.152±0.005	0.160±0.007	79.7±8.8	0.64±0.11
318.417925	20.715492	372014020	179884048860848640	15.057672±0.002833	0.7586±0.0315	28520±644	5.29±0.06	sdB	0.089±0.001	-11.129±0.007	0.215±0.010	20.5±3.1	0.33±0.06
318.667075	20.911639	372014148	1789867186124831616	16.34555±0.002834	0.3383±0.0563	29020±602	5.32±0.06	sdB	0.092±0.002	-11.425±0.005	0.247±0.008	39.0±16.4	0.47±0.21
318.88115	12.665982	592402156	1746789866736764800	15.991699±0.003205	0.4664±0.0473	29120±675	5.55±0.07	sdB	0.056±0.001	-11.376±0.008	0.199±0.017	25.3±4.8	0.51±0.13
319.51366	14.681637	592414174	1759463868550744576	15.046289±0.002838	0.9129±0.0417	28960±569	5.60±0.06	sdB	0.06±0.002	-11.180±0.007	0.159±0.008	15.9±2.0	0.36±0.07
319.635091	23.571516	258303199	1792255325381143040	14.653358±0.002829	0.5225±0.0316	43100±613	5.43±0.06	He-sdOB	0.112±0.004	-11.230±0.005	0.251±0.015	194.8±29.4	0.60±0.19
319.858333	20.366419	469903131	1790470508770502144	15.966567±0.00289	0.3156±0.0515	43130±659	5.58±0.18	He-sdOB	0.087±0.001	-11.508±0.007	0.217±0.030	146.7±38.0	0.66±0.28
320.456296	20.371406	372015115	1790305753825533312	15.355061±0.002836	0.4837±0.0514	39600±649	5.33±0.08	sdO	0.072±0.003	-11.365±0.010	0.197±0.018	86.1±6.2	0.32±0.07
320.52329	21.686536	593111200	1790728894004387712	15.159798±0.002941	0.9229±0.0577	27620±592	5.50±0.06	sdB	0.104±0.002	-11.155±0.005	0.166±0.010	14.5±2.8	0.30±0.07
320.87692	0.710801	254804012	2690967057290240000	16.850067±0.002876	0.3802±0.0716	35050±630	5.89±0.07	He-sdOB	0.048±0.002	-11.642±0.008	0.133±0.035	23.4±5.1	0.49±0.36
321.435002	20.469909	503309030	1790336673293954176	13.357803±0.002788	1.0719±0.0342	50130±680	5.57±0.06	He-sdO	0.087±0.003	-11.015±0.005	0.197±0.007	218.4±16.0	0.53±0.10
321.5339	2.759411	677911144	2691867011851791744	16.131008±0.002867	0.5299±0.0618	29550±675	5.90±0.09	sdB	0.065±0.001	-11.405±0.013	0.162±0.025	17.9±3.9	0.77±0.29
321.70608	15.760201	592412140	1783628003096502144	17.022648±0.002946	0.3704±0.0738	34010±734	5.84±0.08	sdOB	0.079±0.002	-11.637±0.010	0.138±0.039	22.8±14.6	0.50±0.36
322.335678	29.268578	368208087	1850084998438797312	14.085997±0.002801	1.7159±0.0252	34710±592	6.17±0.06	sdOB	0.208±0.005	-10.986±0.011	0.134±0.004	23.4±1.9	0.96±0.12
322.871071	19.868555	503313058	1787066145893240576	13.139815±0.00282	2.6367±0.0362	39960±907	5.94±0.06	sdO	0.107±0.003	-10.924±0.012	0.101±0.001	23.3±2.5	0.73±0.05
322.510983	16.573053	158213246	1772138591918813056	14.428725±0.002831	0.9543±0.0354	37680±802	5.85±0.06	sdO	0.07±0.003	-11.135±0.051	0.170±0.006	51.8±9.9	0.34±0.15
322.64435	9.6801009	679901047	1741581170917641728	15.530628±0.002813	0.6804±0.0505	36590±582	5.79±0.07	sdOB	0.037±0.001	-11.399±0.004	0.128±0.009	26.0±3.3	0.37±0.07
323.58475	-6.962075	56403085	2667642399870553984	13.480331±0.002834	1.4836±0.0425	25510±741	5.21±0.05	sdB	0.03±0.001	-10.830±0.005	0.216±0.006	17.7±2.0	0.27±0.05
324.5772	34.351566	472809107	1950263255195349888	14.729849±0.002808	0.9599±0.0259	30340±592	5.41±0.06	sdB	0.166±0.001	-11.071±0.012	0.201±0.005	30.7±3.8	0.38±0.06

Table 1 continued on next page

Table 1 (continued)

RA	DEC	obs.id	G	parallax	T_{eff}	$\log g$	spclass	E(B-V)	Angular diameter	Radius	Luminosity	Mass
LAMOST (1)	LAMOST (2)	LAMOST (3)	Gaia EDR3 (4)	Gaia EDR3 (mas) (5)	(K) (7)	(cm s^{-2}) (8)	(9)	(10)	log(rad) (11)	R/R_{\odot} (12)	L/L_{\odot} (13)	M/M_{\odot} (14)
324.613116	46.192433	476303135	1977291346957976320	16.132805 ± 0.002829	29330 ± 639	5.80 ± 0.10	sdOB	0.354 ± 0.009	-11.233 ± 0.027	0.207 ± 0.011	28.3 ± 4.6	0.98 ± 0.33
324.833471	39.546916	172101139	1953965379566626816	14.714798 ± 0.002818	46900 ± 649	5.61 ± 0.10	He-sdOB	0.259 ± 0.008	-11.165 ± 0.007	0.179 ± 0.006	140.2 ± 12.8	0.48 ± 0.13
325.278181	25.474982	471009116	1797986937760585600	14.099944 ± 0.002905	43540 ± 613	5.91 ± 0.08	He-sdOB	0.065 ± 0.002	-11.153 ± 0.003	0.168 ± 0.006	90.8 ± 7.8	0.85 ± 0.20
325.676688	33.081334	472808084	1946937541760735872	14.77529 ± 0.002782	35950 ± 788	5.69 ± 0.12	sdOB	0.118 ± 0.004	-11.189 ± 0.004	0.146 ± 0.006	32.0 ± 4.3	0.38 ± 0.13
326.420157	-1.468957	266105200	2674696247998989184	15.2401 ± 0.002829	47260 ± 669	5.72 ± 0.12	He-sdOB	0.038 ± 0.001	-11.410 ± 0.006	0.191 ± 0.029	163.8 ± 52.5	0.72 ± 0.33
326.501298	37.355449	473209201	1952553606634620928	14.641872 ± 0.002799	51430 ± 669	5.74 ± 0.09	He-sdO	0.229 ± 0.006	-11.173 ± 0.017	0.155 ± 0.003	48.0 ± 7.1	0.48 ± 0.10
328.835563	11.297908	371315006	272683230013742336	15.336716 ± 0.002874	35470 ± 579	5.80 ± 0.07	sdOB	0.065 ± 0.002	-11.328 ± 0.019	0.111 ± 0.006	17.4 ± 2.5	0.28 ± 0.06
329.4386	-2.025295	266107138	2679677791586720896	16.5008 ± 0.002986	29290 ± 573	5.51 ± 0.07	sdB	0.131 ± 0.004	-11.429 ± 0.059	0.162 ± 0.031	17.3 ± 3.8	0.32 ± 0.15
329.80546	14.30136	378803208	1768547964899107584	16.167128 ± 0.002926	34370 ± 899	5.30 ± 0.11	sdB	0.081 ± 0.001	-11.407 ± 0.015	0.190 ± 0.020	24.0 ± 4.8	0.27 ± 0.08
330.2594	8.513191	256811238	2724882872133120512	13.108753 ± 0.002853	65560 ± 1556	5.83 ± 0.07	He-sdOB	0.055 ± 0.002	-11.488 ± 0.011	0.112 ± 0.010	15.8 ± 3.3	0.37 ± 0.12
331.015786	14.777294	378809160	1768493259900525312	15.776851 ± 0.00289	42900 ± 995	5.65 ± 0.09	He-sdOB	0.042 ± 0.001	-11.495 ± 0.007	0.117 ± 0.012	42.7 ± 8.3	0.23 ± 0.07
331.818739	3.705491	61309195	268400928284602880	14.187351 ± 0.002903	32180 ± 579	5.97 ± 0.07	sdB	0.032 ± 0.001	-11.077 ± 0.005	0.115 ± 0.003	12.7 ± 1.1	0.45 ± 0.09
332.002469	2.562084	381708131	2683585696429935488	14.10796 ± 0.002884	27610 ± 639	5.62 ± 0.05	sdB	0.03 ± 0.0	-10.992 ± 0.005	0.158 ± 0.004	13.1 ± 1.6	0.39 ± 0.06
332.5111298	25.066193	164209157	1879544900675463552	12.805006 ± 0.002797	21290 ± 570	5.32 ± 0.05	sdB	0.072 ± 0.002	-10.610 ± 0.005	0.232 ± 0.004	10.0 ± 1.2	0.41 ± 0.06
333.826383	16.617652	505803150	1775141422597602176	16.835752 ± 0.002986	59800 ± 1399	5.53 ± 0.07	sdO	0.045 ± 0.0	-11.746 ± 0.021	0.109 ± 0.018	70.8 ± 23.6	0.15 ± 0.05
334.029951	15.060714	505805092	2735467282163538944	16.952951 ± 0.003049	34620 ± 824	5.89 ± 0.08	sdOB	0.052 ± 0.001	-11.646 ± 0.022	0.103 ± 0.024	33.7 ± 4.1	0.30 ± 0.10
334.07485	13.85585	470416164	273420006494745232	15.813065 ± 0.00297	23150 ± 621	5.05 ± 0.07	sdB	0.062 ± 0.001	-11.245 ± 0.014	0.362 ± 0.053	13.8 ± 12.5	0.54 ± 0.19
335.344036	5.416204	75501161	270840023075920768	15.265286 ± 0.002901	35340 ± 635	5.86 ± 0.08	He-sdOB	0.097 ± 0.002	-11.296 ± 0.008	0.109 ± 0.005	16.4 ± 1.6	0.31 ± 0.06
335.57083	26.93794	594102069	1881671180067646080	16.747202 ± 0.002893	28760 ± 626	5.38 ± 0.10	sdB	0.063 ± 0.001	-11.487 ± 0.051	0.179 ± 0.035	19.5 ± 4.9	0.27 ± 0.16
335.57458	27.588819	594105250	1881776668761026688	15.47918 ± 0.00287	50650 ± 2817	5.56 ± 0.23	sdO	0.068 ± 0.001	-11.423 ± 0.062	0.158 ± 0.019	146.7 ± 57.9	0.34 ± 0.14
335.66121	0.856942	382504121	2679230771390593024	16.287024 ± 0.002944	50190 ± 1192	5.55 ± 0.09	sdO	0.062 ± 0.002	-11.610 ± 0.007	0.171 ± 0.039	164.4 ± 53.5	0.38 ± 0.15
337.765186	12.285902	157014157	2730881326537936896	15.679758 ± 0.002881	41950 ± 1020	5.40 ± 0.08	sdO	0.063 ± 0.003	-11.445 ± 0.014	0.175 ± 0.023	85.5 ± 34.9	0.28 ± 0.14
338.731397	31.39054	1203114	190071035773768448	16.448002 ± 0.002857	42390 ± 707	5.93 ± 0.50	He-sdOB	0.068 ± 0.002	-11.634 ± 0.013	0.168 ± 0.044	129.2 ± 73.4	0.47 ± 0.26
339.4026	22.73709	490614158	1874534323107953664	12.734753 ± 0.002806	47390 ± 1054	5.40 ± 0.06	sdO	0.034 ± 0.001	-10.881 ± 0.008	0.209 ± 0.009	128.5 ± 18.7	0.90 ± 0.68
339.806068	13.636279	157011113	2731836527264665856	14.911298 ± 0.00285	32200 ± 692	5.66 ± 0.06	sdB	0.044 ± 0.001	-11.211 ± 0.006	0.201 ± 0.014	38.9 ± 5.8	0.68 ± 0.13
339.981606	-0.877811	362205243	2653065864983035392	15.054759 ± 0.002934	42060 ± 610	5.45 ± 0.06	He-sdOB	0.044 ± 0.001	-11.306 ± 0.173	0.193 ± 0.018	105.9 ± 14.5	0.38 ± 0.09
340.0594	2.10893	362211023	2654860474117172900	15.878462 ± 0.002961	28280 ± 602	5.38 ± 0.07	sdB	0.078 ± 0.001	-11.328 ± 0.014	0.178 ± 0.023	18.8 ± 4.6	0.28 ± 0.09
340.0884	12.09255	379902114	2729936846049609728	16.736578 ± 0.002943	30670 ± 635	5.42 ± 0.09	sdB	0.046 ± 0.001	-11.558 ± 0.008	0.138 ± 0.021	15.1 ± 4.6	0.18 ± 0.06
340.718491	1.872661	362211238	2654793575707334784	14.423444 ± 0.002884	31140 ± 572	5.93 ± 0.06	sdB	0.051 ± 0.001	-11.090 ± 0.018	0.120 ± 0.003	12.1 ± 1.3	0.44 ± 0.06
340.871872	10.781563	157006179	2717582699040219392	15.023709 ± 0.002856	34270 ± 592	5.77 ± 0.07	sdOB	0.054 ± 0.001	-11.261 ± 0.007	0.144 ± 0.009	25.7 ± 4.0	0.45 ± 0.10
341.26507	32.364203	680503235	1890677009230168704	13.979491 ± 0.002818	31020 ± 613	5.70 ± 0.07	sdB	0.089 ± 0.002	-10.987 ± 0.004	0.159 ± 0.003	20.9 ± 1.9	0.45 ± 0.09
341.7299	15.5164	354509102	2732552133240294272	15.702261 ± 0.002888	41210 ± 566	5.51 ± 0.06	He-sdOB	0.079 ± 0.002	-11.439 ± 0.048	0.140 ± 0.016	51.1 ± 8.4	0.23 ± 0.07
341.890375	31.325914	264909113	1889631201873127424	15.430312 ± 0.002803	28940 ± 613	5.55 ± 0.07	sdB	0.051 ± 0.001	-11.267 ± 0.006	0.179 ± 0.013	20.2 ± 2.9	0.41 ± 0.09
341.89198	33.011002	680503175	1890817059523265024	15.982396 ± 0.002848	26720 ± 610	5.55 ± 0.06	sdB	0.098 ± 0.006	-11.312 ± 0.059	0.219 ± 0.010	22.1 ± 5.6	0.62 ± 0.18
342.301397	22.301397	353313201	2836713031563656704	16.008276 ± 0.002871	47740 ± 846	5.35 ± 0.10	He-sdOB	0.074 ± 0.005	-11.540 ± 0.005	0.196 ± 0.027	180.7 ± 47.0	0.32 ± 0.10
343.092447	33.719939	370916040	1801098500140100352	12.749049 ± 0.002781	28650 ± 626	5.64 ± 0.09	sdB	0.098 ± 0.007	-10.698 ± 0.026	0.212 ± 0.004	27.0 ± 2.6	0.71 ± 0.13
344.15977	6.947641	256106208	1712047826225618048	15.238307 ± 0.002859	29920 ± 626	5.65 ± 0.07	sdB	0.063 ± 0.002	-11.231 ± 0.027	0.140 ± 0.009	14.1 ± 2.3	0.32 ± 0.08
345.4409	13.64374	363809200	281515323450428032	14.504062 ± 0.003616	31190 ± 606	5.73 ± 0.07	sdB	0.094 ± 0.007	-11.078 ± 0.009	0.155 ± 0.006	20.3 ± 2.1	0.46 ± 0.06
347.33042	36.899804	678214001	19151448289773812352	16.382402 ± 0.002842	33520 ± 971	5.68 ± 0.07	sdOB	0.1 ± 0.002	-11.481 ± 0.007	0.139 ± 0.013	21.8 ± 4.5	0.34 ± 0.10
347.375115	28.568276	470009143	2845710850610464640	14.462544 ± 0.002821	31890 ± 587	5.73 ± 0.06	sdOB	0.096 ± 0.004	-11.088 ± 0.005	0.146 ± 0.005	20.0 ± 1.9	0.42 ± 0.06

Table 1 continued on next page

Table 1 (continued)

RA	DEC	obs.id	source.id	G	parallax	T_{eff}	$\log g$	spclass	E(B-V)	Angular diameter	Radius	Luminosity	Mass
LAMOST (1)	LAMOST (2)	LAMOST (3)	Gaia EDR3 (4)	Gaia EDR3 (mag) (5)	Gaia EDR3 (mas) (6)	(K) (7)	(cm s^{-2}) (8)	(9)	(10)	log(rad) (11)	R/R_{\odot} (12)	L/L_{\odot} (13)	M/M_{\odot} (14)
347.558118	34.032284	264102247	1911572540520290048	15.418233 \pm 0.002848	0.4956 \pm 0.0502	49490 \pm 1004	5.62 \pm 0.10	He-sdOB	0.065 \pm 0.001	-11.436 \pm 0.043	0.162 \pm 0.018	138.9 \pm 40.4	0.41 \pm 0.14
350.90066	45.217675	587411151	1937879932466496896	17.042416 \pm 0.002882	0.5112 \pm 0.0647	23950 \pm 1791	5.81 \pm 0.12	sdB	0.162 \pm 0.008	-11.463 \pm 0.009	0.150 \pm 0.024	6.5 \pm 3.4	0.54 \pm 0.31
351.37223	41.518334	587405077	1923590271333313792	16.265299 \pm 0.002808	0.603 \pm 0.0453	38370 \pm 868	5.90 \pm 0.09	sdOB	0.127 \pm 0.004	-11.499 \pm 0.009	0.116 \pm 0.010	26.6 \pm 4.8	0.39 \pm 0.14
351.527451	5.270987	158603071	2661097763064489600	15.3873 \pm 0.002886	0.7104 \pm 0.0537	29340 \pm 569	5.64 \pm 0.06	sdB	0.054 \pm 0.001	-11.260 \pm 0.025	0.171 \pm 0.016	19.4 \pm 4.3	0.47 \pm 0.10
352.34432	32.233162	593503117	2872454748672529280	16.906975 \pm 0.004601	0.3954 \pm 0.0678	31070 \pm 630	5.49 \pm 0.09	sdB	0.12 \pm 0.009	-11.548 \pm 0.018	0.158 \pm 0.037	21.2 \pm 10.9	0.29 \pm 0.18
353.68925	51.004629	689015198	1944738965178800384	15.999136 \pm 0.002822	0.4587 \pm 0.0383	37140 \pm 747	5.53 \pm 0.06	sdO	0.181 \pm 0.003	-11.403 \pm 0.012	0.190 \pm 0.014	61.3 \pm 9.3	0.44 \pm 0.19
354.17191	31.533466	593504113	2871378846483069184	16.841461 \pm 0.002846	0.4286 \pm 0.0631	33470 \pm 630	5.96 \pm 0.07	sdB	0.077 \pm 0.004	-11.589 \pm 0.026	0.132 \pm 0.026	19.5 \pm 9.3	0.59 \pm 0.30
355.01197	7.285939	361504161	2757157489778320000	13.451859 \pm 0.00281	2.2099 \pm 0.0323	30720 \pm 596	5.93 \pm 0.08	sdB	0.131 \pm 0.003	-10.831 \pm 0.018	0.148 \pm 0.002	17.4 \pm 1.6	0.68 \pm 0.17
355.66937	43.91102	678701017	1925782766239946624	16.125372 \pm 0.002806	0.3258 \pm 0.0453	39780 \pm 741	5.29 \pm 0.07	sdO	0.102 \pm 0.005	-11.494 \pm 0.005	0.217 \pm 0.027	107.9 \pm 27.9	0.34 \pm 0.06
358.822256	18.337599	54914220	2774038154361038976	13.313434 \pm 0.002813	1.1301 \pm 0.0405	47080 \pm 1105	5.44 \pm 0.14	He-sdOB	0.033 \pm 0.0	-11.025 \pm 0.006	0.184 \pm 0.006	146.9 \pm 18.8	0.35 \pm 0.14
359.439198	24.43959	492005208	2851511427281425536	16.330795 \pm 0.002858	0.4081 \pm 0.0662	53970 \pm 6514	5.61 \pm 0.08	sdO	0.117 \pm 0.009	-11.578 \pm 0.011	0.144 \pm 0.031	160.3 \pm 135.6	0.31 \pm 0.18

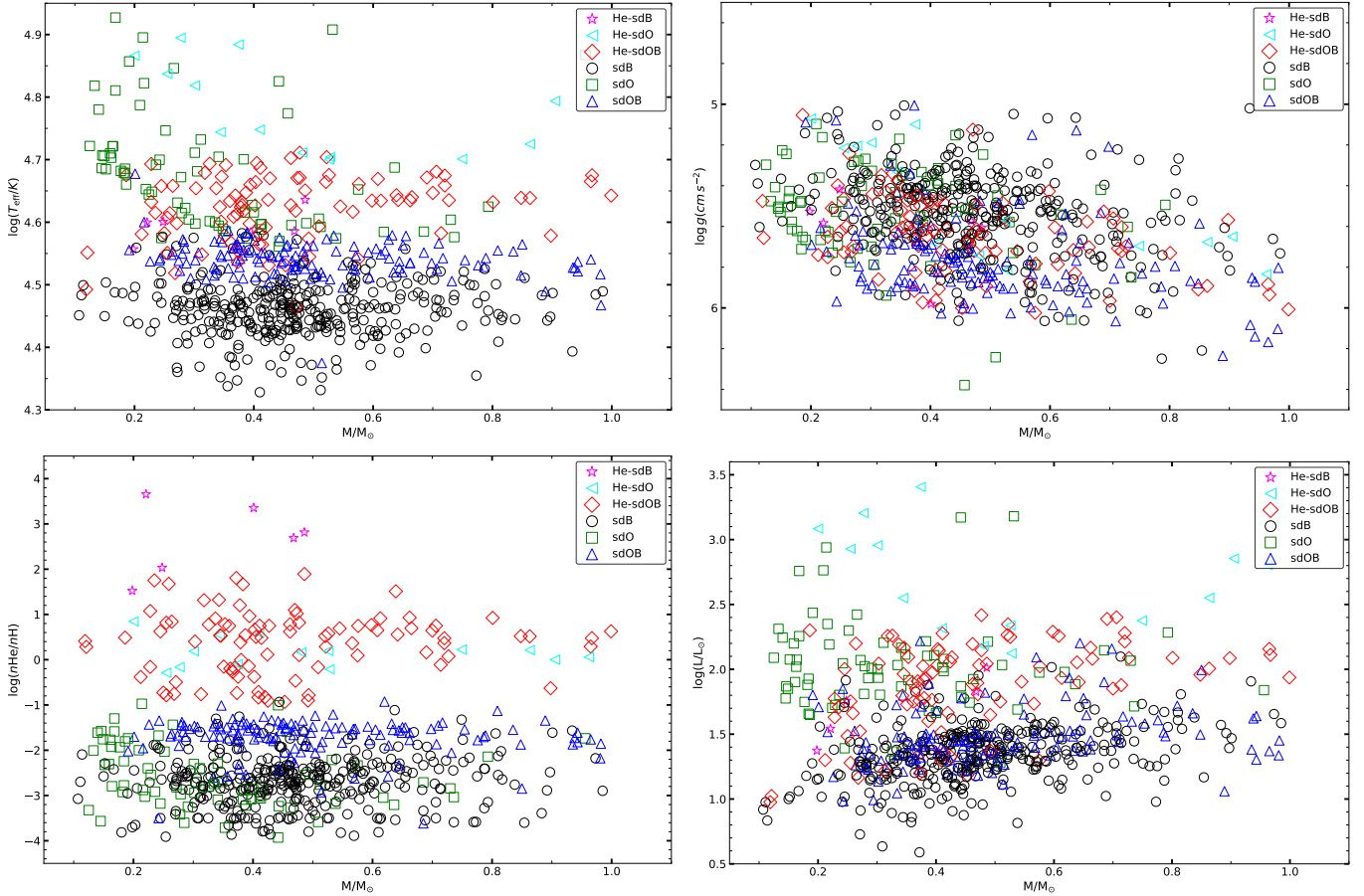


Figure 2. Relationship between mass and atmospheric parameters for the selected hot subdwarfs. From upper left to bottom right, it shows mass - T_{eff} plane, mass - $\log g$ plane, mass - $\log(n\text{He}/n\text{H})$ plane and mass - luminosity plane, respectively. The labels with different colors denote the spectral classification of hot subdwarfs from Lei et al. (2018, 2019b, 2020). Parameter errors are not shown for clarity.

3.1. Mass vs. atmospheric parameters

The four panels in Fig 2 show the relationships we found between masses and atmospheric parameters (e.g., T_{eff} , $\log g$, $\log(n\text{He}/n\text{H})$ and luminosity) for the selected hot subdwarfs. As one can see that, no obvious characteristics are contained in mass - T_{eff} plane (upper left panel), mass - $\log g$ plane (upper right panel) and mass - $\log(n\text{He}/n\text{H})$ plane (bottom left panel). Note that the detailed discussion of the relationships among atmospheric parameters for the selected hot subdwarfs can be found in Section 3.2 of Lei et al. (2018) and Section 4.1 of Lei et al. (2019b).

On the other hand, as shown in the mass - luminosity plane (bottom right panel), though a wide mass distribution (e.g., roughly from 0.1 to 1.0 M_{\odot} , see Section 3.3 for detailed discussion) is presented, most of sdB (black circles) and sdOB (blue triangles) stars settle in a narrow range at a relatively low luminosity (e.g., roughly from $\log(L/L_{\odot}) = 0.5$ to 1.5), which demonstrates that these stars are still at the core He burning stage.

However, most sdO (green squares) and He-rich stars, i.e., He-sdO (aqua right triangles), He-sdOB (red diamonds), and He-sdB (magenta stars), show a much higher and wider range of luminosities than sdB and sdOB stars. Some of them even present luminosity near 3000 L_{\odot} (e.g., $\log(L/L_{\odot}) = 3.5$). These results demonstrate that they could either have evolved off the core He-burning stage and now are on the way to the WD cooling curve, or could be pre-EHB stars that just cross the hot subdwarf region. This result is also clearly shown in Fig 3, in which the relationships between T_{eff} and luminosity for the selected hot subdwarfs are presented. As shown in the figure, most sdB and sdOB stars show a much narrower T_{eff} and luminosity range than that of sdO and He-rich hot subdwarfs (also see Fig 10 in Schaffenroth et al. 2022), and located well in the region defined by the zero-age horizontal branch (ZAHB) and the terminal-age horizontal branch (TAHB) lines.

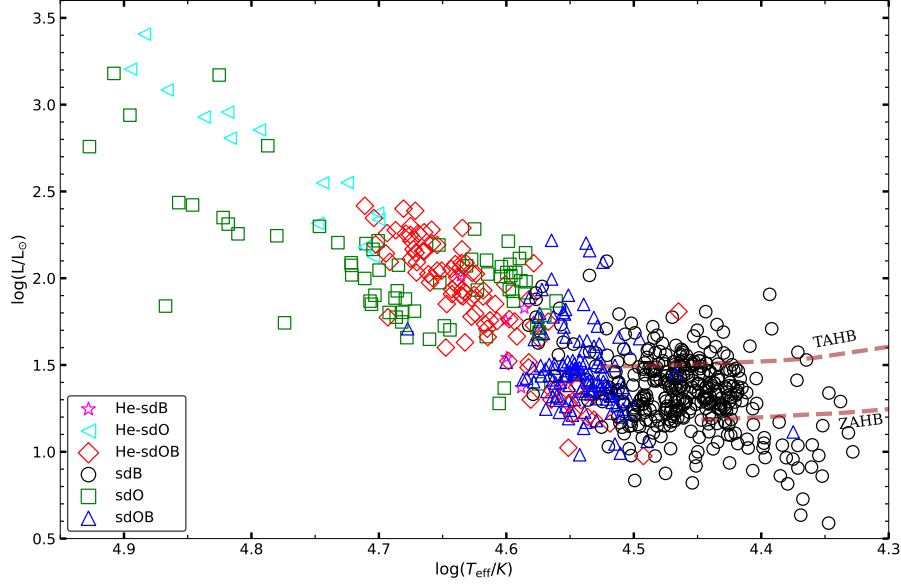


Figure 3. T_{eff} – luminosity plane for the hot subdwarf stars selected in this study. The labels with different colors denote the same spectral classifications as in Fig 2. The two brown dashed lines denote the ZAHB and TAHB positions for HB stars with $[\text{Fe}/\text{H}] = -1.48$ from [Dorman et al. \(1993\)](#).

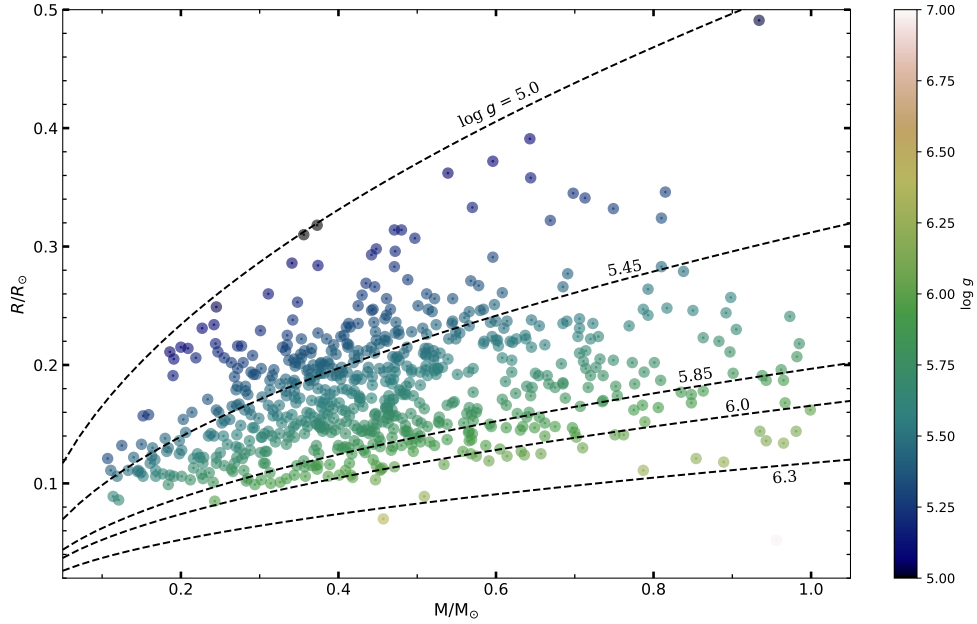


Figure 4. Mass – radius plane for the hot subdwarf stars selected in this study. Color bar in the right denotes different $\log g$ values, while black dashed curves from top to bottom denote constant $\log g$ values of 5.0, 5.45, 5.85, 6.0 and 6.3 dex, respectively.

Fig 4 shows the relationship between mass and radius for our selected sample. $\log g$ values for each object were denoted by the color gradient showed in the right. Most of hot subdwarf stars in our sample have radius between 0.1 and $0.4 R_{\odot}$, while most of the objects have $\log g$ values between 5.0 and 6.3 dex. The black dashed curves reveal the relationship between mass and radius that square of radius has positive correlation with stellar mass when $\log g$ kept constant (see Equation 2). Since all spectral type of hot subdwarfs present relative wide distributions of $\log g$ (see the upper right panel in Fig 2), it is not easy to distinguish them in this figure. Therefore, stars with different spectral classifications were not denoted by different labels as in Fig 2 and 3.

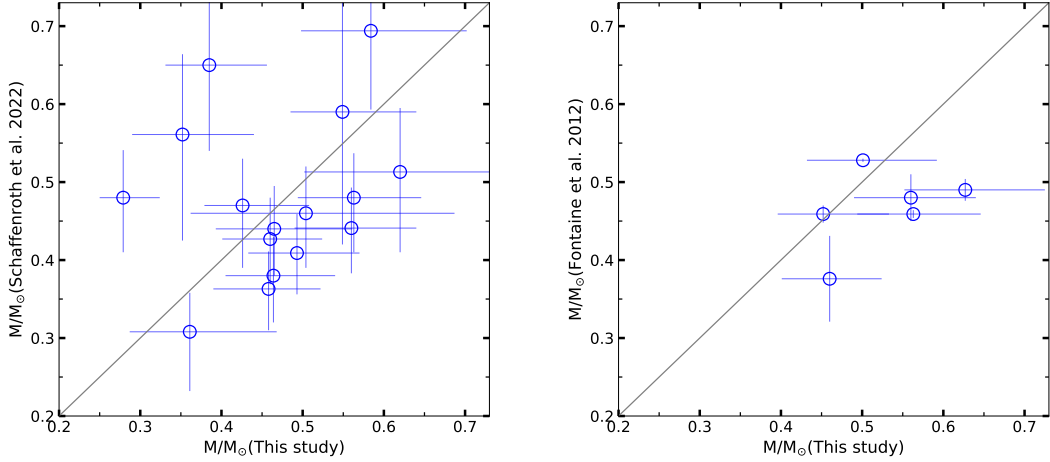


Figure 5. Left panel: Mass comparison between this study and Schaffenroth et al. (2022). Right panel: Mass comparison between this study and Fontaine et al. (2012).

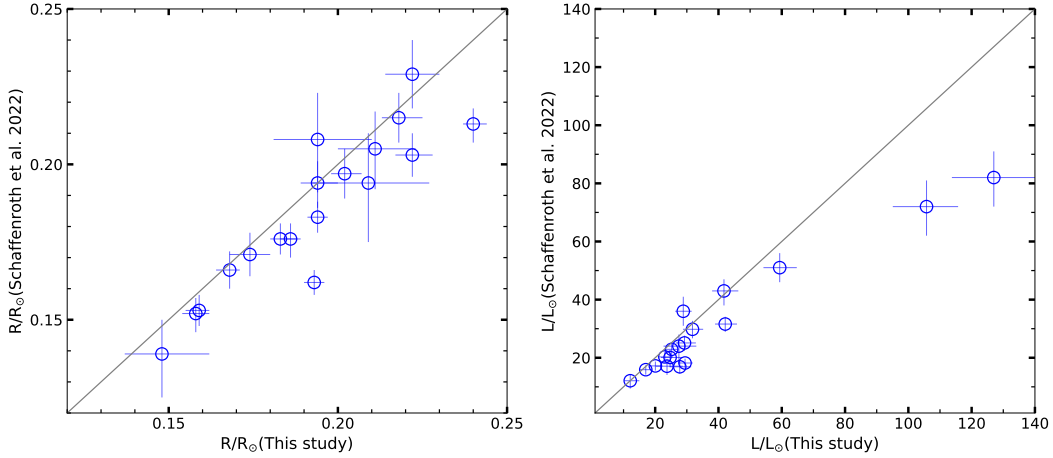


Figure 6. Radius and luminosity comparison between this study and Schaffenroth et al. (2022)

3.2. Mass values comparison with other studies

To check the reliability of the mass obtained in this study, we cross-matched the selected stars with the sample analyzed by Schaffenroth et al. (2022) and Fontaine et al. (2012) (see Section 1), and found 18 and 6 common objects, respectively. In Fig 5, we compared masses obtained in this study with the values of common objects in Schaffenroth et al. (2022) (left panel) and Fontaine et al. (2012) (right panel). Although considerable dispersion is present in both panels, the masses obtained in this study are consistent with the two former studies when the uncertainties are also considered. Note that, the uncertainties for our mass values are mainly from the large uncertainties of $\log g$ and distances. Considering that we have a large number of samples (e.g., 664 hot subdwarf stars), it will not influence much the analysis and interpretation of the mass distribution in this study.

In Fig 6, we also compared the radius and luminosity obtained in this study with the values by Schaffenroth et al. (2022). As shown in the two panels, since $\log g$ values were not used when calculating radius and luminosity, both the radius and luminosity values show much better consistency than the direct mass comparison between the two studies.

3.3. Mass distributions for the selected hot subdwarf stars

To study the mass distribution at different parallax precisions, we selected three groups of hot subdwarf stars from our sample for a mass distribution analysis, i.e., objects with $\sigma_{\varpi}/\varpi \leq 0.2$ were selected as Group 1, objects with

Table 2. Statistical properties for hot subdwarf stars in three groups.

Group	Subset	Total	Peak mass	Mean mass	Massive sample	Massive sample
Name	Name	Number	M_{\odot}	M_{\odot}	Number	Fraction(%)
Group 1 ($\sigma_{\varpi}/\varpi \leq 0.2$)	All sample	664	0.46	0.46	136	20
	sdB/sdOB	483	0.46	0.48	105	22
	He-rich sample	110	0.40	0.46	24	22
	sdO	71	0.18	0.34	7	10
Group 2 ($\sigma_{\varpi}/\varpi \leq 0.1$)	All sample	503	0.46	0.47	100	20
	sdB/sdOB	376	0.46	0.48	80	21
	He-rich sample	75	0.36	0.46	15	20
	sdO	52	0.18	0.33	5	10
Group 3 ($\sigma_{\varpi}/\varpi \leq 0.05$)	All sample	289	0.46	0.48	58	20
	sdB/sdOB	220	0.46	0.48	44	20
	He-rich sample	39	0.42	0.50	9	23
	sdO	30	0.18	0.36	5	16

NOTE—We define massive samples as objects with a mass larger than $0.6 M_{\odot}$.

$\sigma_{\varpi}/\varpi \leq 0.1$ were selected as Group 2, and objects with $\sigma_{\varpi}/\varpi \leq 0.05$ were selected as Group 3. The statistical information for subsets with different spectral types in the three groups is listed in Table 2. From left to right, it gives the group name, subset name, number count, peak mass of the distribution, mean mass, number of stars in the massive sample, and the relative fraction of the massive sample to the total, respectively.

With an increasing parallax precision the number of stars within each group decreases. Group 1 contains all the 664 selected hot subdwarfs, Group 2 has 503 hot subdwarfs, and Group 3 consists of 289 hot subdwarfs. The number fractions of each subset with different spectral types are consistent among the three groups, e.g., sdB/sdOB stars are the largest population in each group which represents about 73% of the total, while He-rich stars (He-rich sdB/sdOB/sdO) and sdO stars in each group present about 16% and 10%, respectively. Furthermore, the peak of the mass distribution for each subset in the three groups is nearly the same, e.g., sdB/sdOB stars present a peak mass of about $0.46 M_{\odot}$ (also see Fig 8), He-rich stars present a peak mass at $0.4 M_{\odot}$, while sdO stars present an inconspicuous peak mass of about $0.18 M_{\odot}$.

The left panel in Fig 7 shows the mass distributions for the whole sample in each group. The mass distributions are very similar among the three groups, most of the hot subdwarf stars have masses between 0.37 and $0.5 M_{\odot}$, and a sharp peak at $0.46 M_{\odot}$ is present. However, Group 3 (i.e., red-dotted histogram) seems to have much fewer stars with a mass between 0.2 and $0.37 M_{\odot}$ than Group 1 (i.e., black-solid histogram) and Group 2 (i.e., blue-dashed histogram). This feature is shown more clearly in the right panel of Fig 7, in which the number counts in each bin were normalized. One can see that with the parallax (distance) precision increasing, the relative number of less massive objects (e.g., mass between 0.2 and $0.37 M_{\odot}$) decreases, which leads to a sharper peak at the low mass side. It means that with larger uncertainties in parallax (distance) the relative contribution of low-mass objects show an increase. On the other hand, massive stars (e.g., $M > 0.6$) present nearly the same mass distribution among three groups, independent of the parallax precision.

The left panel in Fig 8 shows the mass distributions of hot subdwarfs with different spectral types in Group 1. One can see that the whole sample presents a very wide mass distribution (black solid histogram) from $0.1 M_{\odot}$ to $1.0 M_{\odot}$, with a sharp peak (mean mass) at $0.46 M_{\odot}$. Since sdB and sdOB stars have the largest fraction in the group (e.g., 483 objects in a total of 664, or about 73% in percentage), they show very similar mass distributions (magenta dash-dotted histogram) as the whole sample. They also present a sharp mass peak around $0.46 M_{\odot}$ (see Table 2).

On the other hand, both He-rich stars (e.g., He-sdB, He-sdO, He-sdOB) and sdO stars present much flatter mass distributions (denoted by blue dashed and green dotted histograms, respectively) when compared with sdB/sdOB

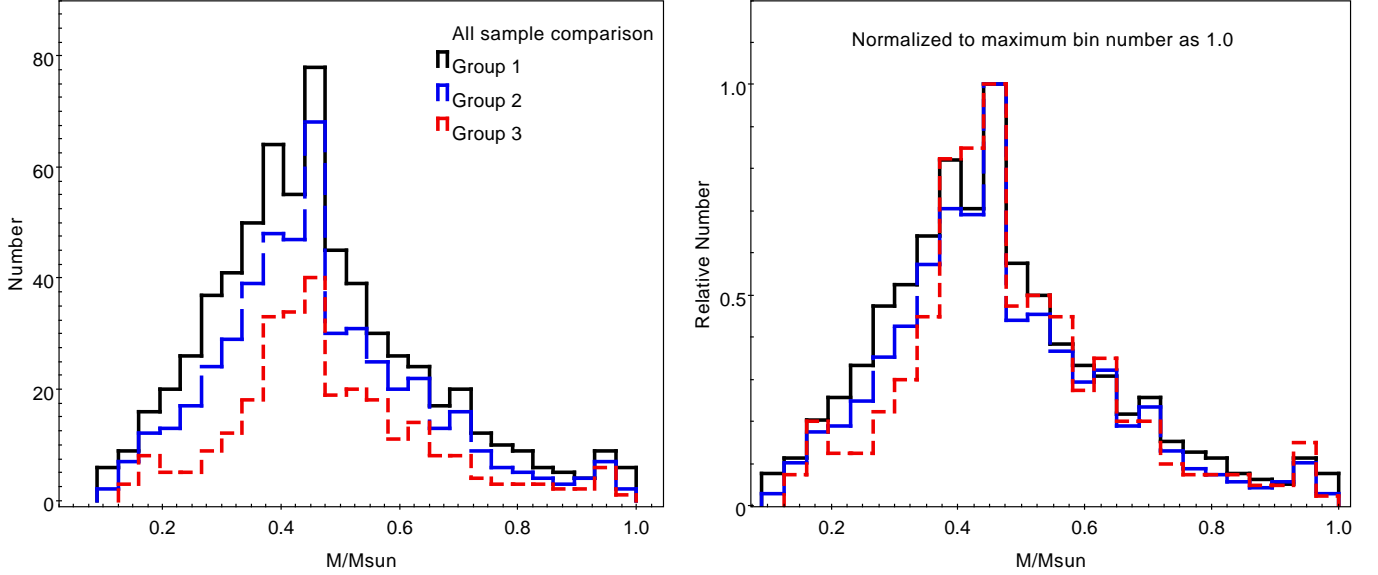


Figure 7. Mass distributions for all types of hot subdwarf stars in three groups. Left panel: Absolute numbers in each bin. Right panel: Numbers in each group were normalized to the maximum. Black solid, blue long-dashed, and red short-dashed histograms denote the mass distribution for hot subdwarf stars in Groups 1, 2, and 3, respectively. The bin size is set to $0.035 M_{\odot}$, and 26 bins are present in the mass range of 0.1 to $1.0 M_{\odot}$.

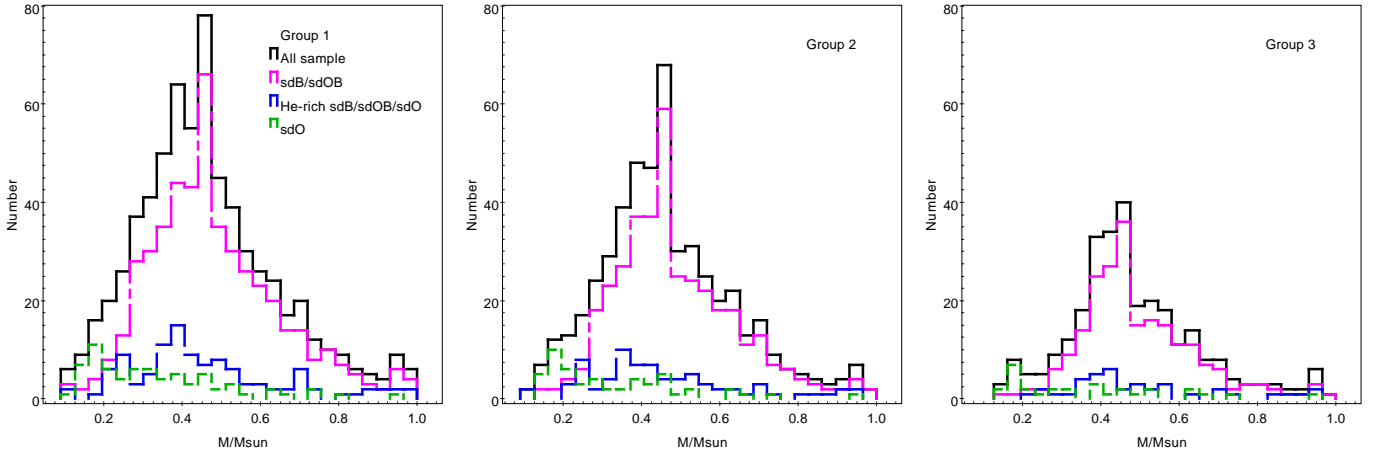


Figure 8. Mass distribution for the selected hot subdwarfs with different spectral classifications in three groups. In each group, the mass distributions for all samples, sdB/sdOB stars, He-rich stars, and sdO stars are denoted by black solid, magenta dash-dotted, blue dashed, and green dotted histograms, respectively. The bin size is the same as in Fig 7.

stars. Moreover, He-rich stars show a small mass peak near $0.40 M_{\odot}$ and have a mean mass of about $0.46 M_{\odot}$. While sdO stars present an inconspicuous peak mass around at $0.18 M_{\odot}$ and a mean mass of about $0.34 M_{\odot}$, which is obviously smaller than the values of sdB/sdO and He-rich stars. If we consider stars with a mass greater than $0.6 M_{\odot}$ as massive hot subdwarfs, the fraction of massive stars in the sdO sample is about 10% (e.g., 7 out of 71, see Table 2), while this fraction among other types of hot subdwarfs (e.g., sdB/sdOB, He-rich sample) are both around at 20%. Note that, according to the results of Han et al. (2002), the minimum core mass for He ignition in a star is about $0.3 M_{\odot}$ (see Table 1 in their study). It means that the low-mass sdO stars found in our sample probably did not undergo a core He burning phase (see detailed discussion in Section 4.4).

The middle and right panel of Fig 8 show the mass distribution of hot subdwarfs with different spectral types in Group 2 and 3 respectively. Mass distributions for the various subsets in the two groups are very similar to the distributions of the corresponding subsets in Group 1, except that less massive stars become fewer with an increasing

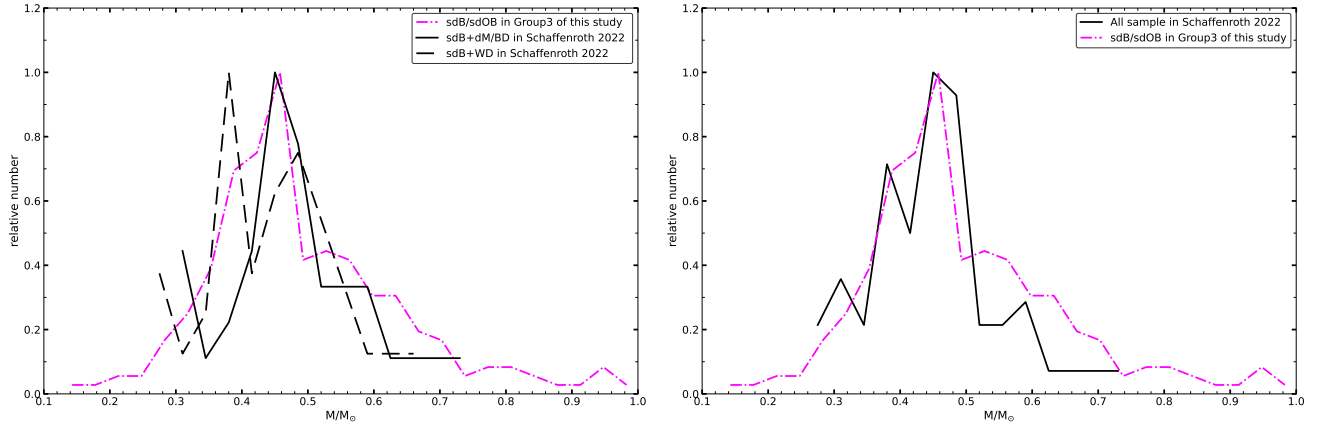


Figure 9. Mass distribution comparison for sdB/sdOB stars in Group 3 with sdB stars in Schaffenroth et al. (2022). Left panel: Mass distribution for sdB+dM/BD (black solid curve) and sdB+WD systems (black dashed curve) in Schaffenroth et al. (2022) are plotted separately. Right panel: Both sdB+dM/BD and sdB+WD systems in Schaffenroth et al. (2022) were put together to plot the mass distribution (black solid curve). In each panel, the magenta dash-dotted curve denotes the mass distribution for sdB/sdOB stars in Group 3. All distributions were normalized to the maximum values for a better comparison.

parallax precision (distance) from Group 1 to Group 3, as shown in Fig 7. Considering that higher parallax precision (distance) means more reliable mass determination, we used hot subdwarf stars in Group 3 to compare the mass distribution with other studies in the following sections.

4. DISCUSSION

4.1. Mass distribution comparison with other studies

Combining high-quality light curves from the Transiting Exoplanet Survey Satellite (TESS, Ricker et al. 2015) and the *K2* space mission (Howell et al. 2014) with the fit of SED, distance from *Gaia* and atmospheric parameters from literature, Schaffenroth et al. (2022) not only derived the properties of primary and secondary stars in about 200 sdB binaries but also obtained absolute masses, radii, and luminosities for 68 sdB stars with different types of companions. They found a broad mass distribution for sdB stars with cool, low-mass stellar or sub-stellar companions (i.e., sdB+dM/BD systems), which present a peak mass at $0.46 M_{\odot}$. Though the mass distribution of sdB stars with WD companions (i.e., sdB+WD systems) also has a similar width as sdB+dM/BD systems, they have a much smaller peak mass around $0.38 M_{\odot}$ (see Section 3.2 and Fig 12 in their study). Based on this result, they concluded that sdB+dM/BD and sdB+WD systems originate from different populations.

In the left panel of Fig 9, we compared the mass distributions for sdB+dM/BD and sdB+WD systems obtained in Schaffenroth et al. (2022) separately with the mass distribution for sdB/sdOB stars of Group 3 in this study. All the sample numbers in each bin are normalized to the maximum bin number which has been set to 1. One can see that the mass distribution for sdB/sdOB stars in Group 3 (magenta dash-dotted curve, e.g., roughly from 0.1 to $1.0 M_{\odot}$) is generally wider than the mass distribution for both sdB+dM/BD (black solid curve, e.g., roughly from 0.3 to $0.74 M_{\odot}$) and sdB+WD systems (black dashed curve, e.g., from 0.28 to $0.68 M_{\odot}$). Note that, the atmospheric parameters for our sample are obtained by fitting H and He profiles in Lei et al. (2018, 2019b, 2020), with no metal opacities included. The inclusion of metals can potentially change the T_{eff} and $\log g$ values, thus resulting in slightly different masses. Moreover, the number of sdB stars analyzed in this study is much bigger than that of in Schaffenroth et al. (2022), e.g., 220 vs 68. Though these factors would act towards a wider mass distribution, they will not influence the observed mass distribution tendencies as significantly. The peak of the mass distribution for our sdB/sdOB stars is nearly the same as the one for sdB+dM/BD systems (at $0.46 M_{\odot}$). Furthermore, there is also a second mass peak around $0.38 M_{\odot}$ for our sdB/sdOB stars, which is corresponding to the peak mass of sdB+WD systems in Schaffenroth et al. (2022).

Note that, we cannot separate sdB+dM/BD and sdB+WD systems in our sample without additional information, e.g., light curves. Therefore, we compared the total mass distribution in the right panel of Fig 9 for all sdB binaries in Schaffenroth et al. (2022) (black solid curve) with the mass distribution for our sdB/sdOB stars in Group 3 (magenta dash-dotted curve). We find the two mass distributions to be consistent with each other, especially on the low mass

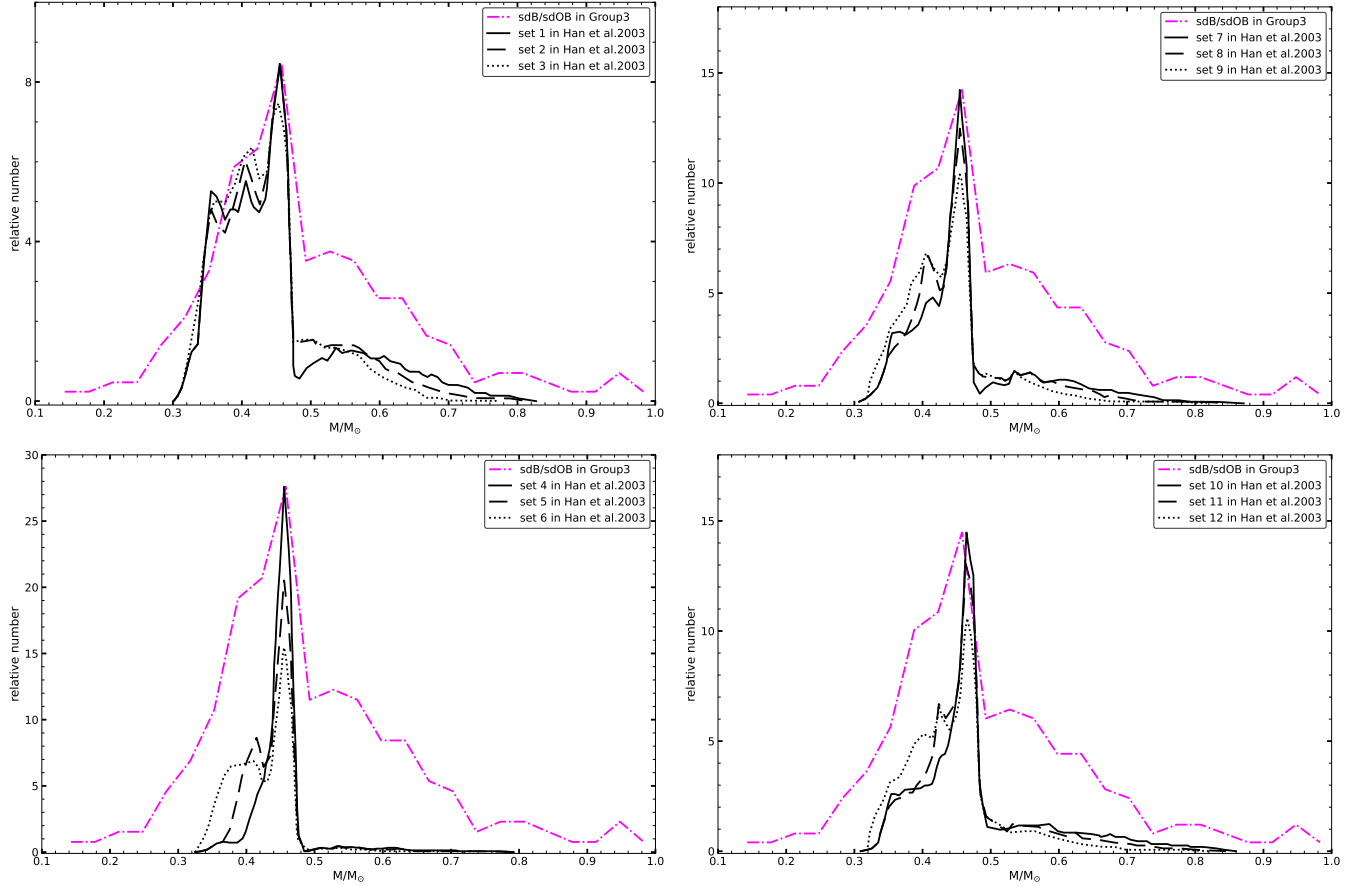


Figure 10. Mass distribution comparison between sdB/sdOB stars in Group 3 and the results predicted by Han et al. (2003). From the upper left to bottom right panel, the mass distribution predicted by 12 sets of simulation in Han et al. (2003) are denoted separately by black solid, dashed, and dotted curves (see legend box) in each panel, while the mass distribution for sdB/sdOB stars in Group 3 of this study is present by the magenta dash-dotted curve. Bin numbers for sdB/sdOB stars in Group 3 were normalized to the maximum bin number of Han et al. (2003) in each panel.

side. However, the mass distribution in Schaffenroth et al. (2022) seems to present a little wider peak and have more stars with masses around $0.5 M_{\odot}$ than ours. It could be due to differences in the atmospheric parameters and their uncertainties adopted in the two studies, especially for $\log g$.

4.2. Mass distribution comparison with theoretical models

Han et al. (2003) carried out a detailed binary population synthesis to study the formation of sdB stars. Three main formation channels were investigated in their study, i.e., Roche lobe overflow (RLOF), common-envelope (CE) ejection, and merger of two He-WDs. sdB stars produced from the best-fitting model of these channels could satisfy most observational characteristics, such as $P-M_{\text{comp}}$ plane, $T_{\text{eff}}-\log g$ plane, orbital period distribution, mass function distribution, birth rates, etc. To study the effects of input parameters (e.g., metallicity, initial mass-ratio distribution, the critical mass ratio for stable RLOF q_{crit} , CE ejection efficiency α_{CE} and thermal contribution to the binding energy of the envelope α_{th} , etc) on the formation of sdB stars, they conducted 12 sets of Monte Carlo simulations by varying the parameters in a reasonable range (see Table 1 and 2 in their study). Han et al. (2003) give mass distributions for the 12 sets of simulations and chose set 2 as their best-fitting models after comparing their results with observations (see Fig 11 in their study). These results provide a great convenience to study the mass distribution of sdB stars and thus their formation channels.

In Fig 10, we compared the mass distribution of our sdB/sdOB stars from Group 3 with mass distributions for the 12 sets of simulation in Han et al. (2003). In the upper left panel, the mass distribution for our sdB/sdOB stars from Group 3 (e.g., magenta dash-dotted curve) is generally consistent with the mass distribution predicted by set

1, 2 and 3 simulations in Han et al. (2003), which are denoted by black solid, dashed and dotted curves respectively. Furthermore, the mass distribution peaks predicted by Han et al. (2003), i.e., at $0.46 M_{\odot}$, agree quite well with the one presented in this study. However, the sdB mass distribution in Han et al. (2003) displays a much steeper fall for masses larger than $0.48 M_{\odot}$. It seems to demonstrate that the main channels in Han et al. (2003) predicted fewer sdB stars above $0.48 M_{\odot}$ than the results from this study. Note that, to compare with the observational results of Maxted et al. (2001), which is biased against sdB binaries with bright F/G type companions, the GK selection in Han et al. (2003) removed sdB binary systems with companions having T_{eff} higher than 4000 K or brighter than the sdB primaries. Due to the strict selection criterion, we did not compare the results with corrections for the GK selection effects in Han et al. (2003) with the results obtained in this study directly. Since the minimum core mass for igniting He in a non-degenerate core is about $0.3 M_{\odot}$, while the minimum core mass to ignite He in degenerate stars could be larger (see Table 1 and Table 2 in Han et al. 2002), sdB stars have a low mass cutoff around $0.3 M_{\odot}$ in Han et al. (2003). There are still some stars less massive than $0.3 M_{\odot}$ in our sdB/sdOB sample, which can be low-mass WDs or pre-ELM WDs.

The three other (e.g., bottom left, upper right, and bottom right) panels in Fig 10 present the mass distribution comparison between our sdB/sdOB stars from Group 3 and the simulations of set 4 to 12 in Han et al. (2003), respectively. Though the peaks of mass distributions are roughly consistent between the two studies, models from set 4 to 12 in Han et al. (2003) predicted obviously fewer stars at the low mass side (e.g., $0.3 - 0.42 M_{\odot}$) than this study. Therefore, the mass distribution for sdB/sdOB stars from Group 3 in this study prefers the model predictions of set 1 to 3 in Han et al. (2003), especially for set 2 (e.g., the black dashed curve in the upper left panel, with $Z = .02$, a flat initial mass ratio distribution, $q_{\text{crit}}=1.5$, $\alpha_{\text{CE}}=\alpha_{\text{th}}=0.75$) even by visual inspections.

To study how parameter variations in binary evolution impact the production of sdB stars, Clausen et al. (2012) also conducted a grid of binary population synthesis models with different parameter assumptions, such as minimum core mass for He ignition, envelope binding energy, CE ejection efficiency, amount of mass and angular momentum loss during stable mass transfer, and the criteria for a stable mass transfer on the RGB and in the Hertzsprung gap, etc. (see Table 1 in their study). They found that the variations of these parameters separately or together can significantly change the production of sdB binaries. They present mass distributions of sdB stars for 14 sets of simulations in Fig 14 of their study, most of which predicted similar mass distributions as in Han et al. (2003), especially for their Run 6 which used very similar parameters as the best-fitting model (set 2) in Han et al. (2003). However, most of the models in Clausen et al. (2012) predicted a most probable mass for sdB stars around $0.48 M_{\odot}$, which is higher by about $0.02 M_{\odot}$ than the value obtained in this study and by Han et al. (2003). They also predicted a population of post-RGB stars in their models, which has a lower mean stellar mass (e.g., less than $0.22 M_{\odot}$, see Fig 14 in their study) than sdB stars and failed to ignite He burning in the cores due to an excessive mass transfer on the RGB, but still crossed the sdB region in $T_{\text{eff}} - \log g$ plane. This population also appears in our results as we mentioned above, e.g., stars less massive than $0.3 M_{\odot}$ in Group 3 (see Fig 8). Furthermore, the models by Clausen et al. (2012) predicted an obvious mass gap between the sdB and post-RGB population between $0.22-0.26 M_{\odot}$ (see Fig 14 in their study), but this feature is not present in our sdB/sdOB stars (see Fig 8). It could be averaged out due to a different bin size adopted in our sample, and the overlap of different types of hot subdwarf stars would also mask this feature in our mass distributions. We will continue to discuss the nature of this population in Section 4.4.

4.3. Mass distribution for He-rich hot subdwarf stars and their binary nature

Geier et al. (2022) performed a radial velocity (RV) variability study for 646 single-lined hot subdwarfs having multi-epoch observed spectra in SDSS and LAMOST. The distribution of the maximum RV variations, (i.e., ΔRV_{max} , defined as the difference between the maximum and minimum RV values of a star, see Section 2.3 in their study), was used as diagnostics to study the RV variability thus the binarity of hot subdwarfs. If a false-detection probability calculated in their study, p is smaller than 0.01% ($\log p < -4.0$), the detection of RV variability was considered to be significant, thus a close hot subdwarf binary should be expected. Employing this method, they confirmed 164 hot subdwarf stars in the sample showing significant RV variations. They also found a distinctive difference between He-poor and He-rich hot subdwarfs, that the former present a high fraction of close binaries, while nearly no significant RV variations were detected for the latter. This result made them conclude that there is no evolutionary connection between He-poor and He-rich hot subdwarfs. Moreover, their results also indicated that He-rich hot subdwarfs should be formed from

Table 3. Statistical properties of hot subdwarfs in the three groups also having detected RV variations by Geier et al. (2022).

Group	Subset	Total	Close binary	Close binary
Name	Name	Number	Number	Fraction(%)
Group 1	All sample	216	86	40
	sdB/sdOB	173	72	42
	He-rich sample	16	1	6
	sdO	27	13	48
Group 2	All sample	159	66	42
	sdB/sdOB	130	54	42
	He-rich sample	10	1	10
	sdO	19	11	58
Group 3	All sample	96	42	44
	sdB/sdOB	78	34	44
	He-rich sample	7	1	14
	sdO	11	7	64

NOTE—Close binaries are defined by $\log p < -4.0$ (see text for details).

the binary merger channels when considering the results from Pelisoli et al. (2020) that binary interaction is always required to form hot subdwarf stars.

To investigate the binarity of hot subdwarf stars in our study, we cross-matched the selected stars in the three groups with the hot subdwarfs studied by Geier et al. (2022) respectively. The statistical properties of the common objects are shown in Table 3. From left to right, it gives the group name, subset name, number counts, close binary number counts, and close binary fractions, respectively. There are in total 216 hot subdwarfs in Group 1 also having RV variation values detected by Geier et al. (2022), among which 86 stars present significant RV variations (e.g., $\log p < -4.0$). It means that about 40% of hot subdwarfs are expected to be in close binaries in this group. Specifically, sdB/sdOB stars present a binary fraction of 42% and sdO stars present a binary fraction of 48%. He-rich (e.g., He-sdB, He-sdOB and He-sdO) stars in our sample present a much lower close binary fraction of 6%, and only one star has a significant RV variation among the 16 He-rich stars. With an increasing parallax precision from Group 1 to 3, the fractions of close binaries in each subset for three groups are roughly consistent. Furthermore, though both He-poor and He-rich stars in this study present a little higher close binary fraction than the counterparts in Geier et al. (2022), e.g., $30 \pm 2\%$ for He-poor stars and about 3% for He-rich stars (see Section 3.1 in their study for details), these results are still consistent with each other when considering the randomness of cross-matching between the two sets of samples.

Fig 11 shows the relationship between mass distribution and the maximum RV variations for the 96 common objects between Group 3 in this study and Geier et al. (2022). As clearly shown in the figure, there are a considerable number of objects that present large maximum RV variations and have very small false-detection probabilities (denoted by the color bar on the right of the figure. e.g., $\log p < -4.0$ means significant RV variability) for all sample (upper left panel), sdB/sdOB stars (upper right panel) and sdO stars (bottom right panel), which indicates a moderate close binary fraction among these types of hot subdwarfs (e.g., higher than 40%, see Table 3). While in the bottom left panel, He-rich stars present nearly no significant RV variations, which is very different from sdB/sdOB and sdO stars. Based on this feature, Geier et al. (2022) came to the conclusion that there is no evolutionary connection between He-rich and He-poor hot subdwarf stars, and He-rich stars are formed by the binary merger channels. If this is the case, He-rich hot subdwarfs should present a higher fraction of massive stars than He-poor hot subdwarfs, since hot subdwarf stars formed from merger channel shall have larger masses on average according to the model prediction of Han et al. (2002, 2003), also see the results from Zhang & Jeffery (2012) and Zhang et al. (2017). However, based on our results presented in Table 2, He-rich stars have nearly the same fraction of massive stars (e.g., about 20%)

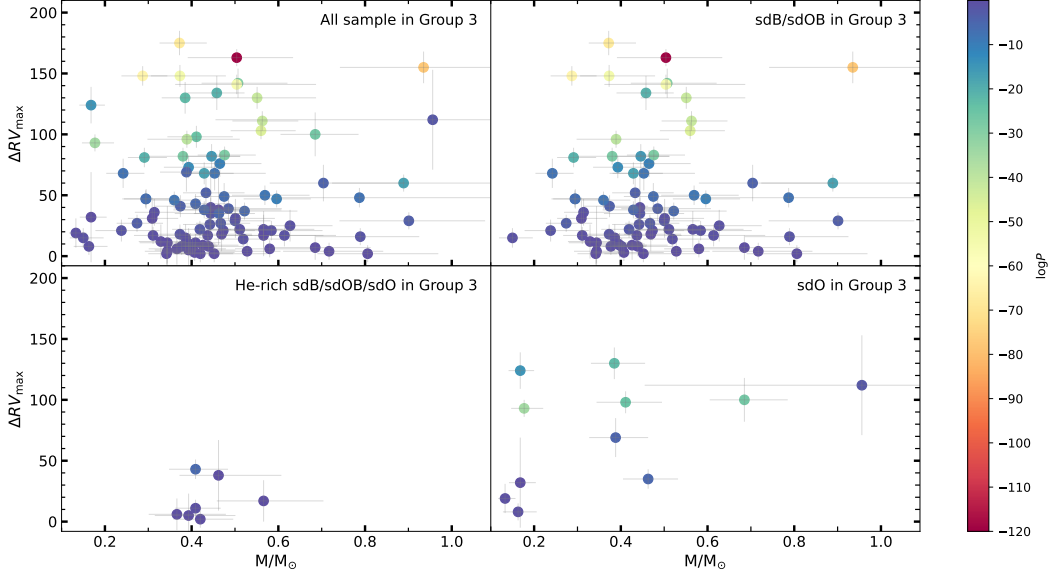


Figure 11. Mass - ΔRV_{\max} plane for hot subdwarf stars in Group 3 also having detected RV variations in Geier et al. (2022). The four panels in the figure show the relationship between mass and binarity for the different populations, i.e., all sample (upper left), sdB/sdO stars (upper right), He-rich stars (bottom left), and sdO stars (bottom right), respectively. The color bar on the right is scaled to the values of false-detection probability ($\log p$). Note that stars with $\log p < -4.0$ are considered to have significant RV variations and thus expected to be in close binaries, see Section 2.3 in Geier et al. (2022) for more details.

as He-poor sdB/sdOB stars, which does not support binary mergers as the only formation channel for He-rich hot subdwarfs.

To understand this issue more clearly, in Fig 12, we compared the mass distribution of He-rich stars from Group 3 in this study with the results predicted by two He-WD merger channels from set 2 simulation in Han et al. (2003). As seen in the figure, the two He-WD merger channel (black dotted curve) predicts a wide mass distribution of hot subdwarfs, e.g., roughly from 0.42 to $0.76 M_{\odot}$, with a fairly wide peak between 0.5 and $0.6 M_{\odot}$. On the other hand, He-rich stars in this study (blue dash-dotted curve) present a wider mass distribution, e.g., from 0.3 to nearly $1.0 M_{\odot}$, with a sharp peak around $0.42 M_{\odot}$ ⁶, which is much lower than the wide peak predicted by binary merger channel. Furthermore, our He-rich sample presents a much lower relative contribution than the model predicts in the broad mass peak area (e.g., 0.5 - $0.6 M_{\odot}$). Zhang et al. (2017) also studied the merger of a He-WD with an MS star, which can produce intermediate helium-rich (iHe-rich, e.g., $-1.0 < \log(n\text{He}/n\text{H}) < 1.0$) hot subdwarfs. However, most of the iHe-rich hot subdwarfs formed through the He-WD+MS merger channel have masses in the range of $0.48 - 0.50 M_{\odot}$, and a few of them have masses up to $0.52 M_{\odot}$, which is also more massive than the mass peak in our He-rich hot subdwarf sample.

As discussed above, these comparisons of results indicated that the two He-WD or the He-WD+MS merger channels cannot be the only formation channels for He-rich hot subdwarfs, some other mechanisms must exist and make contributions to form this kind of stars. Meng & Luo (2021) proposed that the MS companions of massive WDs can survive a Type Ia supernova (SN Ia) explosions and evolve into hot subdwarfs. The hot subdwarfs formed in this channel are also single and He enriched. Moreover, the results based on binary population synthesis can explain some observed features of iHe-rich hot subdwarfs, especially when spin-up/spin-down models were considered. Surprisingly, the spin-up/spin-down models predict the production of hot subdwarfs in the mass range from 0.35 to $1.0 M_{\odot}$, and a distinct mass peak around $0.4 M_{\odot}$ (see Fig 9 in their study), which is consistent with the mass distribution of He-rich stars obtained in this study. However, the same model predicted a low Galactic birth rate for He-rich hot subdwarf stars (e.g., $2.3 - 6 \times 10^{-4} \text{yr}^{-1}$, see Section 4.1 in their study), which demonstrates that some other channels still contribute to the formation of He-rich hot subdwarfs.

⁶ We also studied He-rich stars in Group 1 and 2, and similar mass distributions were obtained as in Group 3.

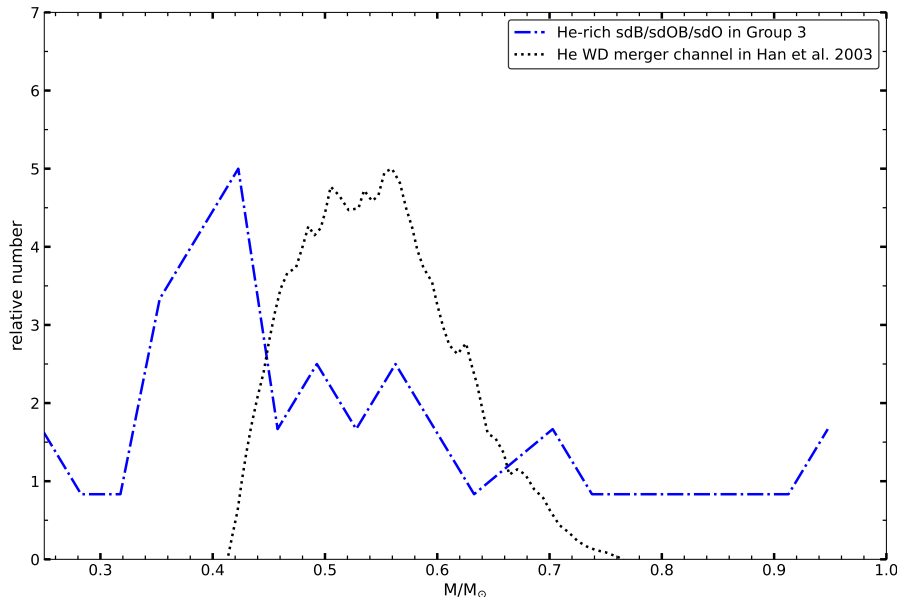


Figure 12. Mass distribution comparison for He-rich hot subdwarfs in Group 3 of this study (blue dash-dotted curve) with the results predicted by two He-WD merger channel in Han et al. (2003) (black dotted curve). Bin numbers in Group 3 were normalized to the maximum bin number of Han et al. (2003).

On the other hand, Werner et al. (2022) discovered two He-sdO stars with unusually strong carbon and oxygen lines (named CO-sdO stars in their study). This new type of hot subdwarf star can neither be explained by a late hot He-core flash (Battich et al. 2018) nor by the merger of two He-WDs, which are considered as the formation channels for canonical He-sdO stars. Miller Bertolami et al. (2022) proposed a new formation channel for the two CO-sdO stars discovered by Werner et al. (2022). In this scenario, the merger of a more massive He-WD and a less massive CO-WD could ignite He core or shell burning and become a CO-sdO star. The material of the CO-WD could be accreted on the top of He-WD and leads to the CO-enriched envelope. This scenario explains the surface parameters and composition of CO-sdO stars. However, Miller Bertolami et al. (2022) did not give the mass distribution for this formation channel, thus we cannot compare our results with it directly. As discussed in Miller Bertolami et al. (2022), the scenario proposed in their study can be a small sub-channel, since the parameter space of the progenitor system needs to be well defined (see Section 2 in their study for detailed discussion) and CO-sdO stars are just a minority compared to the hot subdwarf population. Therefore, this scenario plays a limited role in the formation of He-sdO stars.

Based on the results mentioned above, one can conclude that in addition to the two He-WD merger channels, there should be some other channels that still make contributions to the formation of He-rich hot subdwarf stars, e.g., the SNe Ia explosion channel could make some contributions on the formation of less massive He-rich hot subdwarfs (e.g., less than $0.44 M_{\odot}$, see Fig 12), while the binary merger channel could dominate the formation of massive He-rich hot subdwarfs (e.g., larger than $0.44 M_{\odot}$).

4.4. The nature of low-mass hot subdwarf stars

The minimum core mass for He ignition predicted by models is about $0.3 M_{\odot}$ (Han et al. 2002; Clausen et al. 2012), which could be a little different depending on metallicity and initial mass at zero-age main sequence (ZAMS). Therefore, hot subdwarf stars less massive than $0.3 M_{\odot}$ found in this study are potential post-RGB stars (e.g., low-mass WDs or pre-ELM WDs) that failed to ignite He burning in their cores.

It is believed that ELM WDs cannot be formed by the evolution of single stars since the evolutionary timescale of such low-mass stars would exceed the Hubble time. Istrate et al. (2016) studied the effects of element diffusion and rotational mixing on the evolution of pre-ELM WDs with various metallicities. They found that element diffusion plays a significant role in the evolution of pre-ELM WDs which experience hydrogen shell flashes. Moreover, rotational mixing plays a key role in determining their surface chemical abundances, but it does not influence significantly the number of hydrogen shell flashes and the hydrogen envelope mass at the beginning of the cooling track. They calculated

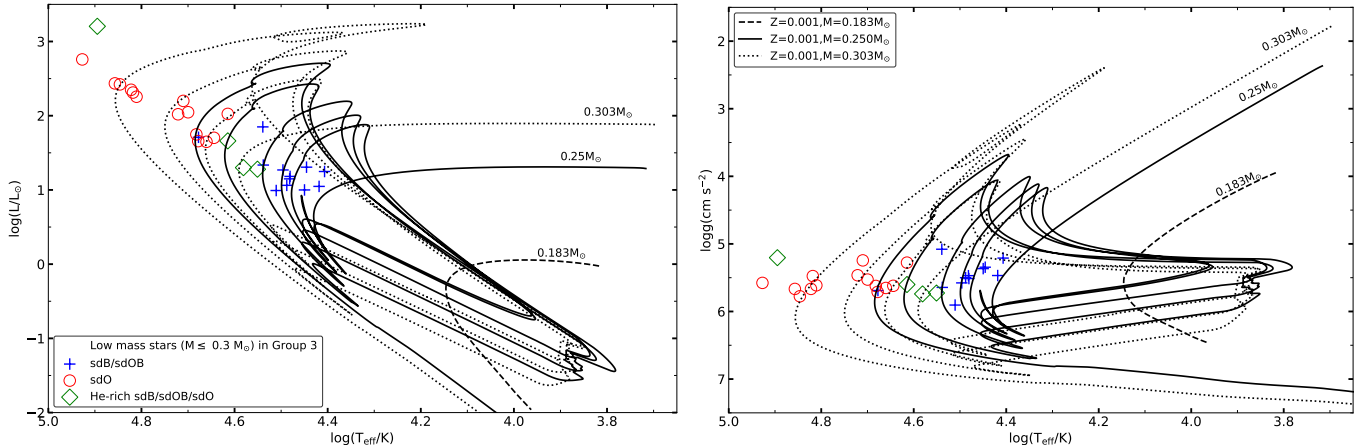


Figure 13. Left panel: T_{eff} – luminosity plane for low-mass stars (i.e., less than $0.3 M_{\odot}$) in Group 3. Right panel: T_{eff} – $\log g$ plane for low-mass stars in Group 3. Black dashed, solid and dotted curves in the panel are evolutionary tracks of pre-ELM WDs with $Z = 0.001$ from [Istrate et al. \(2016\)](#) for $M = 0.183, 0.25$ and $0.303 M_{\odot}$ respectively.

a large number of evolutionary tracks of pre-ELM WDs within a mass range of $0.16 - 0.45 M_{\odot}$, which provides great convenience to analyze the nature of low-mass hot subdwarf stars in our sample.

Fig 13 shows the T_{eff} – luminosity (left panel) and T_{eff} – $\log g$ planes (right panel) for the low-mass hot subdwarfs (e.g., $M \leq 0.3 M_{\odot}$) in Group 3, together with three evolutionary tracks of pre-ELM WDs at $Z = 0.001$ from [Istrate et al. \(2016\)](#). As can be seen in the figure, the positions of all low-mass sdB/sdOB stars (blue pluses), most of low-mass sdO stars (red circles), and He-rich stars (green squares) can be covered by the evolutionary tracks of pre-ELM WDs with higher stellar masses, e.g., $0.25 M_{\odot}$ (black solid curve) and $0.303 M_{\odot}$ (black dotted curve) both in T_{eff} – luminosity plane and T_{eff} – $\log g$ plane. These models experience several hydrogen shell flashes before entering the final cooling curve. On the other hand, our low-mass stars cannot be covered by the less massive evolutionary track of $M = 0.183 M_{\odot}$, which did not experience any hydrogen shell flashes due to the thick shell (see Section 2.1 in [Istrate et al. 2016](#) for detailed discussion). Furthermore, we checked the mass distribution of low-mass hot subdwarfs in Group 3 and found that most of the low-mass sdB/sdOB stars and He-rich stars have masses in the range of $0.25 - 0.30 M_{\odot}$, while most of the low-mass sdO stars have masses around $0.18 M_{\odot}$ as described in Table 1.

The results described above indicate that low-mass sdB/sdOB stars and He-rich stars should be post-RGB stars, which would lose too much envelope mass at the RGB stage to ignite He burning in their cores, and now are on the way towards the ELM WD cooling curves. [Heber et al. \(2003\)](#) discovered a pre-ELM WD in a close binary system, named HD 188112, with a mass of $0.24 M_{\odot}$. The primary in that system presents $T_{\text{eff}} = 21\,500 \pm 500$ K and $\log g = 5.66 \pm 0.05$, which is located at a similar region as our low-mass sdB/sdOB stars in the T_{eff} – $\log g$ plane. However, pre-ELM models seem unable to explain our low-mass sdO stars. Because the evolutionary tracks with the same mass (e.g., about $0.18 M_{\odot}$, black dashed curve in Fig 13) predict much lower effective temperatures than our low-mass sdO stars (red circles in Fig 13, also see [Brown et al. 2022](#)). Thus, this result demonstrates that some other unknown mechanisms could play roles in the formation and evolution of these low-mass sdO stars, which need to be studied in the future.

5. SUMMARY

In this study, we obtained the radii, luminosities, and masses for 664 hot subdwarf stars identified in LAMOST by comparing synthetic fluxes from theoretical spectral energy distributions with observed fluxes from virtual observatory services. The relationship between stellar masses and atmospheric parameters was explored, interpreted, and shown. To study the mass distribution in our sample, three groups of hot subdwarf stars were selected by using their parallax precision. A wide mass distribution of hot subdwarf stars from 0.1 to $1.0 M_{\odot}$ is presented, and a sharp peak was found at $0.46 M_{\odot}$. The mass distribution of sdB/sdOB stars is consistent with the ones from model predictions. However, canonical binary models seem to predict fewer sdB stars with masses larger than $0.48 M_{\odot}$ when compared with the mass distribution obtained in this study. He-poor sdO and He-rich hot subdwarfs present a much flatter mass distribution and have a peak mass at 0.18 and $0.42 M_{\odot}$, respectively. sdB/sdOB and sdO stars have similar close

binary fractions in our sample (e.g., about 40%), and the similar mass - ΔRV_{\max} distribution between them supports that sdO stars are the subsequent evolution stage of sdB/sdOB stars. While, He-rich stars present a much lower close binary fraction than He-poor stars, which supports the binary merger formation channel for these stars. However, He-rich hot subdwarf stars in our sample present a peak mass at $0.42 M_{\odot}$, which is less than the wide mass peak of $0.5 - 0.6 M_{\odot}$ from the predictions of the binary merger channel, but consistent with the SN Ia explosion channel. Our results indicate that binary merger could not be the only main formation channel for He-rich hot subdwarf stars, other channels such as the SN Ia explosion or some other unknown channels must also play an important role in producing this special population, especially for He-rich hot subdwarf stars less massive than $0.44 M_{\odot}$.

We thank the anonymous referee for his/her valuable suggestions and comments which helped improve the manuscript greatly. This work acknowledges support from the National Natural Science Foundation of China (Nos. 12073020 and 12273055, 12273055, 11973048), Scientific Research Fund of Hunan Provincial Education Department grant No. 20K124, Cultivation Project for LAMOST Scientific Payoff and Research Achievement of CAMS-CAS, the science research grants from the China Manned Space Project with No. CMS-CSST-2021-B05. P.N. acknowledges support from the Grant Agency of the Czech Republic (GAČR 22-34467S) and from the Polish National Science Centre under projects UMO-2017/26/E/ST9/00703 and UMO-2017/25/B/ST9/02218. This research has made use of the Spanish Virtual Observatory (<https://svo.cab.inta-csic.es>) project funded by MCIN/AEI/10.13039/501100011033/through grant PID2020-112949GB-I00. Guoshoujing Telescope (the Large Sky Area Multi-Object Fiber Spectroscopic Telescope LAMOST) is a National Major Scientific Project built by the Chinese Academy of Sciences. Funding for the project has been provided by the National Development and Reform Commission. LAMOST is operated and managed by the National Astronomical Observatories, Chinese Academy of Sciences. This research has used the services of www.Astroserver.org under references: X074VU, KS5NVO, XD8O2C, D879YE and D880YE.

Software: TOPCAT (Taylor 2005)

REFERENCES

- Astraatmadja, T. L., & Bailer-Jones, C. A. L. 2016, ApJ, 832, 137, doi: [10.3847/0004-637X/832/2/137](https://doi.org/10.3847/0004-637X/832/2/137)
- Bailer-Jones, C. A. L. 2015, PASP, 127, 994, doi: [10.1086/683116](https://doi.org/10.1086/683116)
- Bailer-Jones, C. A. L., Rybizki, J., Fouesneau, M., Demleitner, M., & Andrae, R. 2021, AJ, 161, 147, doi: [10.3847/1538-3881/abd806](https://doi.org/10.3847/1538-3881/abd806)
- Baran, A. S., Østensen, R. H., Heber, U., et al. 2021, MNRAS, 503, 2157, doi: [10.1093/mnras/stab620](https://doi.org/10.1093/mnras/stab620)
- Battich, T., Miller Bertolami, M. M., Córscico, A. H., & Althaus, L. G. 2018, A&A, 614, A136, doi: [10.1051/0004-6361/201731463](https://doi.org/10.1051/0004-6361/201731463)
- Bayo, A., Rodrigo, C., Barrado Y Navascués, D., et al. 2008, A&A, 492, 277, doi: [10.1051/0004-6361:200810395](https://doi.org/10.1051/0004-6361:200810395)
- Brown, T. M., Sweigart, A. V., Lanz, T., et al. 2010, ApJ, 718, 1332, doi: [10.1088/0004-637X/718/2/1332](https://doi.org/10.1088/0004-637X/718/2/1332)
- Brown, T. M., Cassisi, S., D'Antona, F., et al. 2016, ApJ, 822, 44, doi: [10.3847/0004-637X/822/1/44](https://doi.org/10.3847/0004-637X/822/1/44)
- Brown, W. R., Kilic, M., Kosakowski, A., & Gianninas, A. 2022, ApJ, 933, 94, doi: [10.3847/1538-4357/ac72ac](https://doi.org/10.3847/1538-4357/ac72ac)
- Castellani, M., & Castellani, V. 1993, ApJ, 407, 649, doi: [10.1086/172547](https://doi.org/10.1086/172547)
- Chen, X., Han, Z., Deca, J., & Podsiadlowski, P. 2013, MNRAS, 434, 186, doi: [10.1093/mnras/stt992](https://doi.org/10.1093/mnras/stt992)
- Clausen, D., Wade, R. A., Kopparapu, R. K., & O'Shaughnessy, R. 2012, ApJ, 746, 186, doi: [10.1088/0004-637X/746/2/186](https://doi.org/10.1088/0004-637X/746/2/186)
- Copperwheat, C. M., Morales-Rueda, L., Marsh, T. R., Maxted, P. F. L., & Heber, U. 2011, MNRAS, 415, 1381, doi: [10.1111/j.1365-2966.2011.18786.x](https://doi.org/10.1111/j.1365-2966.2011.18786.x)
- Culpan, R., Geier, S., Reindl, N., et al. 2022, A&A, 662, A40, doi: [10.1051/0004-6361/202243337](https://doi.org/10.1051/0004-6361/202243337)
- Dorman, B., Rood, R. T., & O'Connell, R. W. 1993, ApJ, 419, 596, doi: [10.1086/173511](https://doi.org/10.1086/173511)
- Drilling, J. S., Jeffery, C. S., Heber, U., Moehler, S., & Napiwotzki, R. 2013, A&A, 551, A31, doi: [10.1051/0004-6361/201219433](https://doi.org/10.1051/0004-6361/201219433)
- Edelmann, H., Heber, U., Hagen, H. J., et al. 2003, A&A, 400, 939, doi: [10.1051/0004-6361:20030135](https://doi.org/10.1051/0004-6361:20030135)
- Fontaine, G., Brassard, P., Charpinet, S., et al. 2012, A&A, 539, A12, doi: [10.1051/0004-6361/201118220](https://doi.org/10.1051/0004-6361/201118220)
- Fontaine, G., Green, E., Brassard, P., Latour, M., & Chayer, P. 2014, in Astronomical Society of the Pacific Conference Series, Vol. 481, 6th Meeting on Hot Subdwarf Stars and Related Objects, ed. V. van Grootel, E. Green, G. Fontaine, & S. Charpinet, 83
- Gaia Collaboration, Prusti, T., de Bruijne, J. H. J., et al. 2016, A&A, 595, A1, doi: [10.1051/0004-6361/201629272](https://doi.org/10.1051/0004-6361/201629272)

- Gaia Collaboration, Brown, A. G. A., Vallenari, A., et al. 2018, *A&A*, 616, A1, doi: [10.1051/0004-6361/201833051](https://doi.org/10.1051/0004-6361/201833051)
- . 2021, *A&A*, 649, A1, doi: [10.1051/0004-6361/202039657](https://doi.org/10.1051/0004-6361/202039657)
- Geier, S. 2020, *A&A*, 635, A193, doi: [10.1051/0004-6361/202037526](https://doi.org/10.1051/0004-6361/202037526)
- Geier, S., Dorsch, M., Pelisoli, I., et al. 2022, *A&A*, 661, A113, doi: [10.1051/0004-6361/202143022](https://doi.org/10.1051/0004-6361/202143022)
- Geier, S., Østensen, R. H., Németh, P., et al. 2017, *A&A*, 600, A50, doi: [10.1051/0004-6361/201630135](https://doi.org/10.1051/0004-6361/201630135)
- Geier, S., Kupfer, T., Heber, U., et al. 2015, *A&A*, 577, A26, doi: [10.1051/0004-6361/201525666](https://doi.org/10.1051/0004-6361/201525666)
- Han, Z., Podsiadlowski, P., Maxted, P. F. L., & Marsh, T. R. 2003, *MNRAS*, 341, 669, doi: [10.1046/j.1365-8711.2003.06451.x](https://doi.org/10.1046/j.1365-8711.2003.06451.x)
- Han, Z., Podsiadlowski, P., Maxted, P. F. L., Marsh, T. R., & Ivanova, N. 2002, *MNRAS*, 336, 449, doi: [10.1046/j.1365-8711.2002.05752.x](https://doi.org/10.1046/j.1365-8711.2002.05752.x)
- Heber, U. 2009, *ARA&A*, 47, 211, doi: [10.1146/annurev-astro-082708-101836](https://doi.org/10.1146/annurev-astro-082708-101836)
- . 2016, *PASP*, 128, 082001, doi: [10.1088/1538-3873/128/966/082001](https://doi.org/10.1088/1538-3873/128/966/082001)
- Heber, U., Edelmann, H., Lisker, T., & Napiwotzki, R. 2003, *A&A*, 411, L477, doi: [10.1051/0004-6361:20031553](https://doi.org/10.1051/0004-6361:20031553)
- Heber, U., Irrgang, A., & Schaffenroth, J. 2018, *Open Astronomy*, 27, 35, doi: [10.1515/astro-2018-0008](https://doi.org/10.1515/astro-2018-0008)
- Heber, U., Reid, I. N., & Werner, K. 2000, *A&A*, 363, 198, doi: [10.48550/arXiv.astro-ph/0009159](https://doi.org/10.48550/arXiv.astro-ph/0009159)
- Howell, S. B., Sobek, C., Haas, M., et al. 2014, *PASP*, 126, 398, doi: [10.1086/676406](https://doi.org/10.1086/676406)
- Hubeny, I., & Lanz, T. 2017, arXiv e-prints, arXiv:1706.01859. <https://arxiv.org/abs/1706.01859>
- Irrgang, A., Geier, S., Heber, U., et al. 2021, *A&A*, 650, A102, doi: [10.1051/0004-6361/202038757](https://doi.org/10.1051/0004-6361/202038757)
- Istrate, A. G., Marchant, P., Tauris, T. M., et al. 2016, *A&A*, 595, A35, doi: [10.1051/0004-6361/201628874](https://doi.org/10.1051/0004-6361/201628874)
- Jeffery, C. S., Miszalski, B., & Snowdon, E. 2021, *MNRAS*, 501, 623, doi: [10.1093/mnras/staa3648](https://doi.org/10.1093/mnras/staa3648)
- Kepler, S. O., Pelisoli, I., Koester, D., et al. 2015, *MNRAS*, 446, 4078, doi: [10.1093/mnras/stu2388](https://doi.org/10.1093/mnras/stu2388)
- . 2016, *MNRAS*, 455, 3413, doi: [10.1093/mnras/stv2526](https://doi.org/10.1093/mnras/stv2526)
- . 2019, *MNRAS*, 486, 2169, doi: [10.1093/mnras/stz960](https://doi.org/10.1093/mnras/stz960)
- Krziesinski, J., Şener, H. T., Zola, S., & Siwak, M. 2022, *MNRAS*, 516, 1509, doi: [10.1093/mnras/stac2088](https://doi.org/10.1093/mnras/stac2088)
- Lanz, T., & Hubeny, I. 2007, *ApJS*, 169, 83, doi: [10.1086/511270](https://doi.org/10.1086/511270)
- Lei, Z., Bu, Y., Zhao, J., Németh, P., & Zhao, G. 2019a, *PASJ*, 71, 41, doi: [10.1093/pasj/psz006](https://doi.org/10.1093/pasj/psz006)
- Lei, Z., Zhao, J., Németh, P., & Zhao, G. 2018, *ApJ*, 868, 70, doi: [10.3847/1538-4357/aae82b](https://doi.org/10.3847/1538-4357/aae82b)
- . 2019b, *ApJ*, 881, 135, doi: [10.3847/1538-4357/ab2edc](https://doi.org/10.3847/1538-4357/ab2edc)
- . 2020, *ApJ*, 889, 117, doi: [10.3847/1538-4357/ab660a](https://doi.org/10.3847/1538-4357/ab660a)
- Lei, Z., He, R., Németh, P., et al. 2023, *ApJ*, 942, 109, doi: [10.3847/1538-4357/aca542](https://doi.org/10.3847/1538-4357/aca542)
- Lindegren, L., Klioner, S. A., Hernández, J., et al. 2021a, *A&A*, 649, A2, doi: [10.1051/0004-6361/202039709](https://doi.org/10.1051/0004-6361/202039709)
- Lindegren, L., Bastian, U., Biermann, M., et al. 2021b, *A&A*, 649, A4, doi: [10.1051/0004-6361/202039653](https://doi.org/10.1051/0004-6361/202039653)
- Lisker, T., Heber, U., Napiwotzki, R., et al. 2005, *A&A*, 430, 223, doi: [10.1051/0004-6361:20040232](https://doi.org/10.1051/0004-6361:20040232)
- Luo, Y., Németh, P., Deng, L., & Han, Z. 2019, *ApJ*, 881, 7, doi: [10.3847/1538-4357/ab298d](https://doi.org/10.3847/1538-4357/ab298d)
- Luo, Y., Németh, P., Wang, K., Wang, X., & Han, Z. 2021, *ApJS*, 256, 28, doi: [10.3847/1538-4365/ac11f6](https://doi.org/10.3847/1538-4365/ac11f6)
- Luo, Y.-P., Németh, P., Liu, C., Deng, L.-C., & Han, Z.-W. 2016, *ApJ*, 818, 202, doi: [10.3847/0004-637X/818/2/202](https://doi.org/10.3847/0004-637X/818/2/202)
- Martin, D. C., Fanson, J., Schiminovich, D., et al. 2005, *ApJL*, 619, L1, doi: [10.1086/426387](https://doi.org/10.1086/426387)
- Maxted, P. F. L., Heber, U., Marsh, T. R., & North, R. C. 2001, *MNRAS*, 326, 1391, doi: [10.1111/j.1365-2966.2001.04714.x](https://doi.org/10.1111/j.1365-2966.2001.04714.x)
- Meng, X.-C., & Luo, Y.-P. 2021, *MNRAS*, 507, 4603, doi: [10.1093/mnras/stab2369](https://doi.org/10.1093/mnras/stab2369)
- Mengel, J. G., Norris, J., & Gross, P. G. 1976, *ApJ*, 204, 488, doi: [10.1086/154193](https://doi.org/10.1086/154193)
- Miller Bertolami, M. M., Althaus, L. G., Unglaub, K., & Weiss, A. 2008, *A&A*, 491, 253, doi: [10.1051/0004-6361:200810373](https://doi.org/10.1051/0004-6361:200810373)
- Miller Bertolami, M. M., Battich, T., Córscico, A. H., Althaus, L. G., & Wachlin, F. C. 2022, *MNRAS*, 511, L60, doi: [10.1093/mnras/lsab134](https://doi.org/10.1093/mnras/lsab134)
- Moehler, S., Richtler, T., de Boer, K. S., Dettmar, R. J., & Heber, U. 1990, *A&AS*, 86, 53
- Napiwotzki, R., Karl, C. A., Lisker, T., et al. 2004, *Ap&SS*, 291, 321, doi: [10.1023/B:ASTR.0000044362.07416.6c](https://doi.org/10.1023/B:ASTR.0000044362.07416.6c)
- Németh, P., Kawka, A., & Vennes, S. 2012, *MNRAS*, 427, 2180, doi: [10.1111/j.1365-2966.2012.22009.x](https://doi.org/10.1111/j.1365-2966.2012.22009.x)
- Pelisoli, I., Vos, J., Geier, S., Schaffenroth, V., & Baran, A. S. 2020, *A&A*, 642, A180, doi: [10.1051/0004-6361/202038473](https://doi.org/10.1051/0004-6361/202038473)
- Raddi, R., Torres, S., Rebassa-Mansergas, A., et al. 2022, *A&A*, 658, A22, doi: [10.1051/0004-6361/202141837](https://doi.org/10.1051/0004-6361/202141837)
- Ricker, G. R., Winn, J. N., Vanderspek, R., et al. 2015, *Journal of Astronomical Telescopes, Instruments, and Systems*, 1, 014003, doi: [10.1117/1.JATIS.1.1.014003](https://doi.org/10.1117/1.JATIS.1.1.014003)
- Rodrigo, C., & Solano, E. 2020, in XIV.0 Scientific Meeting (virtual) of the Spanish Astronomical Society, 182
- Rodrigo, C., Solano, E., & Bayo, A. 2012, SVO Filter Profile Service Version 1.0, IVOA Working Draft 15 October 2012, doi: [10.5479/ADS/bib/2012ivoa.rept.1015R](https://doi.org/10.5479/ADS/bib/2012ivoa.rept.1015R)

- Schaffenroth, V., Pelisoli, I., Barlow, B. N., Geier, S., & Kupfer, T. 2022, *A&A*, 666, A182, doi: [10.1051/0004-6361/202244214](https://doi.org/10.1051/0004-6361/202244214)
- Schlafly, E. F., & Finkbeiner, D. P. 2011, *ApJ*, 737, 103, doi: [10.1088/0004-637X/737/2/103](https://doi.org/10.1088/0004-637X/737/2/103)
- Schlegel, D. J., Finkbeiner, D. P., & Davis, M. 1998, *ApJ*, 500, 525, doi: [10.1086/305772](https://doi.org/10.1086/305772)
- Skrutskie, M. F., Cutri, R. M., Stiening, R., et al. 2006, *AJ*, 131, 1163, doi: [10.1086/498708](https://doi.org/10.1086/498708)
- Stroeer, A., Heber, U., Lisker, T., et al. 2007, *A&A*, 462, 269, doi: [10.1051/0004-6361:20065564](https://doi.org/10.1051/0004-6361:20065564)
- Taylor, M. B. 2005, in *Astronomical Society of the Pacific Conference Series*, Vol. 347, *Astronomical Data Analysis Software and Systems XIV*, ed. P. Shopbell, M. Britton, & R. Ebert, 29
- Vennes, S., Kawka, A., & Németh, P. 2011, *MNRAS*, 410, 2095, doi: [10.1111/j.1365-2966.2010.17584.x](https://doi.org/10.1111/j.1365-2966.2010.17584.x)
- Webbink, R. F. 1984, *ApJ*, 277, 355, doi: [10.1086/161701](https://doi.org/10.1086/161701)
- Werner, K., Reindl, N., Geier, S., & Pritzkeleit, M. 2022, *MNRAS*, 511, L66, doi: [10.1093/mnrasl/slac005](https://doi.org/10.1093/mnrasl/slac005)
- Wright, E. L., Eisenhardt, P. R. M., Mainzer, A. K., et al. 2010, *AJ*, 140, 1868, doi: [10.1088/0004-6256/140/6/1868](https://doi.org/10.1088/0004-6256/140/6/1868)
- Zhang, X., Hall, P. D., Jeffery, C. S., & Bi, S. 2017, *ApJ*, 835, 242, doi: [10.3847/1538-4357/835/2/242](https://doi.org/10.3847/1538-4357/835/2/242)
- Zhang, X., & Jeffery, C. S. 2012, *MNRAS*, 419, 452, doi: [10.1111/j.1365-2966.2011.19711.x](https://doi.org/10.1111/j.1365-2966.2011.19711.x)